Master's Thesis

Elastic and Elastoplastic Response of Cubic Lattice Structures

carried out for the purpose of obtaining the degree of Diplom-Ingenieur (Dipl.-Ing.)

submitted at TU Wien

Faculty of Mechanical and Industrial Engineering

by

Luka Mitrovic, BSc

Mat.No.: 01528173

Under the supervision of

Associate Prof. Dipl.-Ing Dr.techn. Heinz Pettermann

Institute of the Lightweight Design and Structural Biomechanics, E317

Vienna, February 2024

Affidavit

I declare in lieu of oath, that I wrote this thesis and carried out the associated research myself, using only the literature cited in this volume. If text passages from sources are used literally, they are marked as such. I confirm that this work is original and has not been submitted for examination elsewhere, nor is it currently under consideration for a thesis elsewhere. I acknowledge that the submitted work will be checked electronically-technically using suitable and state-of-the-art means (plagiarism detection software). On the one hand, this ensures that the submitted work was prepared according to the high-quality standards within the applicable rules to ensure good scientific practice "Code of Conduct" at the TU Wien. On the other hand, a comparison with other student theses avoids violations of my personal copyright.

Vienna, February 2024

Abstract

This work studies the elastic and elastoplastic behavior of a Body-Centered Cubic (BCC) lattice unit cell (UC) with the help of finite element analysis under the assumption of geometric linearity. The periodic microfield approach is implemented, with appropriate periodic boundary conditions applied to the UC. The method of macroscopic degrees of freedom is used to prescribe different load cases to the UC. With this modeling approach, the effective (homogenized) material properties of lattice structure with a BCC UC are obtained. The UC is modeled once with linear shear flexible beam elements in space and once with quadratic tetrahedral continuum elements, and the influence of the modeling approach on results is assessed.

Since the BCC lattice UC shows cubic material symmetry, only three independent material properties are required to determine its effective elasticity tensor. In this work, the effective bulk modulus $\tilde{K}$ obtained from the hydrostatic tensile load case, the effective shear modulus $\tilde{M}$ obtained from the simple shear XY load case, and the effective shear modulus $\tilde{G}$ obtained from the 45° shear XY load case are chosen as the parameters that are determined. For the solid element modeling variant, the effective Young's moduli in the principal material direction [100], the face diagonal [110], and the space diagonal [111] are obtained.

The two-dimensional (2D) initial yield surface representations of the solid element UC are determined under five different sets of load cases. The elastoplastic behavior of the BCC lattice UC under various single and combined load cases is assessed. In addition to the same three load cases required for the determination of the effective elasticity tensor, the uniaxial tension in the [100] direction is also included in the single load cases group. For the combined modeling approach, the combinations of simple shear XY and XZ, simple shear XY and hydrostatic tension, simple shear XY and 45° shear XY, as well as 45° shear XY and hydrostatic tension load cases are modeled. Here, a distinction is made if both of them are applied in the same step or in succession. The differences in the results between varying load cases and modeling approaches are discussed in detail.

Kurzfassung

Diese Arbeit untersucht das elastische und elastoplastische Verhalten einer Gitterstruktur mit kubisch-raumzentrierten (BCC) Einheitszellen (UC) mithilfe der Finite-Elemente-Analyse unter der Annahme geometrischer Linearität. Der periodische Mikrofeldansatz wird implementiert, wobei geeignete periodische Randbedingungen auf die UC angewendet werden. Die Methode der makroskopischen Freiheitsgrade wird verwendet, um verschiedene Lastfälle auf die UC zu übertragen. Mit diesem Modellierungsansatz werden die effektiven (homogenisierten) Materialeigenschaften der Gitterstruktur mit einer BCC-UC ermittelt. Die UC wird einmal mit linearen, schubflexiblen Balkenelementen im Raum und einmal mit quadratischen tetraedrischen Kontinuumselementen modelliert, und der Einfluss des Modellierungsansatzes auf die Ergebnisse wird auswertet.

Da die BCC-UC kubische Materialsymmetrie aufweist, werden nur drei unabhängige Materialeigenschaften benötigt, um ihren effektiven Elastizitätstensor zu bestimmen. In dieser Arbeit werden der effektive Kompressionsmodul $\tilde{K}$, der sich aus dem hydrostatischen Zuglastfall ergibt, der effektive Schermodul $\tilde{M}$, der sich aus dem einfachen Schub-Lastfall (XY) ergibt, und der effektive Schubmodul $\tilde{G}$, der sich aus dem 45° Schub-Lastfall (XY) ergibt, als die zu bestimmenden Parameter gewählt. Für die Modellierungsvariante mit Kontinuumselementen werden die effektiven Elastizitätsmodule in der Hauptmaterialrichtung [100], der Flächendiagonalen [110] und der Raumdiagonalen [111] ermittelt.

Die zweidimensionalen (2D) Darstellungen der Anfangsfließflächen der Kontinuumselement-UC werden unter fünf verschiedenen Lastfallgruppen bestimmt. Das elastoplastische Verhalten der BCC-UC unter verschiedenen einzelnen und kombinierten Lastfällen wird auswertet. Zusätzlich zu den drei Lastfällen, die für die Bestimmung des effektiven Elastizitätstensors erforderlich sind, wird in der Gruppe der Einzellastfälle auch der einachsige Zug in [100]-Richtung berücksichtigt. Für den kombinierten Modellierungsansatz werden die Kombinationen aus einfachem Schub XY und XZ, einfacher Schub XY und hydrostatischem Zug, einfacher Schub XY und 45°-Schub XY sowie 45°-Schub XY und hydrostatischem Zug modelliert. Hier wird unterschieden, ob beide gleichzeitig oder nacheinander angewendet werden. Die Unterschiede in den Ergebnissen zwischen verschiedenen Lastfällen und Modellierungsansätzen werden ausführlich diskutiert.

Contents

1. Introduction

1.1 Motivation and scope of work

Implementing lightweight design principles is crucial in various fields, from aerospace and automotive engineering to energy technology, medicine, and many more. With the continuous development of technology and industry, the requirements on the design increase, and further innovation is necessary [7, 19]. In recent years, the field of additive manufacturing has been consistently improved, and it has shown its potential and many benefits, one of the most important being the ability to produce various complexly shaped components and structures [5, 21, 13, 20]. This allowed the manufacturing of complex open-celled lattice structures with high specific strength and stiffness, as well as outstanding energy absorption capacity [11, 5]. For such periodic structures, depending on the chosen base cell configuration, various macroscopic material properties are obtainable, allowing them to be customized for unique purposes and requirements of many engineering fields [11, 10, 4, 5].

To better understand their behavior, and be able to tailor and optimize their properties, one has to determine the influence of the base cell configuration on their overall mechanical response. A variety of analytical and numerical approaches can be implemented to determine this relation [11, 10]. One of the essential principles of continuum micromechanics, homogenization, allows the estimation of global properties from the behavior at a smaller length scale. The numerical homogenization approaches, especially the ones dealing with unit cells (UCs), like the Periodic Microfield Approaches (PMAs), are suitable for assessing the influence of varying base cell parameters on the homogenized material properties of the periodic cell structure (i.e. infinite periodic arrangement). The PMAs are based on the assumption that the heterogeneous material can be regarded as periodic (i.e. described through the repeating UC). These approaches are implemented via the Finite Element Method (FEM), and since only a single UC is modeled, instead of the complete lattice structure, the computational effort is reduced.

This work studies the elastic and elastoplastic behavior of a Body-Centered-Cubic (BCC) lattice unit cell (UC) with the help of finite element analysis under the assumption of geometric linearity in *Abaqus/Standard 2023 (Dassault Systèmes Simulia Corp., Johnston, Rhode Island, United States)*. The periodic microfield approach is implemented, with appropriate periodic boundary conditions applied to the UC. The method of macroscopic

degrees of freedom is used to prescribe different load cases to the UC. With this modeling approach, the effective (homogenized) material properties of lattice structure with a BCC UC are obtained.

The UC is modeled once with linear shear flexible beam elements in space and once with quadratic tetrahedral continuum elements, and the influence of the modeling approach on results is assessed. The results from beam models are expected to be less accurate than the ones from the solid element models, especially for the load cases where the struts experience bending or shear deformation, but the required computational and pre-processing effort is considerably lower, which is suitable for modeling complex lattice structures. The main reason for these inaccuracies is the inability of beam elements to correctly represent the sites where struts connect (neglecting the material aggregation and overlapping volumes at the junctions of multiple struts in the model), which leads to lower stiffness.

Since the BCC lattice UC shows cubic material symmetry, only three independent material properties are required to determine its effective elasticity tensor. In this work, the effective bulk modulus $\tilde{K}$ obtained from the hydrostatic tensile load case, the effective shear modulus $\tilde{M}$ obtained from the simple shear XY load case, and the effective shear modulus $\tilde{G}$ obtained from the 45° shear XY load case are chosen as the parameters that are determined. For the solid element modeling variant, the effective Young's moduli in the principal material direction [100], the face diagonal [110], and the space diagonal [111] are obtained.

The two-dimensional (2D) initial yield surface representations of the solid element UC are determined under five different sets of load cases. Additionally, the initial yield stress values for all six load cases implemented in the study of the elastic behavior of the BCC lattice UC are obtained.

The elastoplastic behavior of the BCC lattice UC under various single and combined load cases is assessed. In addition to the same three load cases required for the determination of the effective elasticity tensor, the uniaxial tension in the [100] direction is also included in the single load cases group. For the combined modeling approach, the combinations of simple shear XY and XZ, simple shear XY and hydrostatic tension, simple shear XY and 45° shear XY, as well as 45° shear XY and hydrostatic tension load cases are modeled. Here, a distinction is made if both of them are applied in the same step or in succession. The differences in the results between varying load cases and modeling approaches are discussed in detail.

1.2 Literature review

A general introduction to cellular materials, their properties, manufacturing, and applications is found in [9, 2].

The basic principles of additive manufacturing are documented in [21, 8]. A more detailed insight into the processes, like selective laser melting [11, 20, 13, 4] and digital light processing [11, 20], that have been specifically used to produce open-celled lattice structures used for experimental testing in the literature can be found in the corresponding papers.

The theoretical knowledge about elastic and elastoplastic material behavior is based on the Advanced Material Models for Structural Analysis lecture and corresponding lecture material [15]. Additionally, some specific information regarding cubic material symmetry is found in [12].

The theoretical knowledge behind the FEM is based on the lecture Introduction to the Finite Element Method and corresponding lecture material [6], and some segments about the specific functioning of *Abaqus* are referenced from the supporting documentation [1].

The modeling in this work is based on the principles of continuum micromechanics. The information regarding this field is mainly from the university lecture Composites Engineering and learning materials that supplement it [3]. The main ideas like homogenization and localization, and the approximations used for them, are described in detail there. Since the main focus of this work is on homogenization, and specifically on the PMAs, the main interests lie in the models of unit cells. Additionally, a comprehensive overview of the UC approach, including a detailed implementation of PBCs, has been shown in [16].

The implementation of this modeling approach for open-celled lattice structures has already been studied in the literature. In [11], the mechanical behavior of polymer lattice structures with a Simple Cubic (SC), Gibson Ashby (GA), Body-Centered-Cubic (BCC), and Reinforced BCC (RBCC) base cell structures have been assessed with the help of FEM models and experiments. They have been modeled as continuum element, beam element, and modified beam element models, where the stiffness in the vicinity of vertices has been artificially increased to account for the material aggregation in these regions. The modeled structures have been treated as an infinite media (UC model approach), as well as a finite media (finite-size model). The finite-size ones (restricted to beam elements) have been modeled to be comparable to the experimental specimens in the uniaxial compression test. The UCs have been employed to predict the complete elasticity

tensor, and thus determine the linear elastic behavior of such materials. The authors have determined the influence of relative density on Young's moduli in the principal material [001], face diagonal [011], and space diagonal [111] directions and relevant deformation behavior of each of the base cells. By comparing the results from different FEM modeling approaches, it has been concluded that the accuracy strongly depends on the chosen geometry and main deformation mechanisms, but that the beam elements are overall capable of correctly representing the mechanical behavior of such materials. From the comparison of the finite size model and experimental results, it has been shown that imperfections strongly influence the results of the structures with a pronounced directional sensitivity (e.g. SC cell). For the remaining cases (BCC, RBCC, and GA cells), the experimental and numerical results have been in good agreement.

In [14], the polymer lattice structures with various base cells (the same ones as in [11] with the addition of Kelvin (KV) base cell) have been also modeled both as a finite and infinite medium, but the focus has been on the linear viscoelastic behavior of such materials. The perfect geometry of the base cell has been assumed, which gives rise to the cubic material symmetry. For the computation of the elasticity tensor of such material, only three independent material parameters are required, and thus only three different load cases have been modeled. In this work, the authors chose the effective bulk modulus $\tilde{K}$ obtained from the hydrostatic tensile load case, the effective shear modulus $\tilde{M}$ obtained from the simple shear load case, and the effective shear modulus $\tilde{G}$ obtained from the 45° shear load case as the required material parameters.

The main aim of [4] has been to analytically, numerically, and experimentally assess the quasi-static compression behavior of the lattice structure with a BCC base cell made of stainless steel 316L. The specimens have been manufactured by selective laser melting technology, and the mechanical properties of the stainless steel 316L have been determined via the tensile test of a specially designed multi-strut specimen. Additionally, a bilinear elastoplastic material model with isotropic hardening has been defined. During the manufacturing process, due to the heat transfer phenomenon (i.e. difference in heat transfer between different areas of the specimen), it comes to the formation of irregular metallic particle clusters (aggregates), which leads to the deviation of size and shape of the strut cross-section. The authors have assessed the actual diameters of the specimen via the optical digitalization process. From these scans, two approximations of the actual cross-section have been determined, one circular and one elliptical (both larger than the nominal diameter). The experimental setup of the uniaxial compression test for the lattice structures has been described in detail. The numerical FEM modeling

approach has been based on a finite medium lattice model made from quadratic tetrahedral continuum elements, quadratic Timoshenko beam elements, and a modified quadratic Timoshenko beam element approach, where both stiffness and diameter in the vicinity of the vertices have been increased. Both linear and nonlinear behavior of models under uniaxial compression have been assessed. The implemented analytical approaches have been based on modified Timoshenko and Euler-Bernoulli beam theories. For numerical models with modified beam elements and analytical approaches, in addition to struts with nominal cross-section, adjusted circular and elliptical shapes have been also studied and compared to the experimental results. With this approach, the influence of geometrical imperfections on the results has been considered. Lastly, the results from all approaches have been obtained and compared for various slenderness ratio values of struts. From the comparison of the experimental and analytical results, it has been concluded that the Timoshenko theory with elliptical cross-section has delivered the most accurate results, and the Euler-Bernoulli theory with adjusted circular cross-section has been the least accurate. For the linear material behavior, the results from the FEM models have been almost the same as the experimental ones for the smaller values of the slenderness ratio. For the non-linear elastoplastic material behavior, the modified beam element model with elliptical cross-section has been closest to the experimental results.

2. Theory overview

2.1 Cellular materials

Cellular materials are present in different forms in various engineering fields and nature - from bone interior and wood to packaging, insulation, and energy absorption applications [10, 13]. They can be classified into stochastic cell structures (foam) or periodic cell structures (lattice), depending on the base cell arrangement [13]. Additional categorization into the open-celled and close-celled cellular structures can be made depending on whether the voids are topologically connected or not [3]. The representatives of each subclass are shown in *Fig. 2.1*. One of the prevailing artificial cellular materials, and of interest in this work, are open-celled periodic lattice structures. The material properties of these structures depend on the base cell configuration and can be customized to suit the specific needs of various engineering fields. Additionally, they are characterized by high specific strength and stiffness, and outstanding energy absorption capacity [11, 5, 13]. Some of the possible base cell architectures are shown in *Fig. 2.2*. In this work, the focus will be on the BCC unit cell and corresponding lattice structure.

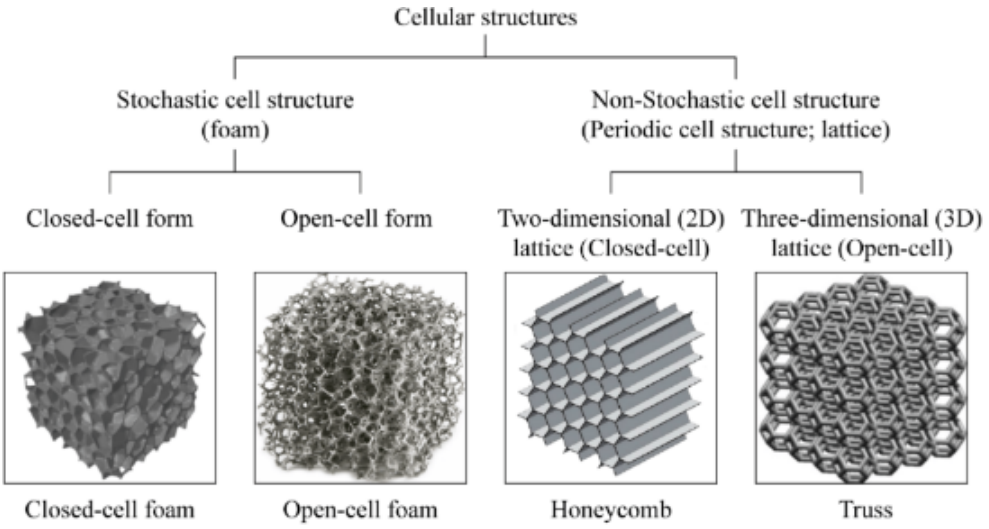

Fig. 2.1 Categorization of the cellular structures and some representatives for each of the subclasses. [13]

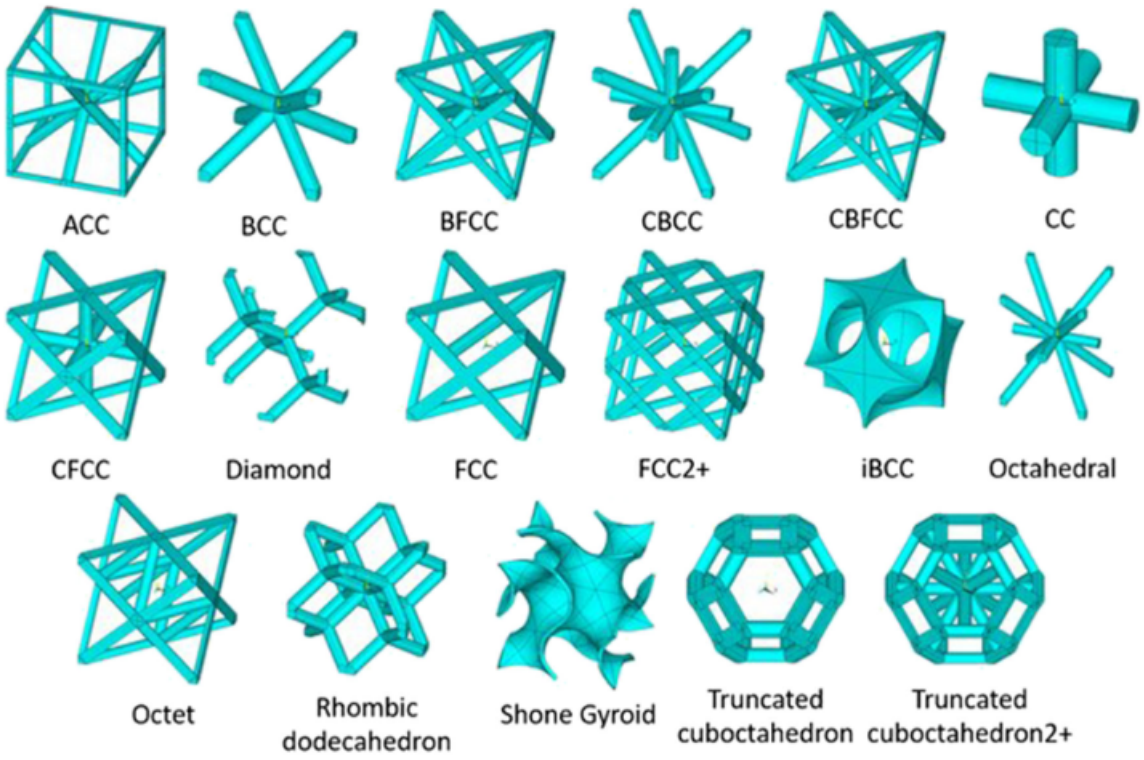

Fig. 2.2 Some of the possible base cell architectures. [17]

2.2 Continuum micromechanics

Open-celled lattice structures can be observed and analyzed on different length scales (macroscale, mesoscale, and microscale) that are considerably separated from each other. For example, the macroscale can be defined as the length scale of a component made from open-celled lattice material, the mesoscale as the length scale of the small specimen for an experiment, and the microscale as the length scale of the base cell (material level) [3, 14]. The focus of this work is on the continuum micromechanics, specifically on the homogenization principles. The aim is to evaluate the relationship between the overall mechanical response of the inhomogeneous material and the phase geometries and arrangements on the microscale. For that, a bridging of different length scales is required. This can be achieved through homogenization, where the behavior at the larger scale can be obtained from the response at the smaller one, i.e. the goal is to find equivalent homogeneous material which has the same properties as the open-celled lattice structure. Since the structure of the observed microgeometry can be very complex, approximations for homogenization are needed, and they can be divided into two categories. The first one is based on the highly idealized volume elements and statistical information, which observe the collective interactions between phases or regions. The second category is based

on the specific microgeometries, which observe very detailed interactions between phases or regions on the microscale. This work specifically focuses on the Periodic Microfield Approaches (PMAs), which belong to the latter category. Typically, PMAs are handled numerically, with the Finite Element Method (FEM) being the most popular and effective approach.

The PMAs are based on the assumption that the heterogeneous material can be regarded as periodic. Through the repeating unit cell (UC), the structure of such periodic material can be described. The overall behavior of a material is then estimated by evaluating the UC's response. Such volume elements need a periodic phase structure and boundary conditions that impose periodicity. In general, countless different UCs can be chosen from the same system. It is essential that the compatibility between neighboring UCs is fulfilled, which means that there are no overlaps or gaps in the system – they must fit with each other perfectly in both deformed and undeformed states.

The boundary conditions can be divided into periodicity, symmetry, and antisymmetry. Although their implementation in FEM can be challenging, the periodic boundary conditions (PBCs) are the most general and appropriate, because they can deal with any possible deformation of the UC, and that is why they are implemented in this work. For PBCs to be implemented, the UC can only have paired faces, which are always parallel, and of the same size, shape, and arrangement. Additionally, these paired faces are meshed in the same way, i.e. they have the same number of nodes at the same positions (homologous nodes). If these requirements are fulfilled, the periodicity can be imposed through the series of multipoint constraints (linear equations) between the nodes' DOFs.

Two methods can be used to subject the UCs to specific loads - the asymptotic homogenization and the method of macroscopic degrees of freedom. The latter is based on the usage of the master nodes and slave regions defined on the UC boundary. The displacements of slave nodes and regions are fully controlled by the displacements of the master nodes and their corresponding regions. Concentrated forces or displacements are applied on the master nodes, which are then transferred to the enslaved regions via multi-point constraints. This method allows a more straightforward estimation of the reaction forces in the system since all reaction forces of coupled degrees of freedom (DOFs) will be summed on the corresponding master node.

A common notation system of the master and slave nodes and regions for a cubic three-dimensional (3D) UC is shown in *Fig. 2.3*. The lettering of W, E, S, and N corresponds to the four cardinal directions, i.e. N - North, S - South, W - West, and E - East. The remaining two faces denote T - Top and B - Bottom. The nodes SEB, NWB, SWT, and SWB are master nodes, with corresponding master regions S, W, B, SB, WB, and SW. The remaining four nodes SET, NET, NWT, and NEB are slave nodes, which are constrained to the displacements of the master nodes. The remaining regions N, E, T, NT, NB, NW, NE, SE, EB, ET, ST, and WT are slave regions.

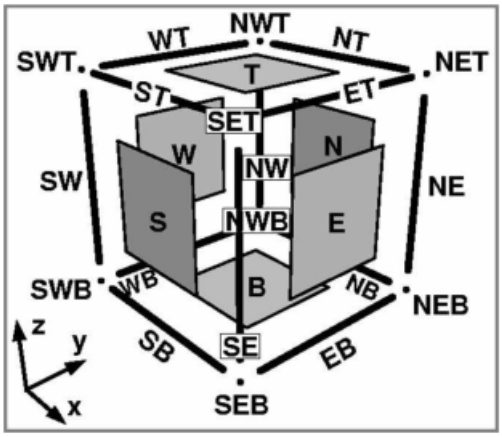

Fig. 2.3 The notation system for the master nodes and regions, as well as the slave nodes and regions of a 3D cubic UC. The lettering of W, E, S, and N corresponds to the four cardinal directions, i.e. N - North, S - South, W - West, and E - East. The remaining two faces denote T - Top and B - Bottom. [3]

2.2.1 Periodic boundary conditions

In *Fig. 2.4*, an example of a two-dimensional (2D) rectangular UC with applied PBCs is shown. The nodes NW and SE are master nodes, with corresponding master regions S and W. Node SW is the anchor node (i.e. it is fixed), and NE is a slave node, with corresponding slave regions E and N. The shift vectors in the undeformed ($\mathbf{c_{1|2}}$) and deformed ($\hat{\mathbf{c}}_{\mathbf{1|2}}$) states, that connect the paired homologous nodes, and the local coordinate system on each of the paired faces, with coordinates of the paired homologous nodes $\tilde{s}_{1|2}$, are defined.

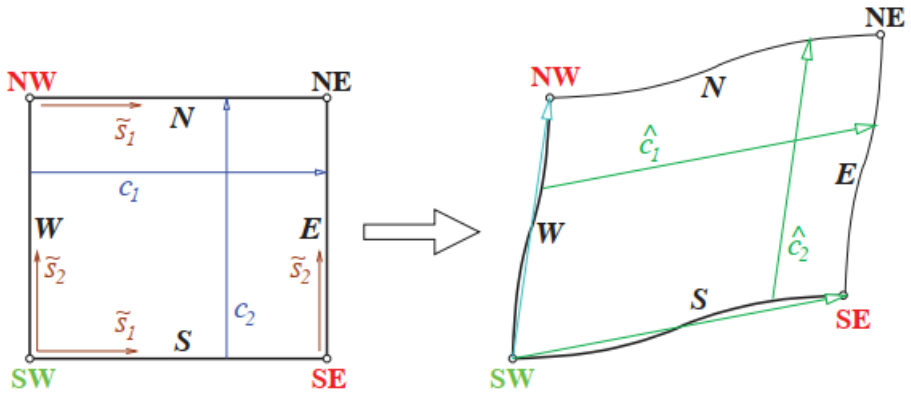

Fig. 2.4 Sketch of the PBCs applied to a 2D rectangular UC. The notation system corresponds to *Fig. 2.3*, with the SW master node as the anchor. The $\mathbf{c_k}$ and $\hat{\mathbf{c}}_\mathbf{k}$ represent shift vectors between the pairs of homologous nodes in the undeformed and deformed state respectively. The $\tilde{s}_k$ are coordinates of the paired homologous nodes in the local coordinate system on each of the paired faces. [3]

For this special case, and considering $\mathbf{u}_{\mathrm{SW}} = 0$ (anchor node), the PBCs can be formulated via equations

$$\mathbf{u}_{\mathrm{N}}(\tilde{s}_1) = \mathbf{u}_{\mathrm{S}}(\tilde{s}_1) + \mathbf{u}_{\mathrm{NW}}, \tag{2.1}$$

$$\mathbf{u}_{\mathrm{E}}(\tilde{s}_2) = \mathbf{u}_{\mathrm{W}}(\tilde{s}_2) + \mathbf{u}_{\mathrm{SE}}, \tag{2.2}$$

$$\mathbf{u}_{\mathrm{NE}} = \mathbf{u}_{\mathrm{NW}} + \mathbf{u}_{\mathrm{SE}}, \tag{2.3}$$

where $\mathbf{u}$ are the displacement vectors of corresponding nodes. The same concept can be analogously extended to a three-dimensional (3D) UC model. These equations are implemented in FEM packages via multipoint constraints. Although the implementation of PBCs is exceptionally advantageous regarding the loading possibilities of the UC, there is an increased pre-processing and computational effort.

The rotational DOFs of beam elements must be coupled appropriately to maintain periodicity and to avoid the appearance of ”hinges”.

2.2.2 Effective Young's modulus $\tilde{E}$

For the rectangular or hexahedral UCs aligned with the coordinate system axes, in the small strain regime, the determination of averaged stresses is simplified and the required equation reads as

$$\tilde{\sigma} = \frac{F_{\mathrm{R}}}{A}, \tag{2.4}$$

with the reaction (or applied) forces F_{R} in the master nodes and the area of the UC faces A. The averaged strain $\tilde{\varepsilon}$ reads as

$$\tilde{\varepsilon} = \frac{u}{l}, \tag{2.5}$$

with the displacement in the deformation direction of the master node u, and the corresponding length of edge l of the UC. For the uniaxial stress load cases, where the stress component in only one direction is different from zero, Hooke's law is simplified, and from it, the equation for effective Young's modulus reads as

$$\tilde{E} = \frac{\tilde{\sigma}}{\tilde{\varepsilon}}. \tag{2.6}$$

2.2.3 Effective bulk modulus $\tilde{K}$

The effective bulk modulus $\tilde{K}$ is determined from the hydrostatic load case. Under the hydrostatic load, the specimen experiences uniform stresses from all directions, e.g. condition as if it were submerged under water (for hydrostatic compressive load case). The corresponding stress tensor is a diagonal tensor, and its components have equal values (i.e. only normal stresses are different from zero, and are equal to each other). For a material with a cubic material symmetry, the same is true for the strain tensor. This type of loading only causes a volume change, but no change in shape (distortion). The bulk modulus K relates volumetric strain ε_{vol} to the mean stress σ_m [15]. The mean stress is defined as

$$\tilde{\sigma}_m = \frac{1}{3}\sum_{i=1}^{3}\tilde{\sigma}_{ii} = \frac{\tilde{\sigma}_{xx} + \tilde{\sigma}_{yy} + \tilde{\sigma}_{zz}}{3}, \tag{2.7}$$

with $\tilde{\sigma}_{ii}$ obtained from Eq.(2.4).

The correct reaction forces at the corresponding master nodes have to be chosen. For $\tilde{\sigma}_{xx}$, a reaction force in the x-direction at the SEB master node, for $\tilde{\sigma}_{yy}$, a reaction force in the y-direction at the NWB master node, and for $\tilde{\sigma}_{zz}$, a reaction force in the z-direction at the SWT master node. The equation for volumetric strain reads

$$\tilde{\varepsilon}_{\text{vol}} = \sum_{i=1}^{3} \tilde{\varepsilon}_{ii} = \tilde{\varepsilon}_{xx} + \tilde{\varepsilon}_{yy} + \tilde{\varepsilon}_{zz}, \tag{2.8}$$

where, for a material with cubic symmetry, $\tilde{\varepsilon}_{xx} = \tilde{\varepsilon}_{yy} = \tilde{\varepsilon}_{zz}$, which are obtained analogous to Eq.(2.5). Finally, the bulk modulus value is obtained from

$$\tilde{K} = \frac{\tilde{\sigma}_m}{\tilde{\varepsilon}_{\text{vol}}}. \tag{2.9}$$

2.2.4 Effective shear modulus $\tilde{M}$

The effective shear modulus $\tilde{M}$ is obtained from the simple shear load case, where all normal stress components are zero, and only one shear stress component in principal material coordinates is different from zero. The requirements for this load case are that the opposing faces must remain parallel throughout the deformation and that there is displacement only in the deformation direction. The equation for the corresponding averaged shear stress reads

$$\tilde{\tau} = \frac{F_{\text{R}}}{A}, \tag{2.10}$$

with the reaction (or applied) forces F_{R} in the master nodes and the area of the UC faces A. For this specific case (simple shear in the x-y plane), the reaction force in the y-direction at the SEB master node is required. The shear angle is determined via the displacement of the master node and the undeformed length of the UC's corresponding edge. For the deformation in the y-direction observed in the x-y plane, the equation reads

$$\tilde{\gamma}_{xy} = \frac{u_y}{l_x}, \tag{2.11}$$

with u_y as the displacement of the master node in the y-direction, and l_x as the undeformed length of the corresponding edge.

Finally, the effective shear modulus can be determined via the effective shear stress and shear angle, and its equation reads

$$\tilde{M} = \frac{\tilde{\tau}_{xy}}{\tilde{\gamma}_{xy}}. \tag{2.12}$$

2.2.5 Effective shear modulus $\tilde{G}$

The effective shear modulus $\tilde{G}$ is determined from the 45° shear load case, which corresponds to simple or pure shear related to the coordinate system which has been rotated by 45° around the out-of-plane axis (e.g. around the z-axis for the shear in the x-y plane). It consists of a change in shape without shear in principal material coordinates (i.e. normal stresses that don't involve volume change) [14]. Such load case has a stress tensor form

$$\tilde{\boldsymbol{\sigma}} = \begin{pmatrix} \tilde{\sigma}_{xx} & 0 & 0 \\ 0 & \tilde{\sigma}_{yy} & 0 \\ 0 & 0 & 0 \end{pmatrix}, \tag{2.13}$$

and strain tensor form

$$\tilde{\boldsymbol{\varepsilon}} = \begin{pmatrix} \tilde{\varepsilon}_{xx} & 0 & 0 \\ 0 & \tilde{\varepsilon}_{yy} & 0 \\ 0 & 0 & 0 \end{pmatrix}, \tag{2.14}$$

where $\tilde{\varepsilon}_{yy} = -\tilde{\varepsilon}_{xx} = \tilde{\varepsilon}$, and $\tilde{\sigma}_{yy} = -\tilde{\sigma}_{xx} = \tilde{\sigma}$. These values are determined in the same manner as in the previous cases.

To obtain the desired pure or simple shear state, the stress and strain tensors must be rotated by 45° around the z-axis in the positive direction. The transformation matrix with form

$$\mathbf{Q_z} = \begin{pmatrix} cos(\phi) & sin(\phi) & 0 \\ -sin(\phi) & cos(\phi) & 0 \\ 0 & 0 & 1 \end{pmatrix} \tag{2.15}$$

is implemented, with $\phi = 45°$.

The transformation equation for the stress tensor reads

$$\tilde{\boldsymbol{\sigma}}' = \mathbf{Q_z} \cdot \tilde{\boldsymbol{\sigma}} \cdot \mathbf{Q_z}^{\mathbf{T}}, \tag{2.16}$$

and an analogous one is used for the strain tensor. After the transformation, the stress tensor

$$\tilde{\boldsymbol{\sigma}}' = \begin{pmatrix} 0 & \tilde{\sigma} & 0 \\ \tilde{\sigma} & 0 & 0 \\ 0 & 0 & 0 \end{pmatrix}, \tag{2.17}$$

and strain tensor

$$\tilde{\boldsymbol{\varepsilon}}' = \begin{pmatrix} 0 & \tilde{\varepsilon} & 0 \\ \tilde{\varepsilon} & 0 & 0 \\ 0 & 0 & 0 \end{pmatrix} \tag{2.18}$$

forms are obtained. The required effective shear modulus $\tilde{G}$ is obtained via

$$\tilde{G} = \frac{\tilde{\sigma}}{2\tilde{\varepsilon}} = \frac{-\tilde{\sigma}_{xx}}{-2\tilde{\varepsilon}_{xx}} = \frac{\tilde{\sigma}_{yy}}{2\tilde{\varepsilon}_{yy}}. \tag{2.19}$$

For the isotropic material behavior, the moduli $\tilde{G}$ and $\tilde{M}$ are equal.

Suppose a general stress tensor is decomposed into its pressure and deviatoric components, and likewise the strain one into the volume change and strain deviator. In that case, the modulus $\tilde{M}$ relates the non-diagonal ("shear") components of deviatoric stress and strain contributions, whereas the modulus $\tilde{G}$ relates the diagonal ("normal") components of these contributions [14]. As previously mentioned, the bulk modulus $\tilde{K}$ relates volume change and pressure contributions. This decoupling allows the implementation of various loading scenarios where either each of the individual moduli is targeted, or some combination of them can be "activated" [14].

2.2.6 Effective elasticity tensor

The BCC lattice UC shows cubic material symmetry and to obtain the effective elasticity tensor of such material, three independent material parameters are required [15, 14]. Many different ones can be chosen, but in this work, the effective bulk modulus $\tilde{K}$, effective shear modulus $\tilde{M}$, and effective shear modulus $\tilde{G}$ are selected.

For a material with cubic symmetry and K, M, and G as chosen parameters, Hooke's law in the Voigt-Nye notation can be written as

$$\begin{pmatrix} \sigma_{xx} \\ \sigma_{yy} \\ \sigma_{zz} \\ \tau_{xz} \\ \tau_{yz} \\ \tau_{xy} \end{pmatrix} = \begin{pmatrix} K+\frac{4G}{3} & K-\frac{2G}{3} & K-\frac{2G}{3} & 0 & 0 & 0 \\ K-\frac{2G}{3} & K+\frac{4G}{3} & K-\frac{2G}{3} & 0 & 0 & 0 \\ K-\frac{2G}{3} & K-\frac{2G}{3} & K+\frac{4G}{3} & 0 & 0 & 0 \\ 0 & 0 & 0 & M & 0 & 0 \\ 0 & 0 & 0 & 0 & M & 0 \\ 0 & 0 & 0 & 0 & 0 & M \end{pmatrix} \begin{pmatrix} \varepsilon_{xx} \\ \varepsilon_{yy} \\ \varepsilon_{zz} \\ \gamma_{xz} \\ \gamma_{yz} \\ \gamma_{xy} \end{pmatrix}. \tag{2.20}$$

2.3 Finite element method

The Finite Element Method is a numerical method for solving partial differential equations (PDEs), which can handle complex geometries and loading cases, and is applicable in different fields of physics and engineering. Different software packages are available on the market, and the one used in this work is *Abaqus/Standard 2023 (Dassault Systèmes Simulia Corp., Johnston, Rhode Island, United States)*. In [1], detailed information about various elements, constraints, and the FEM itself is given. A variety of finite elements can be used in modeling, and their different properties are generally influenced by the type, degrees of freedom, number of nodes, integration, and formulation. This study will employ continuum (solid) and beam elements.

Continuum elements are the most used finite elements because of their versatility. They can be used to form complex geometries and support many different loads. These elements have only translational DOFs on nodes and can have linear or quadratic interpolation. Their shapes can range from quadrilateral and triangular for 2D and hexahedral to tetrahedral for 3D. Hexahedral elements should be the most effective, mainly if they are rectangular because they have a high accuracy at a lower computational cost. The results from the linear tetrahedral elements are not as accurate, especially in the elasticity problems, since they are overly stiff. However, these elements are especially suitable for

complex geometries because the lower effort for meshing is required, in comparison to the hex elements. Alternatively, implementing second-order tetragonal elements can improve the accuracy of the results.

Beams are structural elements that possess translational and rotational DOFs on nodes. Based on the assumption that the dimensions along the axial direction of the beam are substantially larger than the proportions of the cross-section, the beam is reduced from a 3D structure to a "one-dimensional" line element. The cross-section and orientation of the beam need to be defined for the computations. The beam can be formulated with Euler-Bernoulli or Timoshenko beam theory. In the former case, the beam cross-section is always assumed to remain plane and perpendicular to the beam axis, thus ignoring the influence of transverse shear deformations. In the Timoshenko shear-flexible formulation, the cross-section is also assumed to be plane but does not have to be perpendicular to the axis. In this type of element, only the stress component along the axis, transverse shear stress, and shear stress caused by torsion in 3D are evaluated. The transverse shear stress does not contribute to plasticity in the beam elements [1]. The most significant influence of the shear deformation can be seen in thick beams. For the slender ones, this influence is almost insignificant [1]. The results of a beam element in post-processing are always shown in its local orientation. In general, this type of element is beneficial because of its simplistic structure, but it is not suitable for every model.

Constraints are needed to model the kinematic relations. The one used in this work is the "equation" multi-point constraint (MPC) that creates relations between specific DOFs of the defined regions through linear equations. It introduces the constraint forces at coupled DOFs, which are considered to be external but do not appear in the reaction force output. More detailed information regarding its functioning and implementation can be found in [1].

2.4 Yield surface

The yield surface is a graphical interpretation of the plastic flow criteria, which defines the material's elasticity limit, i.e. onset of yielding, under any possible stress state. For an isotropic material, it is usually visualized in terms of principal stresses (σ_1, σ_2, and σ_3), or invariants of stress tensor (I_1, I_2, and I_3). If the stress state is inside the surface, the material behavior is elastic, and if it is exactly at the boundary, yielding occurs. Otherwise, it cannot exist, since it is not allowed to be on the outside of the surface. By incorporating hardening laws, the surface can expand or move with increasing loads after

the initial yield point is reached, if the plastic deformation further evolves [15, 22, 18].

Some of the most common approaches are Tresca (maximum shear stress) and von Mises (J_2) yield criteria. The two-dimensional (2D) representations of their respective yield surface for a plane stress state ($\sigma_3 = 0$) and a general stress state in the deviatoric plane for an isotropic material are shown in *Fig. 2.5*. The deviatoric plane is defined as a view in the direction of the pure hydrostatic state (i.e., $\sigma_1 = \sigma_2 = \sigma_3$), which doesn't carry any shear stresses, and thus doesn't have any influence on the onset of yielding for the J_2 and Tresca criteria. Everything outside of this plane are hydrostatic contributions, while everything inside are deviatoric ones, which can activate the yield criteria. The Tresca yield surface is a hexagon in the 2D representation and a regular hexagon in the deviatoric plane, whereas the von Mises yield surface is an ellipse in the 2D representation and a circle in the deviatoric plane. The biggest difference between the two is in the pure shear stress state. Since this is an isotropic material, it doesn't matter how the stress state is oriented with respect to the material principal axis. This results in symmetric surfaces, where the onset of tensile and compressive yielding is the same. For an anisotropic material, there is a direction-dependent plastic behavior.

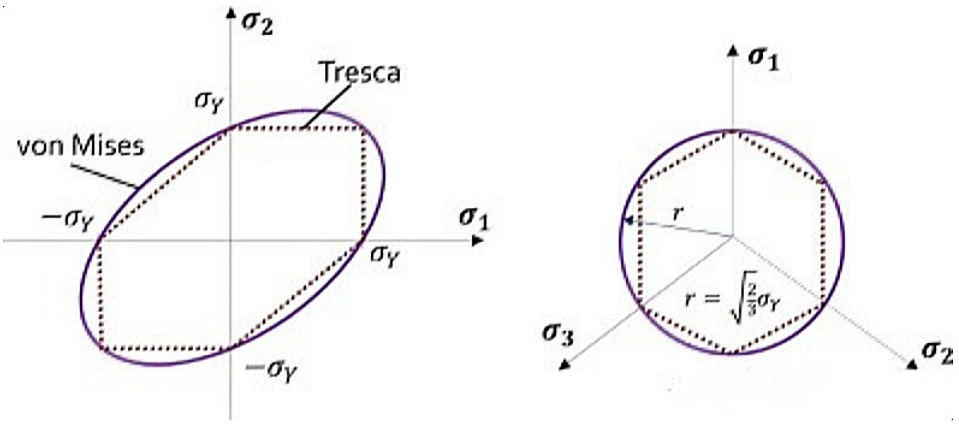

Fig. 2.5 The 2D representations of an isotropic material's Tresca and von Mises yield surface for a plane stress state ($\sigma_3 = 0$) (left) and a general stress state in the deviatoric plane (right). The yield stress σ_Y, and principal stresses σ_1, σ_2, and σ_3 are shown. [18]

3. Unit cell model

In this section, detailed information about geometry, materials, and modeling approaches of the BCC lattice UC model used in this work is given. The nomenclature of the master nodes and regions, as well as the slave nodes and regions of the UC, is based on *Fig. 2.3* discussed in chapter 2. Different load cases, both force and displacement-controlled, are implemented throughout this work via the method of macroscopic degrees of freedom. The finite element analysis is performed under the assumption of geometric linearity. The exact configuration of applied macroscopic BCs for individual load cases is given in further sections of this work.

The modeled UC has 4 x 4 x 4 mm dimensions with a strut diameter of 0.6 mm. It is modeled once with the quadratic tetrahedral (C3D10) continuum elements (*Fig. 3.1*) and once with the linear Timoshenko (shear flexible) beam elements in space (B31) (*Fig. 3.2*). The solid element model has 45 664 elements in total, with 12 elements along the diameter of the strut, whereas the beam model has 96 elements in total, with 12 elements along each strut. For the solid element model, the second-order tetragonal elements are implemented, since they are more accurate than the first-order ones, and also allow easier meshing of complex geometries (in comparison to the hex elements). Regarding the number of beam section points in the circular cross-section, the analyses with both default number (3 points radially, and 8 circumferentially - 17 in total) and increased number of section points (25 points radially and 60 points circumferentially - 1441 in total) are done.

The beam model was initially modeled to be larger (10 x 10 x 10 mm), and it had to be adjusted for the results to be comparable. To achieve this adjustment, the diameter of the strut of this model has been increased to 1.5 mm (scaled 2.5 times in comparison to the original). This can be done for this case since there are no damage or fracture mechanisms that are examined.

The periodic boundary conditions (PBCs) are implemented via *medtool45 (Dr. Pahr Ingenieurs e.U., Pfaffstätten, Austria)*, which generates the required ”equation” MPCs for the provided UC mesh. Additionally, for the beam element model, it has to be ensured that the rotational DOFs at the vertices of the cubic UC are constrained so that the PBCs are fulfilled. This can also be achieved via ”equation” MPCs, by coupling the rotational DOFs of seven nodes at vertices of the cube to the rotational DOFs of the remaining master node.

The results from beam models are expected to be less accurate than the ones from the solid element models, but the required computational and pre-processing effort is considerably lower, which is suitable for modeling complex lattice structures. These inaccuracies are primarily caused by their inability to correctly represent the sites where struts connect (neglecting the material aggregation and overlapping volumes at the junctions of multiple struts in the model), which leads to lower stiffness. This is especially visible in cases where the struts experience bending or shear deformations. The latter, in addition, do not contribute to plasticity in the beam elements.

In *Abaqus*, the orientation of a beam cross-section is described using a local, right-handed (t, n_1, n_2) axis system. Here, t represents the tangent to the axis of the element. The n_1 ("beam section axis") and n_2 ("normal to the beam") are the basis vectors that establish the local 1- and 2-directions of the cross-section, respectively [1]. The axial stress distribution of the beam element UC is studied in a further chapter of this work. In *Fig. 3.3*, the locations of the section points where these results are output are described. In this work, they are always positioned at the outermost fiber of the cross-section under 270° with respect to the positive 1-direction of the local coordinate system (e.g. blue point for that specific local orientation).

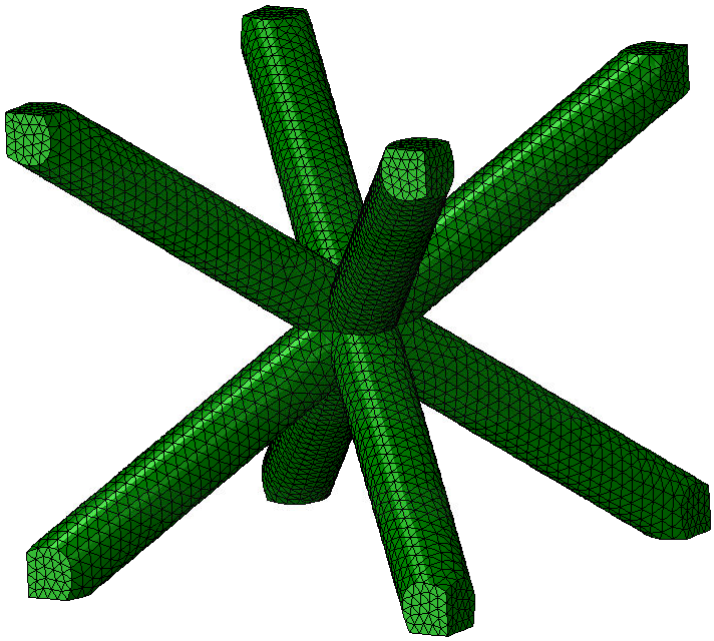

Fig. 3.1 UC modeled with quadratic tetrahedral (C3D10) continuum elements.

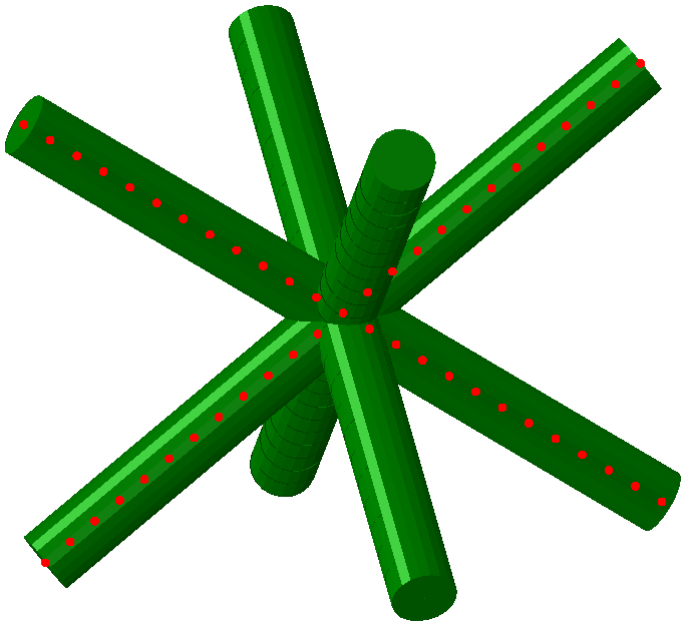

Fig. 3.2 UC modeled with linear beam (B31) elements (rendering of beam section active).

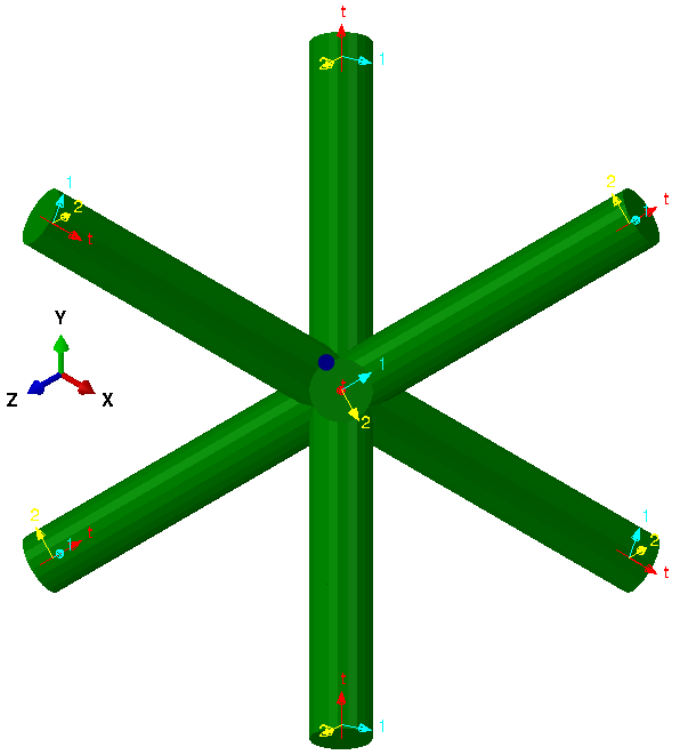

Fig. 3.3 The orientation of beam elements for each strut is described through the local coordinate system (t, n_1, n_2). The locations of section points where the results in this work are output are always positioned at the outermost fiber of the cross-section under 270° with respect to the positive 1-direction of the local coordinate system (e.g. blue point for that specific local orientation).

The bulk material is isotropic and its properties are shown in the *Tab. 3.1*.

The plastic behavior of the bulk material in this work is characterized through J_2 (von Mises) yield criterion and linear isotropic hardening model (i.e. bilinear plasticity), and its uniaxial engineering stress-strain curve is shown in *Fig. 3.4*. To model this in *Abaqus*, a set of data points from the corresponding true stress - logarithmic plastic strain diagram (*Fig. 3.5*) is provided.

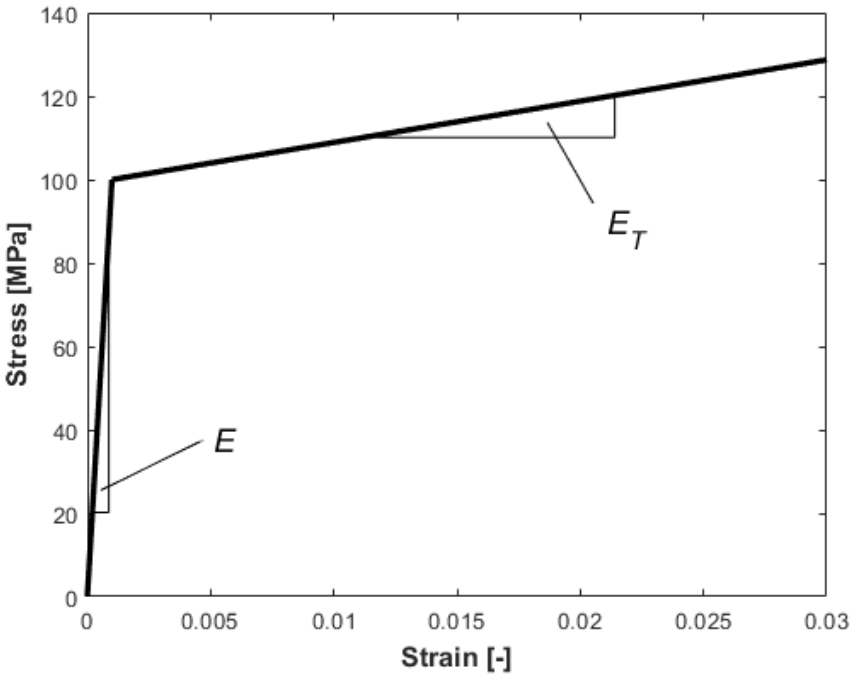

Fig. 3.4 Uniaxial engineering stress-strain curve of the bulk material, representing its bilinear plastic behavior. The slope of the curve in the linear elastic region (up to the yield stress) is defined as Young's modulus E. The slope in the linear hardening region is defined as tangent modulus E_T

Tab. 3.1 The material properties of the isotropic bulk material used for the UC model.

Young's modulus [MPa]	Poisson's ratio [-]	Hardening modulus [MPa]	Yield stress [MPa]
100 000	0.3	1000	100

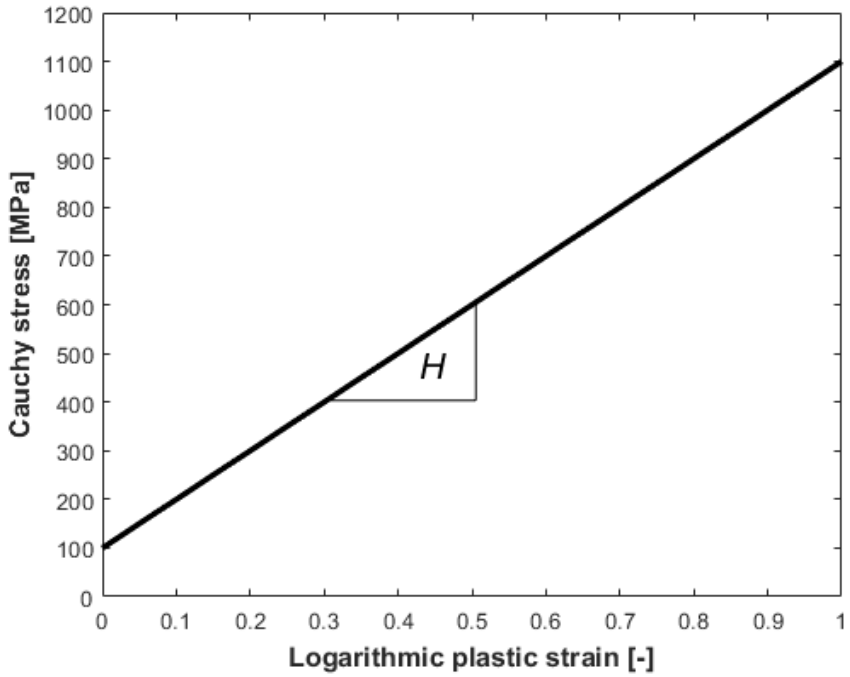

Fig. 3.5 The Cauchy (true) stress - logarithmic (true) plastic strain curve of the bulk material. The data points of the curve are used as the input of plastic behavior in *Abaqus*. Its slope corresponds to the hardening modulus H (or plastic modulus E_{P} in some literature [22]).

The implemented yield stress and hardening modulus values of the bulk material are found in *Tab. 3.1*. The damage initiation criterion and evolution are not modeled in this work. For small strains, the relation

$$H = \frac{E \cdot E_{\mathrm{T}}}{E - E_{\mathrm{T}}}, \tag{3.1}$$

between hardening modulus H, Young's modulus E, and tangent modulus E_{T} can be formulated [22].

If the final defined stress value in *Fig. 3.5* (in this case 1100 MPa) is exceeded, the model will behave ideally plastic (i.e. no hardening present from that point).

4. Elastic behavior

4.1 Introduction

In this section, the elastic properties of the BCC lattice UC are determined. This UC shows cubic material symmetry and to obtain the elasticity tensor of such material, three independent material parameters are required [15, 14]. Many different ones can be chosen, but in this work, the effective bulk modulus $\tilde{K}$, effective shear modulus $\tilde{M}$, and effective shear modulus $\tilde{G}$ are selected. The parameter $\tilde{K}$ is obtained from the hydrostatic tension load case, $\tilde{M}$ from the simple shear XY load case, and $\tilde{G}$ from the 45° shear XY load case [14]. Additionally, for the solid element modeling variant, the effective Young's moduli in the principal material direction [100], the face diagonal [110], and the space diagonal [111] are obtained.

4.2 Elasticity tensor computation

For a material with cubic material symmetry and effective bulk $\tilde{K}$, shear $\tilde{M}$, and shear $\tilde{G}$ moduli as chosen independent material parameters, the homogenized elasticity tensor can be computed according to Eq.(2.20). $\tilde{K}$ is determined via Eq.(2.9), $\tilde{M}$ via Eq.(2.12), and $\tilde{G}$ via Eq.(2.19).

The analysis is strain-controlled, and the required load cases are achieved by applying displacements to the master nodes (method of macroscopic degrees of freedom). The applied macroscopic BCs on the master nodes for each of the load cases are given in *Tab. 4.1*. The BCs for the uniaxial tension load case in the principal material direction [100] are also defined here, which will be required and referenced in subsequent sections. The applied displacement u for these models is chosen in a way that an engineering (nominal) strain of 1% is achieved.

Tab. 4.1 Applied macroscopic BCs to the UC for hydrostatic tension, simple shear XY, 45° shear XY, and uniaxial tension [100] load cases. The master node notation is based on *Fig. 2.3*. u is the desired displacement that is applied. The symbol "-" denotes that the "force-free" BC is present.

Load case	Master nodes	u_x	u_y	u_z
Hydrostatic tension	SWB	0	0	0
	SEB	u	0	0
	NWB	0	u	0
	SWT	0	0	u
Simple shear XY	SWB	0	0	0
	SEB	0	u	0
	NWB	0	0	0
	SWT	0	0	0
45° shear XY	SWB	0	0	0
	SEB	u	0	0
	NWB	0	$-u$	0
	SWT	0	0	0
Uniaxial tension [100]	SWB	0	0	0
	SEB	u	0	0
	NWB	0	-	0
	SWT	0	0	-

4.2.1 Results

The values of the effective material parameters $\tilde{K}$, $\tilde{M}$, and $\tilde{G}$, for both solid and beam element UC are shown in *Tab. 4.2*. The plots of deformed UC models and a description of the deformation behavior of these loading cases are discussed in detail in further sections of this work.

As already discussed, the accuracy of the simulation with the beam elements is lower than with the solid elements. Because of this, the values that are obtained from the beam model are slightly lower (the solid element UC is stiffer than the beam element one).

The influence of different deformation mechanisms of the struts on the overall stiffness of the BCC lattice UC can be assessed from the results. Depending on the load case, in addition to compression and tension, the struts can experience bending as well.

Tab. 4.2 Effective material parameters $\tilde{K}$, $\tilde{M}$, and $\tilde{G}$ obtained from the UC models.

	Eff. bulk modulus $\tilde{K}$ [MPa]	Eff. shear modulus $\tilde{M}$ [MPa]	Eff. shear modulus $\tilde{G}$ [MPa]
Beam el. UC	1360.35	1374.73	43.16
Solid el. UC	1625.89	1462.33	69.37

From the load cases that are examined in this report, the highest bending deformation is present for the 45° shear XY load case. Here, the struts deform the easiest, and as a result, the UC has the lowest stiffness. This is reflected by the fact that the corresponding effective shear modulus $\tilde{G}$ has the lowest value.

For the hydrostatic tension load case, the struts experience only pure tension, and the BCC lattice UC has a high stiffness.

For the simple shear XY load case, two pairs of struts are stretched, while the other two are compressed. In addition to this, some bending deformation is present as well. Since the deformation is more stretch-dominated, the UC has good stiffness under this load case.

In conclusion, the effective elasticity tensor obtained from the results of the beam model reads

$$\tilde{\mathbf{E}}_{\mathbf{Beam}} = \begin{pmatrix} 1417.89 & 1331.58 & 1331.58 & 0 & 0 & 0 \\ 1331.58 & 1417.89 & 1331.58 & 0 & 0 & 0 \\ 1331.58 & 1331.58 & 1417.89 & 0 & 0 & 0 \\ 0 & 0 & 0 & 1374.73 & 0 & 0 \\ 0 & 0 & 0 & 0 & 1374.73 & 0 \\ 0 & 0 & 0 & 0 & 0 & 1374.73 \end{pmatrix} \text{[MPa]}, \tag{4.1}$$

and the one from the results of the solid element UC model reads

$$\tilde{\mathbf{E}}_{\mathbf{Solid}} = \begin{pmatrix} 1718.39 & 1579.64 & 1579.64 & 0 & 0 & 0 \\ 1579.64 & 1718.39 & 1579.64 & 0 & 0 & 0 \\ 1579.64 & 1579.64 & 1718.39 & 0 & 0 & 0 \\ 0 & 0 & 0 & 1462.33 & 0 & 0 \\ 0 & 0 & 0 & 0 & 1462.33 & 0 \\ 0 & 0 & 0 & 0 & 0 & 1462.33 \end{pmatrix} \text{[MPa]}. \tag{4.2}$$

4.3 Effective Young's moduli in the [100], [110], and [111] directions

In this section, the effective Young's moduli in the principal material direction [100], the face diagonal [110], and the space diagonal [111] of the BCC lattice UC are determined. The effective material parameters in the [110] and [111] directions are only computed for the solid element UC since the results are more accurate for this model. The force-controlled FEA is implemented. As an alternative to the method presented in this work, the elasticity tensor could be rotated to the desired direction and then inverted to obtain the compliance tensor. From this tensor, the effective Young's modulus value in this specific direction can be easily obtained.

4.3.1 The [100]-direction

For the principal material direction, a uniaxial stress state along the x-direction is applied

$$\tilde{\boldsymbol{\sigma}}_{\mathbf{100}} = \begin{pmatrix} \tilde{\sigma} & 0 & 0 \\ 0 & 0 & 0 \\ 0 & 0 & 0 \end{pmatrix}, \tag{4.3}$$

with resulting strain tensor

$$\tilde{\boldsymbol{\varepsilon}}_{\mathbf{100}} = \begin{pmatrix} \tilde{\varepsilon}_{xx} & 0 & 0 \\ 0 & \tilde{\varepsilon}_{yy} & 0 \\ 0 & 0 & \tilde{\varepsilon}_{zz} \end{pmatrix}, \tag{4.4}$$

where $\tilde{\varepsilon}_{yy} = \tilde{\varepsilon}_{zz}$.

The BCs that are applied to the master nodes of the UC are shown in *Tab. 4.3*.

Computed according to Eq.(2.6), the value of the effective Young's modulus in the [100] direction of the solid element UC is $\tilde{E}_{100} = 204.83$ MPa, and of the beam element one $E_{\mathrm{B100}} = 128.11$ MPa.

A relatively low values of the effective modulus are obtained for this load case, due to the strong bending deformation of the struts. The bending deformation here is lower compared to the 45° shear load case.

Tab. 4.3 The macroscopic BCs that are applied to the UC to obtain the effective Young's modulus in the material direction [100]. The parameter F is the desired force that is applied.

Load case	Master nodes	u_x	u_y	u_z	F_x	F_y	F_z
[100] direction	SWB	0	0	0	-	-	-
	SEB	-	0	0	F	-	-
	NWB	0	-	0	-	free	-
	SWT	0	0	-	-	-	free

4.3.2 The [110]-direction

The stress tensor for the uniaxial tension load case in the [110] direction, where the x-direction is aligned with the face diagonal, read as

$$\tilde{\boldsymbol{\sigma}}_{\mathbf{110}} = \begin{pmatrix} \tilde{\sigma} & 0 & 0 \\ 0 & 0 & 0 \\ 0 & 0 & 0 \end{pmatrix}, \tag{4.5}$$

with resulting strain tensor

$$\tilde{\boldsymbol{\varepsilon}}_{\mathbf{110}} = \begin{pmatrix} \tilde{\varepsilon}_{xx} & 0 & 0 \\ 0 & \tilde{\varepsilon}_{yy} & 0 \\ 0 & 0 & \tilde{\varepsilon}_{zz} \end{pmatrix}. \tag{4.6}$$

By rotating the stress and strain tensor by 45° around the z-axis in the negative direction, analogous to Eq.(2.16), they are returned to the principal material directions, and the stress tensor form reads as

$$\tilde{\boldsymbol{\sigma}}_{\mathbf{110}}{}' = \begin{pmatrix} \tilde{\sigma}' & \tilde{\sigma}' & 0 \\ \tilde{\sigma}' & \tilde{\sigma}' & 0 \\ 0 & 0 & 0 \end{pmatrix}, \tag{4.7}$$

with resulting strain tensor

$$\tilde{\boldsymbol{\varepsilon}}_{\mathbf{110}}{}' = \begin{pmatrix} \tilde{\varepsilon}'_{xx} & \tilde{\varepsilon}'_{xy} & 0 \\ \tilde{\varepsilon}'_{xy} & \tilde{\varepsilon}'_{yy} & 0 \\ 0 & 0 & \tilde{\varepsilon}'_{zz} \end{pmatrix}, \tag{4.8}$$

where $\tilde{\varepsilon}'_{xx} = \tilde{\varepsilon}'_{yy}$.

In conclusion, to obtain the effective modulus in the face diagonal direction [110], the two-dimensional stress state

$$\tilde{\boldsymbol{\sigma}}_{\mathbf{110|A}} = \begin{pmatrix} \tilde{\sigma} & \tilde{\sigma}_{\mathrm{R}} & 0 \\ \tilde{\sigma} & \tilde{\sigma} & 0 \\ 0 & 0 & 0 \end{pmatrix}, \tag{4.9}$$

should be applied to the UC, i.e. the equal loads in both x and y-directions introduced to the SEB and NWB master nodes in the x-y plane ($\tilde{\sigma}_{\mathrm{R}} = \tilde{\sigma}$). To avoid rigid body rotations, and achieve this desired load state, the displacement of the SEB node in the y-direction is coupled to the displacement of the NWB in the x-direction. This coupling ($u_{y|\mathrm{SEB}} = u_{x|\mathrm{NWB}}$) is possible because of the cubic material symmetry and the cubic UC, and it is achieved via the equation MPC, which introduces the constraint forces at coupled DOFs ($\tilde{\sigma}_{\mathrm{R}}$). These constraint forces are considered to be external but do not appear in the reaction force output [1]. The applied macroscopic BCs for this load case are shown in *Tab. 4.4*. Afterward, the stress and strain tensor are rotated by 45° around the z-axis in the positive direction according to Eq.(2.16). The same transformation matrix $\mathbf{Q_z}$ (Eq.(2.15)), previously used to obtain the effective shear modulus $\tilde{G}$ is implemented here.

Finally, computed according to Eq.(2.6), the value of the effective Young's modulus in the [110] direction of the solid element UC is $\tilde{E}_{110} = 761.25$ MPa.

Tab. 4.4 The macroscopic BCs that are applied to the UC to obtain the effective Young's modulus in the face diagonal direction [110]. The parameter F is the desired force that is applied.

Load case	Master nodes	u_x	u_y	u_z	F_x	F_y	F_z
[110] direction	SWB	0	0	0	-	-	-
	SEB	-	$= u_{x\|\mathrm{NWB}}$	0	F	-	-
	NWB	-	-	0	F	F	-
	SWT	0	0	-	-	-	free

4.3.3 The [111]-direction

The stress tensor for the uniaxial tension load case in the [111] direction of the UC with the cubic material symmetry, where the z-direction is aligned with the space diagonal, while the x and y-axes point towards the corners of the "hexagon", reads as

$$\tilde{\boldsymbol{\sigma}}_{\mathbf{111}} = \begin{pmatrix} 0 & 0 & 0 \\ 0 & 0 & 0 \\ 0 & 0 & \tilde{\sigma} \end{pmatrix}, \tag{4.10}$$

with resulting strain tensor

$$\tilde{\boldsymbol{\varepsilon}}_{\mathbf{111}} = \begin{pmatrix} \tilde{\varepsilon}_{xx} & 0 & 0 \\ 0 & \tilde{\varepsilon}_{yy} & 0 \\ 0 & 0 & \tilde{\varepsilon}_{zz} \end{pmatrix}, \tag{4.11}$$

where $\tilde{\varepsilon}_{xx} = \tilde{\varepsilon}_{yy}$.

The stress and strain tensor have to be rotated three times to return to the principal material directions. First rotation by 45° around the z-axis in the positive direction, then rotation by $\approx 54.74°$ around the y-axis in the negative direction, and finally rotation by 45° around the z-axis in the negative direction. The transformation matrix for the rotation around the z-axis, $\mathbf{Q_z}$, is already defined in Eq.(2.15). The transformation matrix for the rotation around the y-axis reads as

$$\mathbf{Q_y} = \begin{pmatrix} cos(\phi) & 0 & -sin(\phi) \\ 0 & 1 & 0 \\ sin(\phi) & 0 & cos(\phi) \end{pmatrix}. \tag{4.12}$$

The obtained stress form after this transformation sequence reads as

$$\tilde{\boldsymbol{\sigma}}_{\mathbf{111}}{}' = \begin{pmatrix} \tilde{\sigma}' & \tilde{\sigma}' & \tilde{\sigma}' \\ \tilde{\sigma}' & \tilde{\sigma}' & \tilde{\sigma}' \\ \tilde{\sigma}' & \tilde{\sigma}' & \tilde{\sigma}' \end{pmatrix}, \tag{4.13}$$

with resulting strain tensor

$$\tilde{\boldsymbol{\varepsilon}}_{\mathbf{111}} = \begin{pmatrix} \tilde{\varepsilon}'_{xx} & \tilde{\varepsilon}'_{xy} & \tilde{\varepsilon}'_{xz} \\ \tilde{\varepsilon}'_{xy} & \tilde{\varepsilon}'_{yy} & \tilde{\varepsilon}'_{yz} \\ \tilde{\varepsilon}'_{xz} & \tilde{\varepsilon}'_{yz} & \tilde{\varepsilon}'_{zz} \end{pmatrix}, \tag{4.14}$$

where all normal strains $\tilde{\varepsilon}_{ii}$ are equal to each other, and all shear strains $\tilde{\varepsilon}_{ij}$ are equal to each other.

In conclusion, to obtain the effective Young's modulus in the space diagonal direction, the stress state

$$\tilde{\boldsymbol{\sigma}}_{\mathbf{111|A}} = \begin{pmatrix} \tilde{\sigma} & \tilde{\sigma}_{\mathrm{R}} & \tilde{\sigma}_{\mathrm{R}} \\ \tilde{\sigma} & \tilde{\sigma} & \tilde{\sigma}_{\mathrm{R}} \\ \tilde{\sigma} & \tilde{\sigma} & \tilde{\sigma} \end{pmatrix}, \tag{4.15}$$

should be applied to the UC, i.e. the equal loads in all three directions (x, y, and z) introduced to the master nodes SEB, NWB, and SWT ($\tilde{\sigma}_{\mathrm{R}} = \tilde{\sigma}$). To avoid rigid body rotations and obtain the desired load case, the displacement of the SEB master node in the y-direction is coupled to the displacement of the NWB master node in the x-direction, and its displacement in the z-direction is coupled to the displacement of the SWT master node in the x-direction. The displacement of the NWB master node in the z-direction is coupled to the displacement of the SWT master node in the y-direction. These couplings ($u_{y|\mathrm{SEB}} = u_{x|\mathrm{NWB}}$, $u_{z|\mathrm{SEB}} = u_{x|\mathrm{SWT}}$, and $u_{z|\mathrm{NWB}} = u_{y|\mathrm{SWT}}$) are possible because of the cubic material symmetry and the cubic UC, and they are implemented via the equation MPC, which introduces the constraint forces at coupled DOFs ($\tilde{\sigma}_{\mathrm{R}}$). The applied macroscopic BCs for this load case are shown in *Tab. 4.5*.

Tab. 4.5 The macroscopic BCs that are applied to the UC to obtain the effective Young's modulus in the space diagonal direction [111]. The parameter F is the desired force that is applied.

Load case	Master nodes	u_x	u_y	u_z	F_x	F_y	F_z
[111] direction	SWB	0	0	0	-	-	-
	SEB	-	$= u_{x\|\mathrm{NWB}}$	$= u_{x\|\mathrm{SWT}}$	F	-	-
	NWB	-	-	$= u_{y\|\mathrm{SWT}}$	F	F	-
	SWT	-	-	-	F	F	F

Afterward, the stress and strain tensor are rotated in the following sequence - rotation by 45° around the z-axis in the positive direction, then rotation by $\approx 54.74°$ around the y-axis in the positive direction, and finally rotation by 45° around the z-axis in the negative direction. The final transformation matrix is achieved by multiplying the matrices corresponding to the rotation sequence

$$\mathbf{Q_{111}} = \mathbf{Q_{z/-45}} \cdot \mathbf{Q_{y/54.74}} \cdot \mathbf{Q_{z/45}} = \begin{pmatrix} 0.7887 & -0.2113 & -0.5774 \\ -0.2113 & 0.7887 & -0.5774 \\ 0.5774 & 0.5774 & 0.5774 \end{pmatrix}. \tag{4.16}$$

The equation for the transformation of the stress and strain tensor is analogous to Eq.(2.16).

Finally, computed according to Eq.(2.6), the value of the effective Young's modulus in the space diagonal direction [111] of the solid element UC is $\tilde{E}_{111} = 7975.26$ MPa.

4.3.4 Results

The values of effective Young's moduli in the [100], [110], and [111] directions of the solid element UC, and the one in the [100] direction of the beam element one are shown in *Tab. 4.6*.

For cubic materials, Young's moduli along the [100] and [111] directions represent extreme values (minimum and maximum) [12]. In this case, the [100] one represents the minimum, the [111] one is the maximum, whereas the [110] effective Young's modulus lies between them.

The difference in the values between the beam element and solid element UC models is due to already discussed inaccuracies of the beam element modeling approach.

Tab. 4.6 The values of the effective Young's moduli in the [100], [110], and [111] directions of the solid element UC, and of the beam element UC in the principal material direction E_{B100}.

$\tilde{E}_{100}$ [MPa]	$\tilde{E}_{110}$ [MPa]	$\tilde{E}_{111}$ [MPa]	E_{B100} [MPa]
204.83	761.25	7975.26	128.11

5. Initial yield surface

5.1 Introduction

In this section, the two-dimensional (2D) initial yield surface representations of a solid element Body-Centered Cubic lattice unit cell are determined under five different sets of load cases in *Abaqus/Standard*. The applied stresses for all load cases are oriented with the global coordinate system of the UC. The differences between the results are discussed in detail, and a plot containing all representations is shown. Additionally, the initial yield stress values for the hydrostatic tension, simple shear XY, and 45° shear XY load cases, as well as for the uniaxial tension in the principal [100], face diagonal [110], and space diagonal [111] directions are determined. The geometric linearity is assumed, and the analysis is force-controlled.

5.2 Implementation

Since not all materials have a sharply pronounced yield point in a stress-strain diagram, usually an offset yield stress at 0.2% or 1% plastic strain is taken ($R_{\mathrm{p0.2}}$ or R_{p1}). These values are typically obtained from the uniaxial load cases, where only one stress component is different than zero. In this work, due to the variety of studied load cases and cubic material symmetry of the UC, which can lead to the presence of complex stress states, the onset of yielding is taken as the point where the ratio of plastically dissipated energy (ALLPD) and internal energy (ALLIE) reaches the value of 1%. The internal energy is a sum of plastically dissipated energy, recoverable elastic strain energy (ALLSE), and artificial strain energy (ALLAE). The analysis is force-controlled, and the applied stresses (according to Eq.(2.4)) at the increment when the condition for the onset of yielding is fulfilled are taken as the yield onset for that specific load case. Five different sets of load cases are considered, and the corresponding applied stresses are oriented with the global coordinate system of the UC.

The applied macroscopic boundary conditions for the hydrostatic tension, simple shear XY, 45° shear XY, and uniaxial tension in the [100], [110], and [111] directions are shown in *Tab. 5.1*. To obtain the initial yield stress values for the uniaxial tension in the [110] and [111] directions, the same stress tensor rotations described in subsection 4.3.2 and subsection 4.3.3, must be performed here as well. The "equation" MPCs are implemented for both these load cases, as discussed in their respective sections.

Tab. 5.1 The macroscopic BCs for the hydrostatic tension, simple shear XY, 45° shear XY, and uniaxial tension in the [100], [110], and [111] directions. The master node notation is based on *Fig. 2.3*. The "equation" MPCs are applied for the uniaxial tension in the [110], and [111] directions.

Load case	Master nodes	u_x	u_y	u_z	F_x	F_y	F_z
Hydrostatic tension	SWB	0	0	0	-	-	-
	SEB	-	0	0	F	-	-
	NWB	0	-	0	-	F	-
	SWT	0	0	-	-	-	F
Simple shear XY	SWB	0	0	0	-	-	-
	SEB	0	-	0	-	F	-
	NWB	0	0	0	-	-	-
	SWT	0	0	0	-	-	-
45° shear XY	SWB	0	0	0	-	-	-
	SEB	-	0	0	F	-	-
	NWB	0	-	0	-	$-$F	-
	SWT	0	0	0	-	-	-
Uniaxial tension [100]	SWB	0	0	0	-	-	-
	SEB	-	0	0	F	-	-
	NWB	0	-	0	-	free	-
	SWT	0	0	-	-	-	free
Uniaxial tension [110]	SWB	0	0	0	-	-	-
	SEB	-	$= u_{x\|\mathrm{NWB}}$	0	F	-	-
	NWB	-	-	0	F	F	-
	SWT	0	0	-	-	-	free
Uniaxial tension [111]	SWB	0	0	0	-	-	-
	SEB	-	$= u_{x\|\mathrm{NWB}}$	$= u_{x\|\mathrm{SWT}}$	F	-	-
	NWB	-	-	$= u_{y\|\mathrm{SWT}}$	F	F	-
	SWT	-	-	-	F	F	F

For the first initial yield surface representation (model I), a plane stress state is assumed, where the out-of-plane normal stress ($\sigma_{zz} = 0$) and in-plane shear stress ($\sigma_{xy} = 0$) are zero, while the in-plane normal ones (σ_{xx} and σ_{yy}) are varied. The load cases are applied in a way that the ratio of σ_{yy} and σ_{xx} is constant and equal to the parameter k (i.e., $\frac{\sigma_{yy}}{\sigma_{xx}} = k$). In total 21 points are determined between $\sigma_{xx} = \sigma_{yy}$ and $\sigma_{xx} = -\sigma_{yy}$ points. The rest of the surface can be mirrored from here since it is symmetric due to the cubic material symmetry, and restriction to the plane stress states. The parameter k takes values from 1 to -1, with increments of 0.1 to cover all required load cases. The exact macroscopic BCs that are applied are shown in *Tab. 5.2*.

For the second set of load cases (model II), the out-of-plane normal stress is constant and equal to one-fourth of the yield stress obtained from the uniaxial tension load case in the principal material direction ($\sigma_{zz} = 0.25 \cdot \sigma_{\mathrm{Y100}} = 0.11125$ MPa), while the in-plane ones (σ_{xx} and σ_{yy}) are varied under the assumption that their ratios are constant (i.e., $\frac{\sigma_{yy}}{\sigma_{xx}} = k$ and $\frac{\sigma_{xx}}{\sigma_{yy}} = m$). The load cases have to be implemented in two steps, where the first step ensures that the σ_{zz} is at the required level for the application of the in-plane stresses, i.e. that it will remain at this value throughout the second step. Since the plane-stress condition is not fulfilled anymore, the complete symmetry of the yield surface is not ensured, and 41 points between $\sigma_{xx} = \sigma_{yy}$ and $-\sigma_{xx} = -\sigma_{yy}$ points are determined, and afterward mirrored to obtain the complete surface. To cover all required load cases, two different parameters k and m are defined and varied. For the points from 1 to 21, only the parameter k is considered, and it takes values from 1 to -1, with increments of 0.1. For the load cases for points from 21 to 41, only the parameter m is considered, and it takes the values from -1 to 1, with increments of 0.1. The exact macroscopic BCs that are applied are shown in *Tab. 5.2*.

For the third set of load cases (model III), the out-of-plane normal stress is constant and equal to one-half of the yield stress obtained from the uniaxial tension load case in the principal material direction ($\sigma_{zz} = 0.5 \cdot \sigma_{\mathrm{Y100}} = 0.2225$ MPa), while the in-plane ones (σ_{xx} and σ_{yy}) are varied under the assumption that their ratios are constant (i.e., $\frac{\sigma_{yy}}{\sigma_{xx}} = k$ and $\frac{\sigma_{xx}}{\sigma_{yy}} = m$). The rest is the same as for the model II. The exact macroscopic BCs that are applied are shown in *Tab. 5.2*.

The fourth set of load cases (model IV) considers the out-of-plane normal stress to be zero ($\sigma_{zz} = 0$), and the in-plane shear stress to be constant and equal to one-half of the yield stress from the uniaxial tension load case in the principal material direction ($\sigma_{xy} = 0.5 \cdot \sigma_{\mathrm{Y100}} = 0.2225$ MPa). The in-plane normal stresses (σ_{xx} and σ_{yy}) are varied under the assumption that their ratios are constant (i.e., $\frac{\sigma_{yy}}{\sigma_{xx}} = k$ and $\frac{\sigma_{xx}}{\sigma_{yy}} = m$). The load cases have to be implemented in two steps, where the first step ensures that the σ_{xy} is at the required level for the application of the σ_{xx} and σ_{yy}, i.e. that it will remain at this value throughout the second step. Due to the presence of the shear stress component, the complete symmetry of the yield surface is not ensured, and 41 points between $\sigma_{xx} = \sigma_{yy}$ and $-\sigma_{xx} = -\sigma_{yy}$ points are determined, and afterward mirrored to obtain the complete surface. To cover all required load cases, two different parameters k and m are defined and varied in the same way as for model II. The exact macroscopic BCs that are applied are shown in *Tab. 5.2*.

The fifth set of load cases (model V) considers the out-of-plane normal stress to be zero ($\sigma_{zz} = 0$), and the in-plane shear stress to be constant and equal to one-half of the yield stress from the simple shear XY load case ($\sigma_{xy} = 0.5 \cdot \sigma_{\mathrm{Yxy}} = 2.4675$ MPa). The in-plane normal stresses (σ_{xx} and σ_{yy}) are varied under the assumption that their ratios are constant (i.e., $\frac{\sigma_{yy}}{\sigma_{xx}} = k$ and $\frac{\sigma_{xx}}{\sigma_{yy}} = m$). The rest is the same as for the model IV. The exact macroscopic BCs that are applied are shown in *Tab. 5.2*.

Tab. 5.2 The macroscopic BCs that are applied to determine the yield surface representations from models I to V. The master node notation is based on *Fig. 2.3.* For points 1 - 21, only the parameter k is considered, and it takes values from 1 to -1, with increments of 0.1. For points 21 - 41, corresponding to the BCs in parentheses, only the parameter m is considered and it takes the values from -1 to 1, with increments of 0.1.

Model	Step	Load case	Master nodes	u_x	u_y	u_z	F_x	F_y	F_z
I	Step 1.	$\frac{\sigma_{yy}}{\sigma_{xx}} = k$ $\sigma_{zz} = 0$ $\sigma_{xy} = 0$	SWB	0	0	0	-	-	-
			SEB	-	0	0	F	-	-
			NWB	0	-	0	-	k·F	-
			SWT	0	0	-	-	-	free
II	Step 1.	$\sigma_{zz} = 0.25 \cdot \sigma_{\mathrm{Y100}}$	SWB	0	0	0	-	-	-
			SEB	-	0	0	free	-	-
			NWB	0	-	0	-	free	-
			SWT	0	0	-	-	-	$\mathrm{F}_{\mathrm{Y}/4}$
	Step 2.	$\sigma_{zz} = 0.25 \cdot \sigma_{\mathrm{Y100}}$ $\sigma_{xy} = 0$ $\frac{\sigma_{yy}}{\sigma_{xx}} = k \mid (\frac{\sigma_{xx}}{\sigma_{yy}} = m)$	SWB	0	0	0	-	-	-
			SEB	-	0	0	F $\mid$ (m·F)	-	-
			NWB	0	-	0	-	k·F $\mid$ (−F)	-
			SWT	0	0	-	-	-	$\mathrm{F}_{\mathrm{Y}/4}$
III	Step 1.	$\sigma_{zz} = 0.5 \cdot \sigma_{\mathrm{Y100}}$	SWB	0	0	0	-	-	-
			SEB	-	0	0	free	-	-
			NWB	0	-	0	-	free	-
			SWT	0	0	-	-	-	$\mathrm{F}_{\mathrm{Y}/2}$
	Step 2.	$\sigma_{zz} = 0.5 \cdot \sigma_{\mathrm{Y100}}$ $\sigma_{xy} = 0$ $\frac{\sigma_{yy}}{\sigma_{xx}} = k \mid (\frac{\sigma_{xx}}{\sigma_{yy}} = m)$	SWB	0	0	0	-	-	-
			SEB	-	0	0	F $\mid$ (m·F)	-	-
			NWB	0	-	0	-	k·F $\mid$ (−F)	-
			SWT	0	0	-	-	-	$\mathrm{F}_{\mathrm{Y}/2}$
IV	Step 1.	$\sigma_{xy} = 0.5 \cdot \sigma_{\mathrm{Y100}}$	SWB	0	0	0	-	-	-
			SEB	-	-	0	free	$\mathrm{F}_{\mathrm{Y}/2}$	-
			NWB	0	-	0	-	free	-
			SWT	0	0	-	-	-	free
	Step 2.	$\sigma_{xy} = 0.5 \cdot \sigma_{\mathrm{Y100}}$ $\sigma_{zz} = 0$ $\frac{\sigma_{yy}}{\sigma_{xx}} = k \mid (\frac{\sigma_{xx}}{\sigma_{yy}} = m)$	SWB	0	0	0	-	-	-
			SEB	-	-	0	F $\mid$ (m·F)	$\mathrm{F}_{\mathrm{Y}/2}$	-
			NWB	0	-	0	-	k·F $\mid$ (−F)	-
			SWT	0	0	-	-	-	free
V	Step 1.	$\sigma_{xy} = 0.5 \cdot \sigma_{\mathrm{Y}xy}$	SWB	0	0	0	-	-	-
			SEB	-	-	0	free	$\mathrm{F}_{\mathrm{Yxy}/2}$	-
			NWB	0	-	0	-	free	-
			SWT	0	0	-	-	-	free
	Step 2.	$\sigma_{xy} = 0.5 \cdot \sigma_{\mathrm{Y}xy}$ $\sigma_{zz} = 0$ $\frac{\sigma_{yy}}{\sigma_{xx}} = k \mid (\frac{\sigma_{xx}}{\sigma_{yy}} = m)$	SWB	0	0	0	-	-	-
			SEB	-	-	0	F $\mid$ (m·F)	$\mathrm{F}_{\mathrm{Yxy}/2}$	-
			NWB	0	-	0	-	k·F $\mid$ (−F)	-
			SWT	0	0	-	-	-	free

5.3 Results

The obtained initial yield surface representations of the BCC lattice UC for the defined sets of load cases (models I, II, III, IV, and V) are shown and discussed in this section. The initial yield stress values that are obtained for the hydrostatic tension, simple shear XY, 45° shear XY, and uniaxial tension in the [100], [110], and [111] directions are shown in *Tab. 5.3*. The load cases under which the struts are predominantly under tension or compression (e.g., hydrostatic tension or simple shear XY) have higher initial yield stress values. The ones where the bending of the struts is the dominant deformation mechanism (e.g., uniaxial tension in the principal material direction or 45° shear XY) have lower initial yield stress values, as the struts deform more easily. The bending deformation of the struts is the highest under the 45° shear load case, and the corresponding $\sigma_{\mathrm{Y45^\circ}}$ value is the lowest of the six load cases studied here. The plastic anisotropy can be observed, as there are strong differences in the obtained initial yield stress values between the uniaxial tension load cases in three different directions. Also, there are strong differences between the values from simple shear and 45° shear load cases, which would be the same for an isotropic material under the assumption of geometric linearity. Additionally, in that case, hydrostatic tension load would not lead to plasticity, according to the J_2 yield criterion, as there would be no change in shape, only in volume.

The representation of the yield surface determined from the plane stress load cases (model I), where the out-of-plane normal stress ($\sigma_{zz} = 0$) and in-plane shear stress ($\sigma_{xy} = 0$) are zero, while the in-plane normal ones (σ_{xx} and σ_{yy}) are varied, is shown in *Fig. 5.1*.

From the results, it can be seen that the surface is oval-shaped. There is a slight difference in the initial yield stress values between the biaxial tension ($\sigma_{\mathrm{Y}} = 0.468$ for $\sigma_{xx} = \sigma_{yy}$) and uniaxial tension in the principal material direction load cases ($\sigma_{\mathrm{Y}} = 0.445$). Suppose the orientation of the global coordinate system of the UC were to be changed, relative to which the stresses are applied. In that case, the initial yield surface representation might be different in size or shape, and these differences between the values might become more pronounced. In all load cases for model I, the main deformation mechanism is the bending

Tab. 5.3 The initial yield stress values for the hydrostatic tension (σ_{Yhyd}), simple shear XY ($\sigma_{\mathrm{Y}xy}$), 45° shear XY ($\sigma_{\mathrm{Y45^\circ}}$), and uniaxial tension in the [100] (σ_{Y100}), [110] (σ_{Y110}), and [111] (σ_{Y111}) directions.

σ_{Yhyd} [MPa]	$\sigma_{\mathrm{Y}xy}$ [MPa]	$\sigma_{\mathrm{Y45^\circ}}$ [MPa]	σ_{Y100} [MPa]	σ_{Y110} [MPa]	σ_{Y111} [MPa]
3.933	1.744	0.259	0.445	0.925	4.935

of the struts. As previously mentioned, the highest amount of bending is present for the 45° shear XY load case ($\sigma_{xx} = -\sigma_{yy}$), resulting in the lowest values of initial yield stress.

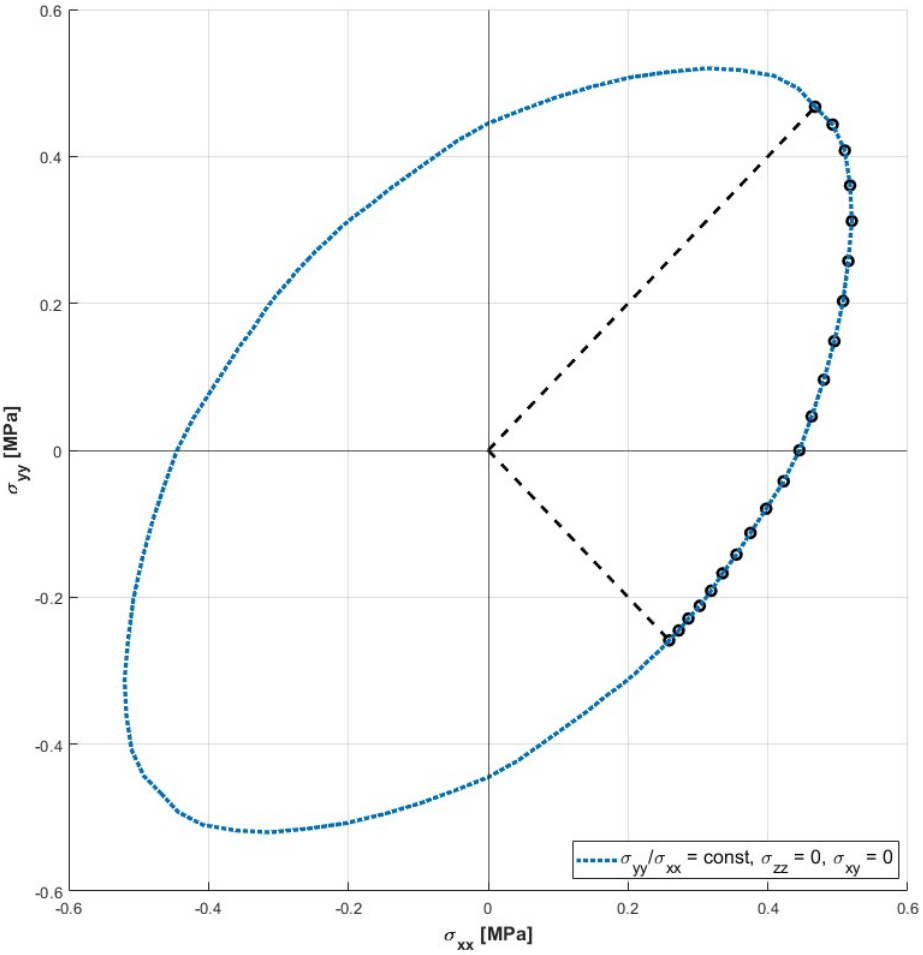

Fig. 5.1 The representation of the yield surface determined from the plane stress load cases (model I), where the out-of-plane normal stress and in-plane shear stress are zero, while the in-plane normal ones are varied. The black circles represent the 21 points that are determined.

The representations of the yield surface determined from the second and third sets of load cases (models II and III), which consider a constant out-of-plane normal stress ($\sigma_{zz} = 0.25 \cdot \sigma_{Y100}$ and $\sigma_{zz} = 0.5 \cdot \sigma_{Y100}$), while the in-plane normal stresses are varied, are shown in *Fig. 5.2*.

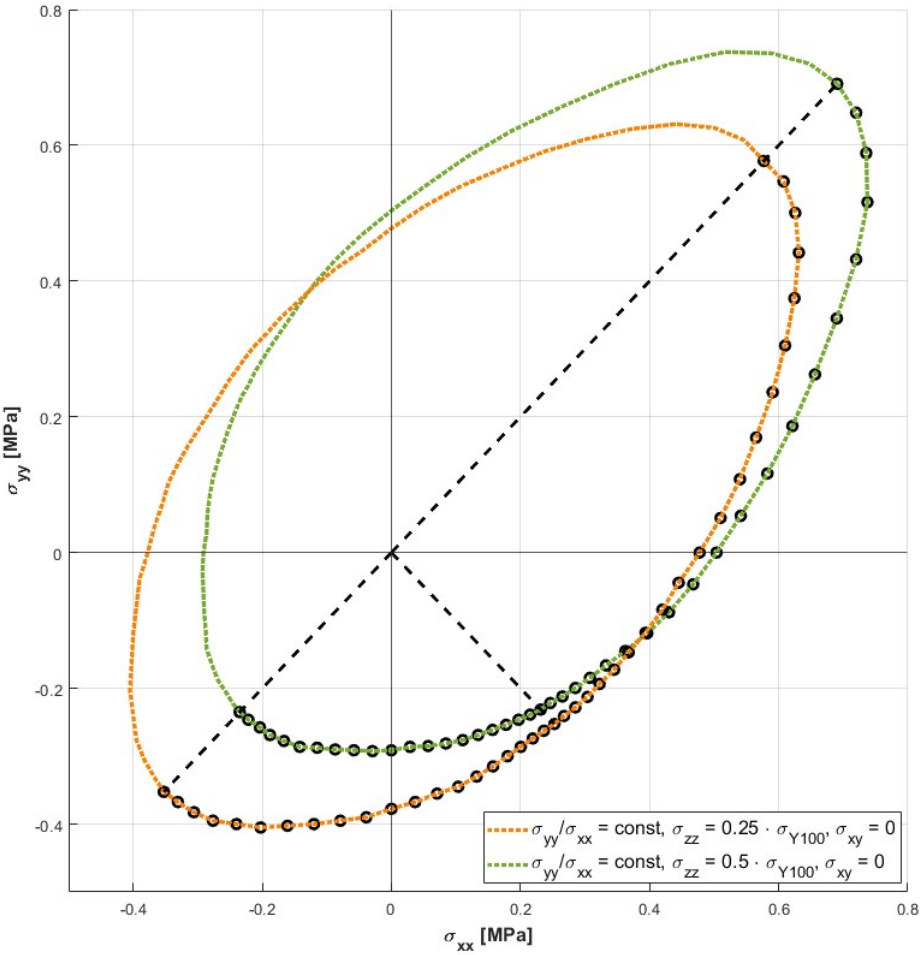

Fig. 5.2 The representations of the yield surface determined from the second and third sets of load cases (models II and III). The black circles represent the 41 points that are determined. The values for the out-of-plane normal stresses are $\sigma_{zz} = 0.25 \cdot \sigma_{Y100} = 0.11125$ MPa and $\sigma_{zz} = 0.5 \cdot \sigma_{Y100} = 0.2225$ MPa respectively.

The results show that the yield surface representations are again oval-shaped, but are more asymmetrical than the previous one (*Fig. 5.1*). This is understandable, as the out-of-plane normal stress is positive for both models II and III, and thus the shape is shifted more in the direction of the first quadrant. Since the value of σ_{zz} is larger for model III, it is shifted further than the representation for model II. The load cases where $\sigma_{xx} = \sigma_{yy}$ have respectively the highest yield stresses, which are also higher compared to the same load case from model I. This is explained by the fact that the positive out-of-plane normal stress brings this load case closer to the hydrostatic tension one (i.e., $\sigma_{xx} = \sigma_{yy} = \sigma_{zz}$), under which the struts experience only pure tension. In the regions where the compressive stresses begin to dominate the load cases, the positive σ_{zz} leads to the overall lower yield stress values compared to the yield surface representation from model I.

The representations of the yield surface determined from the fourth and fifth set of load cases (models IV and V), which consider that the in-plane shear stress component is constant ($\sigma_{xy} = 0.5 \cdot \sigma_{\mathrm{Y}100}$ and $\sigma_{xy} = 0.5 \cdot \sigma_{\mathrm{Y}xy}$), the out-of-plane normal stress to be zero, while the in-plane normal stresses are varied, are shown in *Fig. 5.3*.

The results show that the surfaces are similarly shaped as the plane stress representation from model I (*Fig. 5.1*), even though the applied load cases are different. Similarly, the yield stress values obtained from the $\sigma_{xx} = \sigma_{yy}$ and "uniaxial tension" ($\sigma_{xx} \neq 0$, $\sigma_{yy} = 0$) load cases are different (i.e., $\sigma_{\mathrm{Y}} = 0.463$ MPa for $\sigma_{xx} = \sigma_{yy}$, and $\sigma_{\mathrm{Y}} = 0.436$ for the "uniaxial tension" load case obtained from model IV). In comparison to the representations from models II and III (*Fig. 5.2*), these representations again have a higher order of symmetry. Overall, the presence of the constant shear stress component reduces the yield stress values under all stress states, "pulling" the surface inward, when compared to the results from the model I (*Fig. 5.1*). The larger the value of σ_{xy}, the more pronounced the contraction of the surface (i.e., the surface representation from model V is smaller than the one from model IV).

The plot containing all representations (models I, II, III, IV, and V) together is shown in *Fig. 5.4*. The previously discussed differences between the results of the yield surface representations can be better observed in this plot.

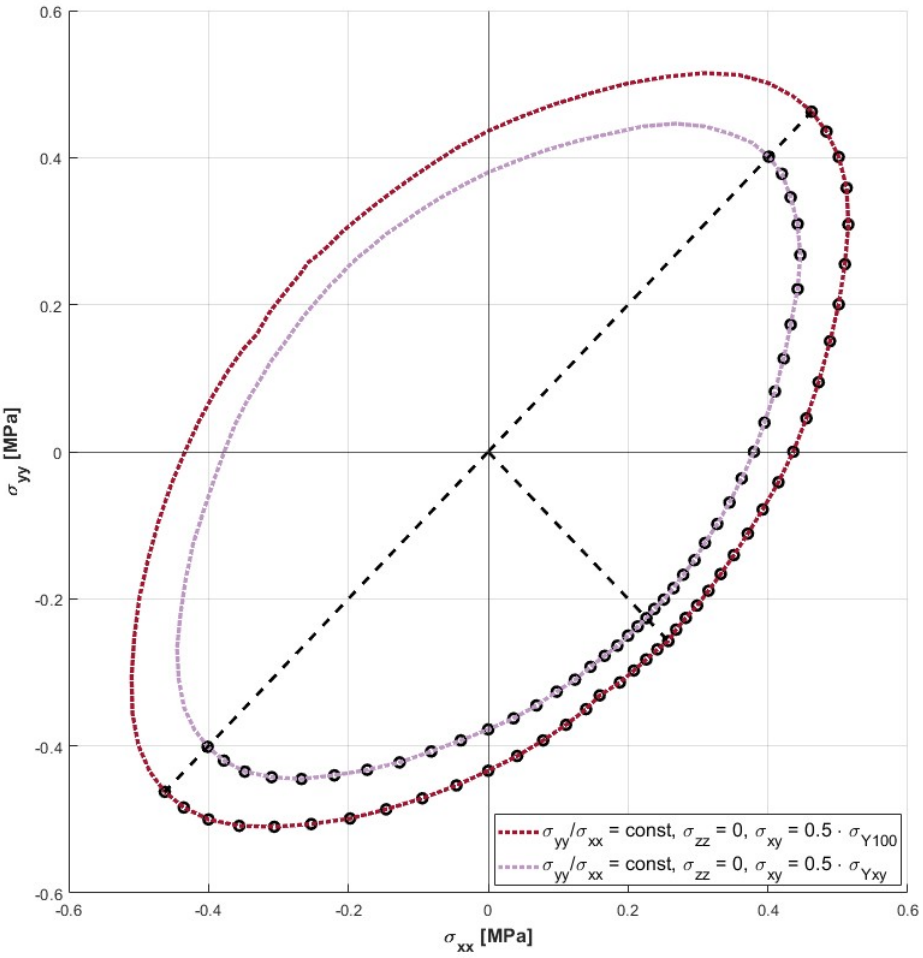

Fig. 5.3 The representations of the yield surface determined from the fourth and fifth sets of load cases (models IV and V). The black circles represent the 41 points that are determined. The values for the in-plane shear stresses are $\sigma_{xy} = 0.5 \cdot \sigma_{\mathrm{Y100}} = 0.2225$ MPa and $\sigma_{xy} = 0.5 \cdot \sigma_{\mathrm{Yxy}} = 2.4675$ MPa respectively.

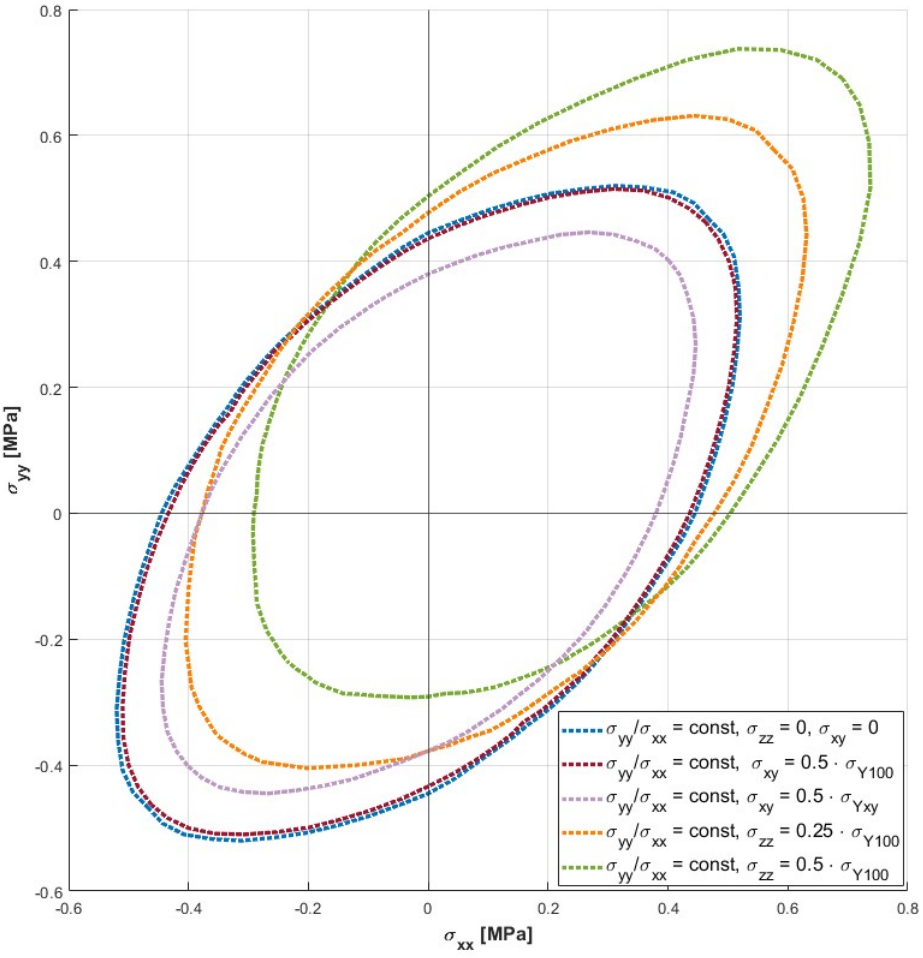

Fig. 5.4 The representations of the yield surface from all five load case sets (models I, II, III, IV, and V). The stresses are oriented with the global coordinate system of the UC. The values for the out-of-plane normal stresses are $\sigma_{zz} = 0.25 \cdot \sigma_{\mathrm{Y100}} = 0.11125$ MPa and $\sigma_{zz} = 0.5 \cdot \sigma_{\mathrm{Y100}} = 0.2225$ MPa respectively. The values for the in-plane shear stresses are $\sigma_{xy} = 0.5 \cdot \sigma_{\mathrm{Y100}} = 0.2225$ MPa and $\sigma_{xy} = 0.5 \cdot \sigma_{\mathrm{Yxy}} = 2.4675$ MPa respectively.

6. Elastoplastic behavior

6.1 Introduction

In this section, the elastoplastic behavior of the BCC lattice UC is studied. Here, the results from both beam and continuum element UC models are compared side-by-side and the differences in the resulting behavior are discussed. The UCs are loaded by single load cases and combined load cases. The hydrostatic tension, simple shear XY, 45° shear XY, and uniaxial tension in the [100] direction are modeled as the single load cases. The combined approach consists of two load cases that are either applied simultaneously (single step) or in succession (two different steps). The combinations that are implemented in this work are combined simple shear XY and XZ, simple shear XY and hydrostatic, simple shear XY and 45° shear XY, as well as 45° shear XY and hydrostatic load cases.

The plastic behavior of the bulk material in this work is defined in chapter 3.

The analysis is strain-controlled, and done under the assumption of geometric linearity. An engineering strain of 3.75% is applied for the single load cases and combined load cases in a single step. For each load case in the combined approach with two different steps, an engineering strain of 2% is applied. The BCs that are implemented for the single load cases are already defined in *Tab. 4.1*. The ones for the combined load cases are defined in the further sections.

For the solid model, the number of 250 equal increments is chosen, because it captures the behavior of the model more accurately compared to the 100 increments, while still retaining a good computational effort (compared to the 500 increments). For the beam model, 500 equal increments are used, because the accuracy of results is better, and the computational effort is still low.

6.2 Influence of the number of section points on the beam model results

The beam model is modeled with two different numbers of section points - 17 and 1441. In *Figs. 6.1 to 6.4* a comparison between the obtained engineering stress-strain curves for both beam element modeling approaches from all single load cases (hydrostatic tension, 45° shear XY, uniaxial tension [100], and simple shear XY) are shown. In all figures the relevant effective normal and shear stress components are shown, the remaining ones are zero.

For the single hydrostatic tension load case, shown in *Fig. 6.1*, the results from both beam modeling approaches perfectly match each other. Here, the struts are under pure tension, and the corresponding normal stress distribution over the cross-section of the beam is uniform. Because of this, the yield stress is reached simultaneously in all regions of the struts, and due to the bilinear plasticity of the bulk material, there is a sharp transition into the linear elastoplastic region. The model with the default number of section points also leads to accurate results due to this uniformity of the stress distribution throughout the load case.

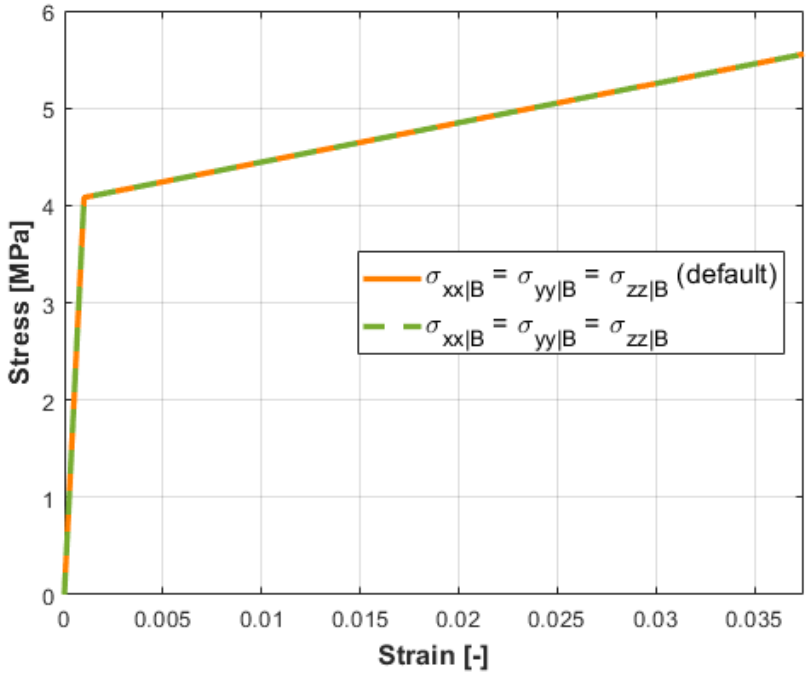

Fig. 6.1 Comparison of the engineering stress-strain curves for the single hydrostatic tension load case for the beam models with default (17) and increased (1441) number of section points.

For the single 45° shear XY load case, shown in *Fig. 6.2*, the results from both beam modeling approaches show notable differences. Here, the struts experience significant bending deformation, and the model with the increased number of section points is required to accurately capture the corresponding nonlinear stress distribution. Since the highest stresses are present in the outermost fibers of the beam, they are the first to yield. With increasing strain, the plastic zones grow towards the neutral axis, while the central elastic zones are reduced, and the stress distribution becomes increasingly more nonlinear. The isotropic hardening additionally enhances this nonlinear behavior. Due to the very high bending deformation of the struts for this load case, the plastic zones have presumably evolved closer to the neutral axis. The increased number of section points can accurately capture these higher stresses, as well as the overall nonlinear stress distribution, leading to the higher linear hardening region and smoother curve in the nonlinear elastoplastic region compared to the default beam element model.

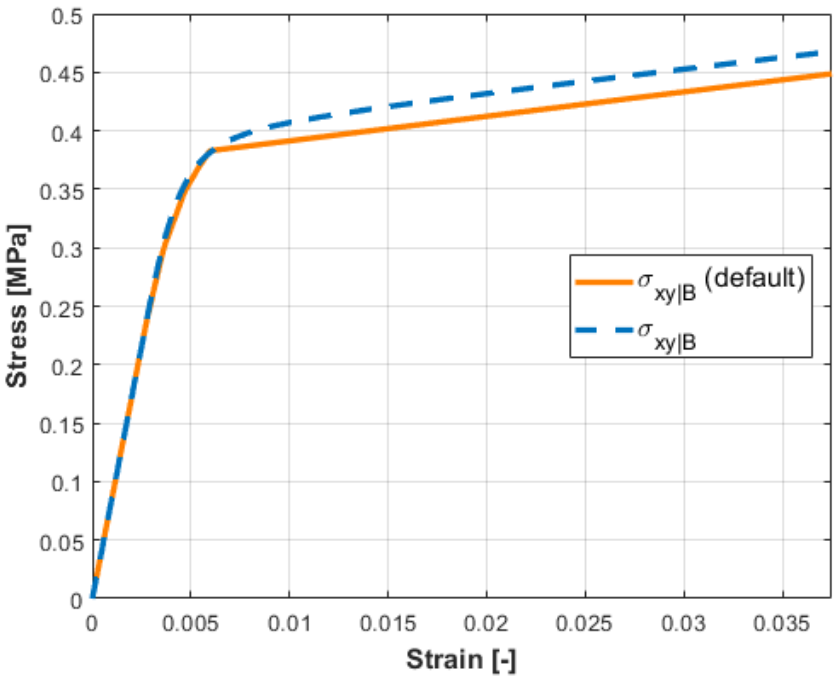

Fig. 6.2 Comparison of the engineering stress-strain curves for the single 45° shear XY load case for the beam models with default (17) and increased (1441) number of section points.

For the single uniaxial tension load case in the principal material direction [100], shown in *Fig. 6.3*, the differences between the results are present but considerably less pronounced compared to the 45° shear XY one. This is due to the lower bending deformation of the struts that is present here, which leads to less nonlinear stress distribution. This can be relatively accurately captured by the default modeling approach. Still, the model with the increased number of section points is the preferred choice.

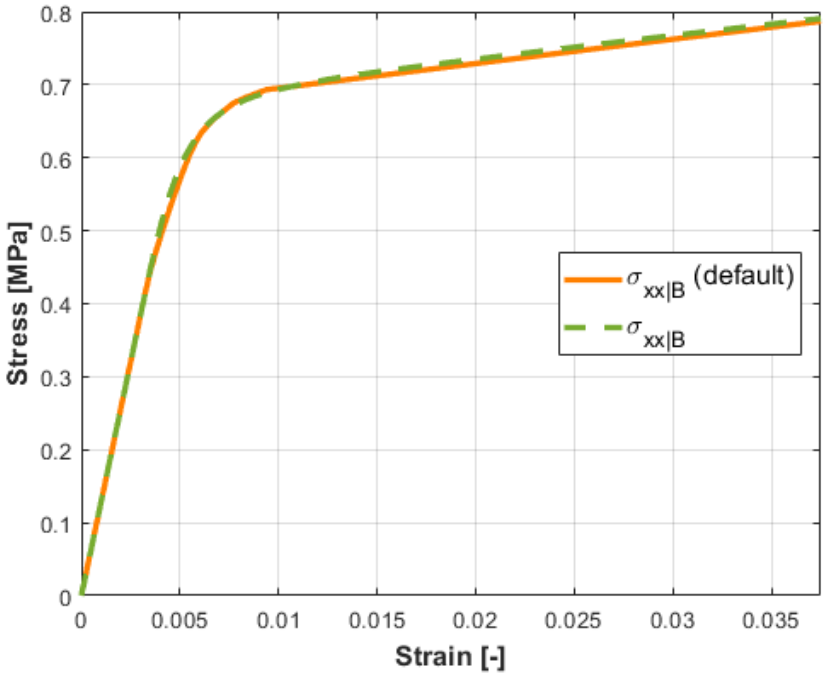

Fig. 6.3 Comparison of the engineering stress-strain curves for the single uniaxial tension [100] load case for the beam models with default (17) and increased (1441) number of section points.

For the single simple shear XY load case, shown in *Fig. 6.4*, the dominant deformation mechanisms of the struts are compression and tension. Because of this, the results from both beam modeling approaches perfectly match each other. The explanation is the same as for the single hydrostatic tension load case. Due to the very small bending deformation that is present, there is a subtle nonlinear elastoplastic region, which is accurately captured by both modeling approaches.

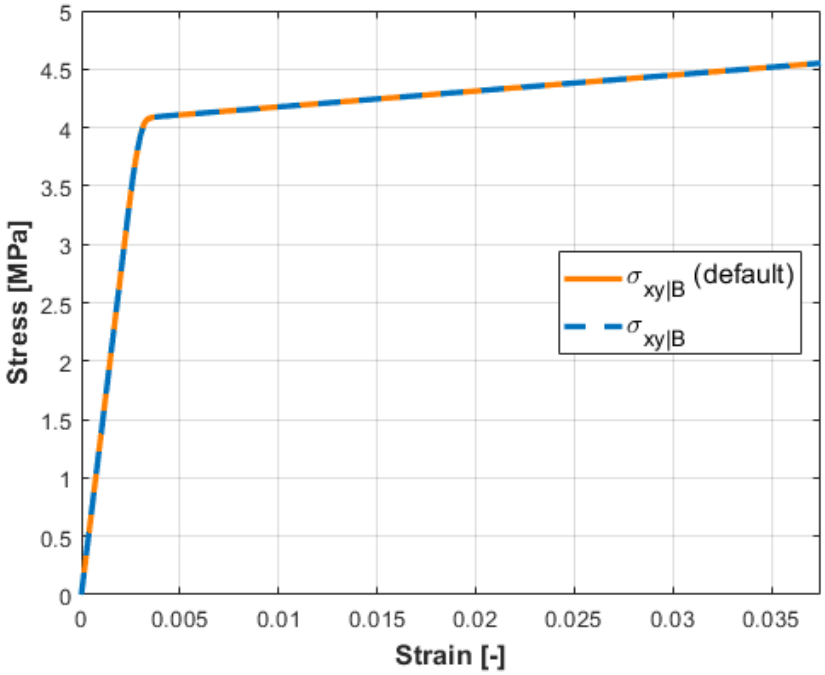

Fig. 6.4 Comparison of the engineering stress-strain curves for the single simple shear XY load case for the beam models with default (17) and increased (1441) number of section points.

In conclusion, the increase in the number of section points leads to the ability to better capture the nonlinear behavior due to bending in the elastoplastic engineering stress-strain curve. For the load cases where the tension or compression of the struts are the main deformation mechanisms, the results from both beam modeling approaches perfectly match. In the following sections, all results for the beam element UC model that are shown, are obtained from the models with the increased number of section points.

6.3 Single load cases

In this section, the results from the models where only single load cases (hydrostatic tension, simple shear XY, 45° shear XY, and uniaxial tension [100]) are applied, are discussed. The BCs that are implemented here are the same ones used for the linear elastic models in the section 4.2 (*Tab. 4.1*). The comparison of the deformed and undeformed shapes for each of the modeling approaches under these load conditions is shown and discussed.

For the beam models, in addition to the deformed figure, the axial stress (S11) distribution at the outermost fiber (*Fig. 3.3*) is shown in the local orientation of the beams. The global deformation behavior of the struts can be assessed from these results.

For the solid element models, in addition to the deformed figure, the accumulated equivalent plastic strain (PEEQ) distribution is shown. The PEEQ is a scalar variable that characterizes the plastic state (i.e. it is a measure of the plastic dissipated energy). If its value is larger than zero, it means that the plastic yielding has occurred, and the value grows as the plastic deformation "accumulates". The PEEQ value can either grow or remain at the same level (if no further plastic deformation occurs), but it can never decrease or be negative (it is related to von Mises stress which is always positive) [1, 15]. The lower limit of the PEEQ in contour plots in this work is set to the very small value of 1e-6 so that only the regions that have yielded are shown. For some load cases, the upper limit is restricted as well, to exclude the local PEEQ concentrations, and better show the plastic behavior of the struts.

The slopes of the engineering stress-strain curves from the UC models are determined at certain points for each of the load cases. The ones obtained in the linear elastic regions (i.e. $\tilde{K}$, $\tilde{M}$, $\tilde{G}$, and $\tilde{E}$) are compared to the results obtained from the linear elastic FEA at the beginning of the report. The effective tangent moduli $\tilde{E_{\mathrm{T}}}$ are determined in the linear hardening region of these engineering stress-strain curves. Finally, the effective hardening moduli $\tilde{H}$ are computed according to Eq.(3.1).

6.3.1 Hydrostatic load case

The results that are obtained for the hydrostatic tension load case are discussed in this section. The deformed and undeformed shapes of the UC at the endpoint (engineering strain of 3.75%) of the load case for the beam model (*Fig. 6.5*) and solid element model (*Fig. 6.6*) are shown in corresponding figures.

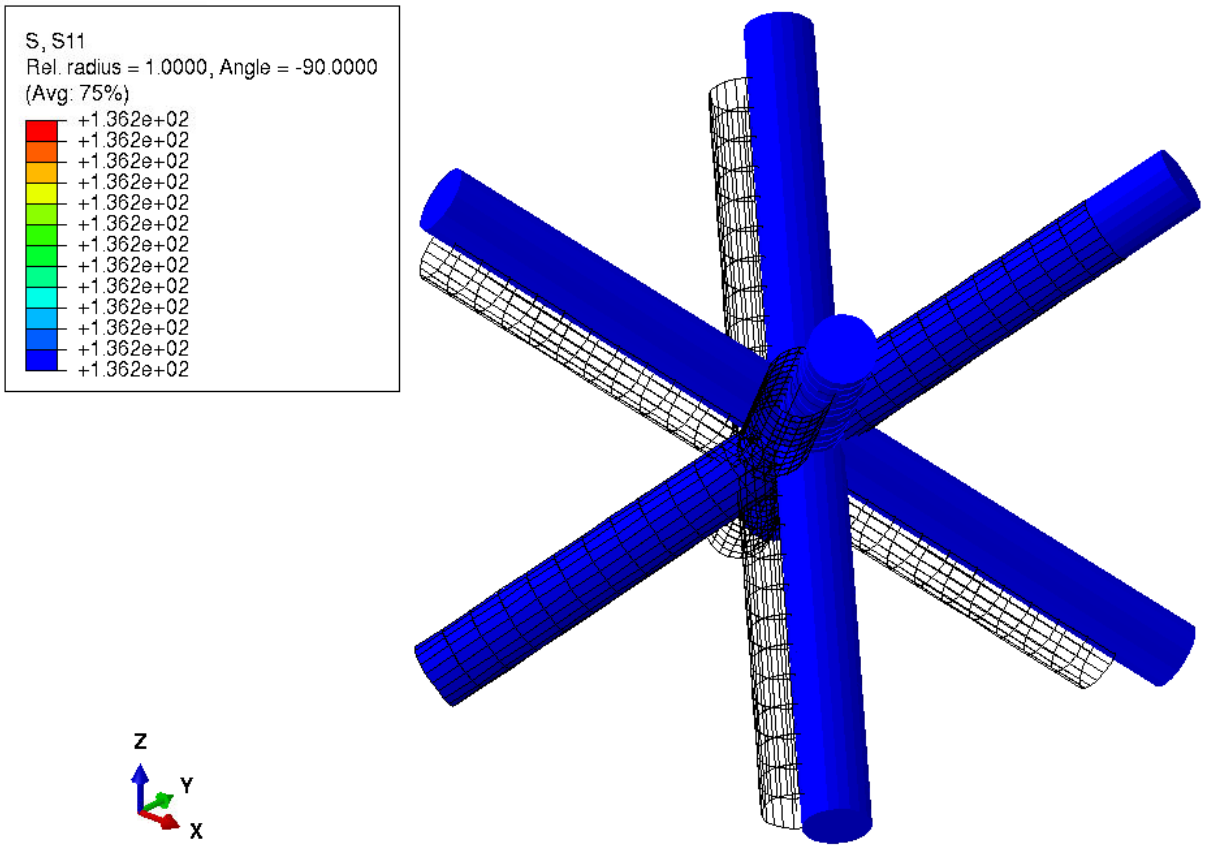

Fig. 6.5 The deformed and undeformed (wireframe) shape of the beam element model, as well as the axial stress (S11) distribution at the outermost fiber (*Fig. 3.3*) in the local orientation of beam elements at the endpoint (engineering strain of 3.75%) of the hydrostatic tension load case.

From the deformed figure of the beam element UC (*Fig. 6.5*), as well as the axial stress (S11) distribution at the outermost fiber (*Fig. 3.3*) in the local orientation of beam elements, it is concluded that the struts experience only pure tension for this load case.

The results from the solid element model show the regions of the UC that have yielded, and it is concluded that the tips of the struts experience no yielding at the endpoint (engineering strain of 3.75%) of this load case (*Fig. 6.6*). Except for the local plasticity concentrations in the vicinity of the vertices, the central regions of the struts (light and dark orange in *Fig. 6.6*) experience slightly higher plastic deformations compared to the

rest of the UC. As the UC deforms under load, the highest constriction of the struts occurs here, causing these regions to be the first to yield and have higher PEEQ values at the endpoint of the load case. The yielding of the central regions for this case occurs simultaneously since all struts experience the same deformation (pure tension).

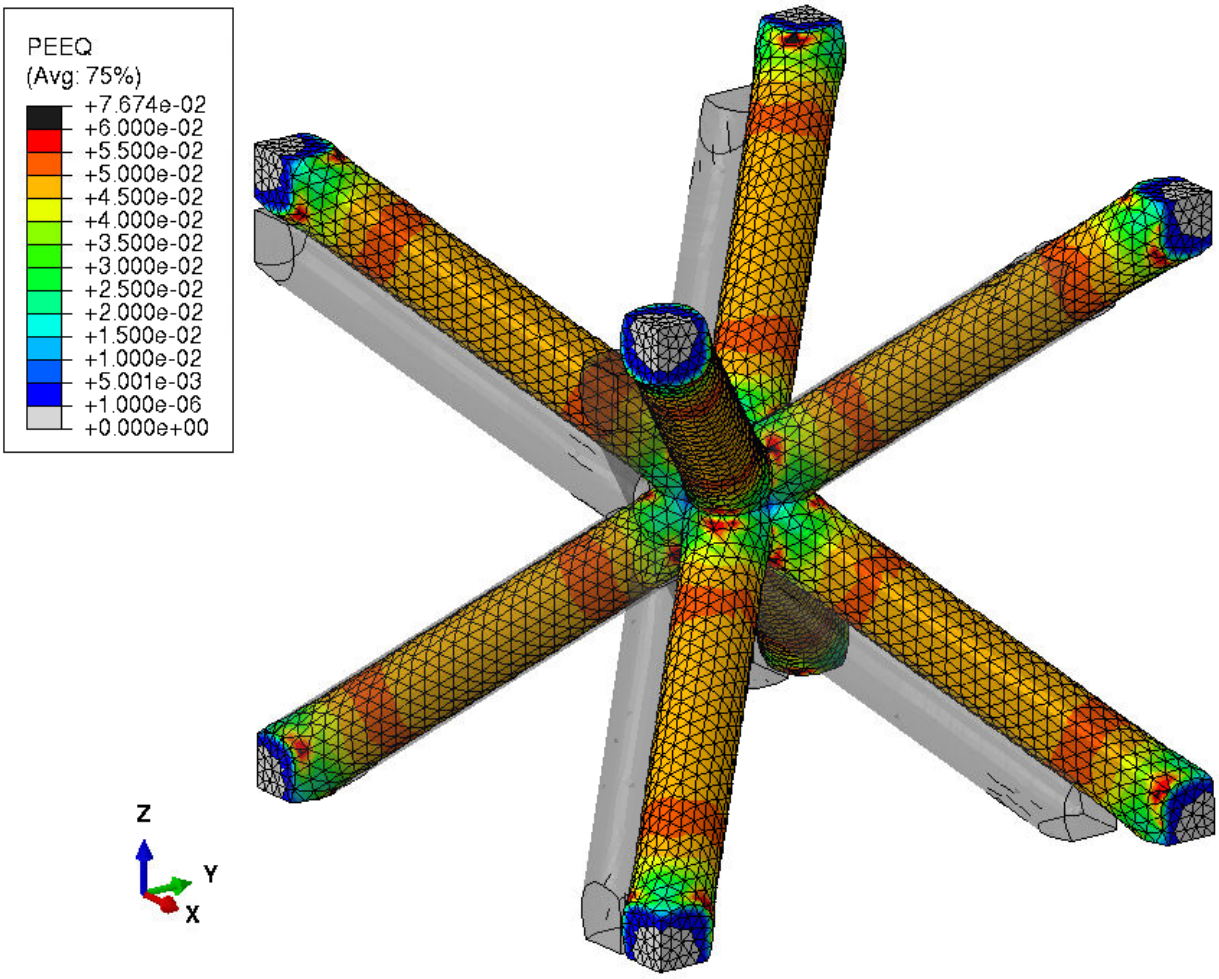

Fig. 6.6 The deformed and undeformed (shaded) shape of the solid element model, as well as the equivalent plastic strain (PEEQ) distribution at the endpoint (engineering strain of 3.75%) of the hydrostatic tension load case.

The obtained engineering stress-strain curves from both modeling approaches are presented and compared in *Fig. 6.7*. The relevant effective normal stress components are shown, the remaining effective stress components are zero. Since the struts experience only pure tension, after the value of the yield limit is reached, there is a sharp transition into the linear elastoplastic regime.

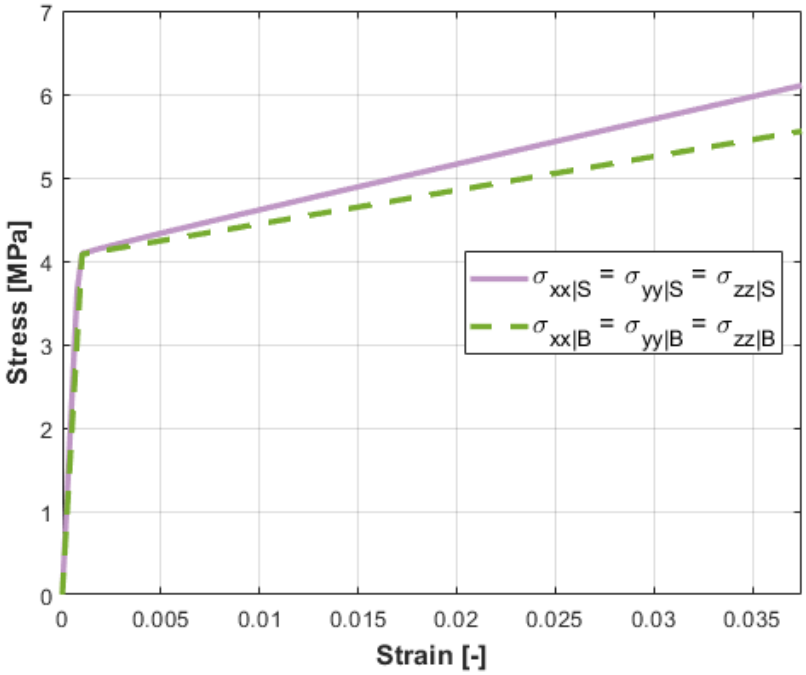

Fig. 6.7 The obtained engineering stress-strain curves for the hydrostatic tension load case for the beam model (index B) and solid element model (index S).

The slope values are shown in *Tab. 6.1.* The effective bulk moduli $\tilde{K}$ values coincide with the ones obtained from the linear elastic FEA. The effective tangent $\tilde{K}_{\mathrm{T}}$ moduli, estimated at around 2% engineering strain, and corresponding hardening $\tilde{K}_{\mathrm{H}}$ moduli values from both modeling approaches are different. It is concluded that the slopes of the engineering stress-strain curves of these modeling approaches are different in both elastic and elastoplastic regions. This is caused by the already discussed inaccuracies of the beam element modeling approach. Regarding the tangent modulus, the steeper the slope (the larger the value of the tangent modulus) in the linear elastoplastic region, the more pronounced is the hardening effect.

Tab. 6.1 The effective bulk $\tilde{K}$, tangent $\tilde{K}_{\mathrm{T}}$, and hardening $\tilde{K}_{\mathrm{H}}$ moduli obtained from the engineering stress-strain curves for the hydrostatic tension load case.

	Beam UC	Solid UC
$\tilde{K}$ [MPa] lin. el. FEA	1360.35	1625.89
$\tilde{K}$ [MPa] from the slope	1360.34	1625.47
$\tilde{K}_{\mathrm{T}}$ [MPa] at 2% engineering strain	40.41	53.93
$\tilde{K}_{\mathrm{H}}$ [MPa] at 2% engineering	41.64	55.79

6.3.2 Simple shear XY

The results that are obtained for the simple shear XY load case are discussed in this section. The deformed and undeformed shape of the UC for the beam model at the endpoint (engineering strain of 3.75%) of the load case (*Fig. 6.8*), solid element model at 2% engineering strain (*Fig. 6.9*) and at the endpoint (engineering strain of 3.75%) of the load case (*Fig. 6.10*) are shown in corresponding figures.

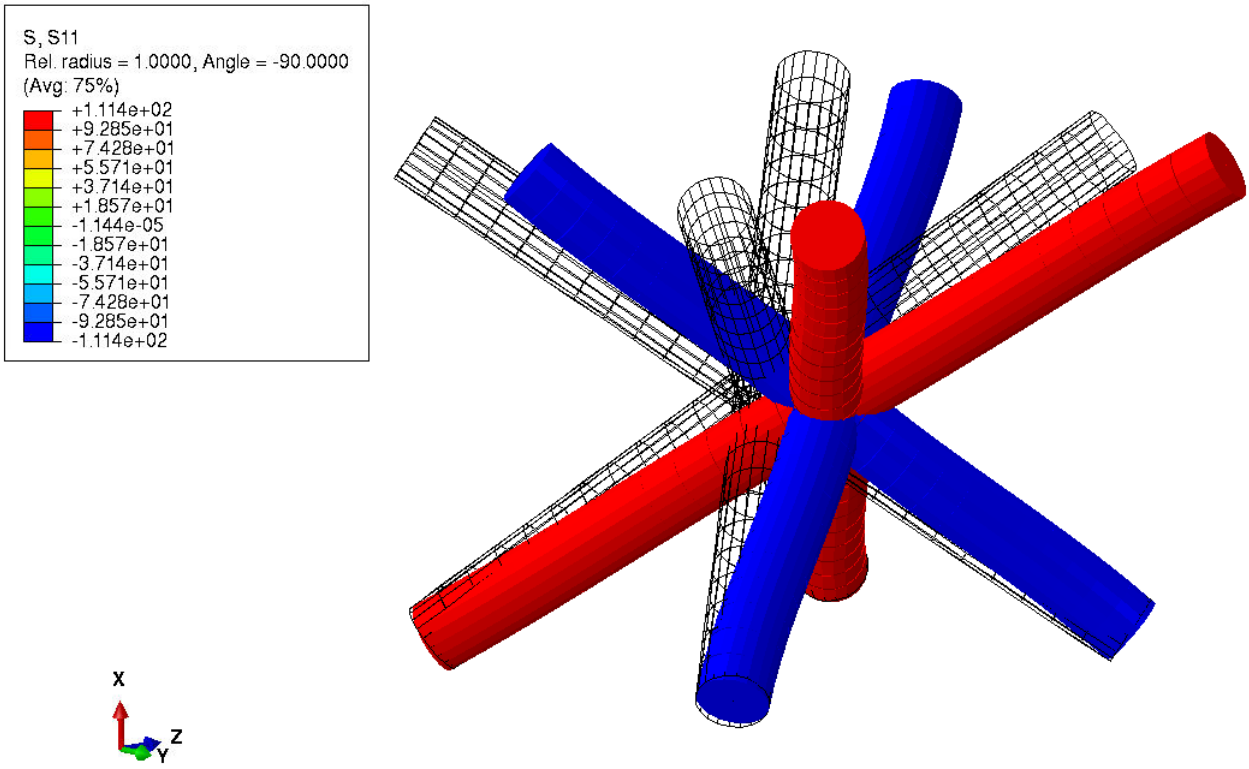

Fig. 6.8 The deformed and undeformed (wireframe) shape of the beam element model, as well as the axial stress (S11) distribution at the outermost fiber (*Fig. 3.3*) in the local orientation of beam elements at the endpoint (engineering strain of 3.75%) of the simple shear XY load case. A significantly higher deformation scale factor is applied to the deformed figure so that the very small bending deformation of struts is visible.

From the deformed figure of the beam element UC (*Fig. 6.8*), as well as the axial stress (S11) distribution at the outermost fiber (*Fig. 3.3*) in the local orientation of beam elements, the global deformation behavior of struts for this load case is assessed. A significantly higher deformation scale factor is applied to the deformed figure so that the very small bending deformation of struts is visible. Even though a small amount of bending is present, the compression and tension of the struts still dominate the overall deformation behavior (four struts are stretched, while the remaining four are compressed).

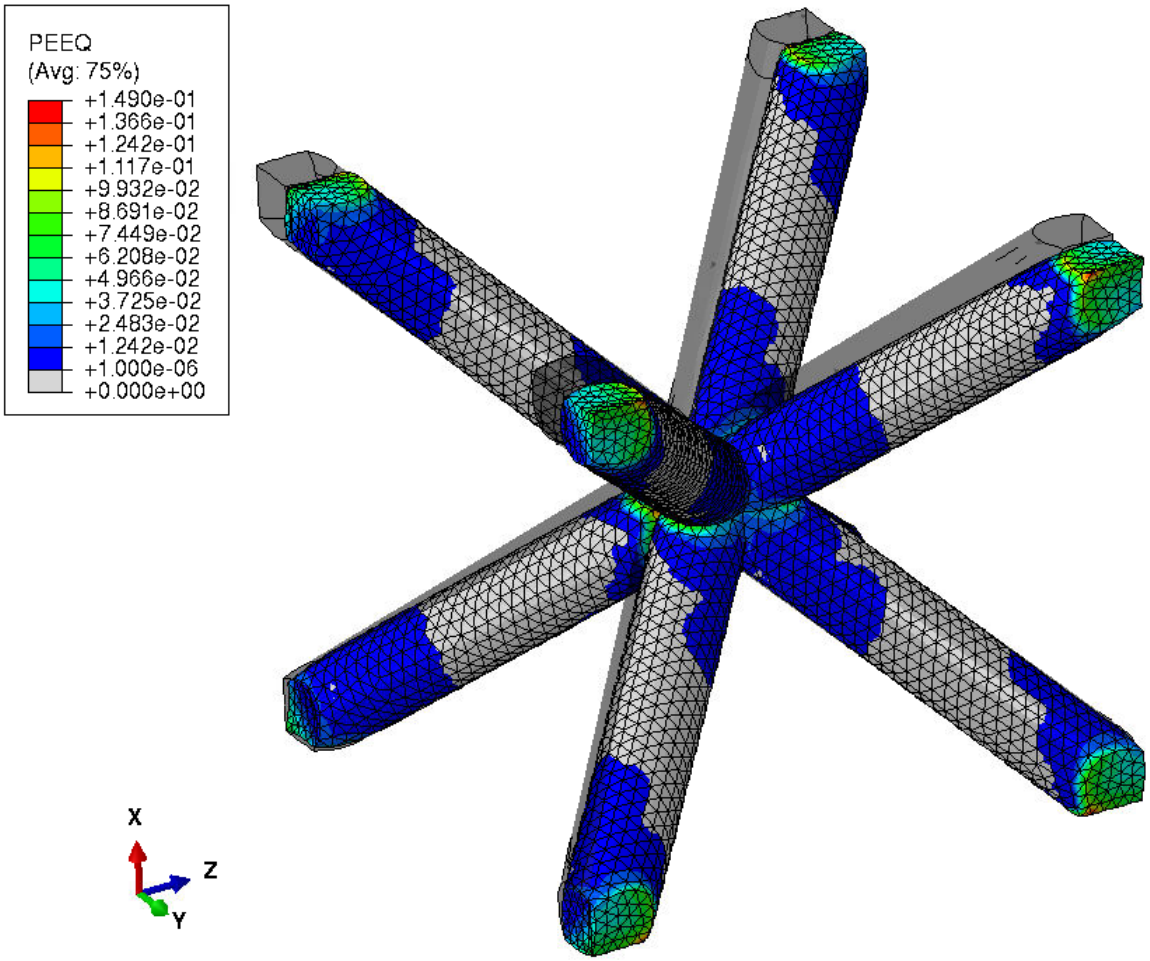

Fig. 6.9 The deformed and undeformed (shaded) shape of the solid element model, as well as the equivalent plastic strain (PEEQ) distribution for the simple shear XY load case at 2% engineering strain.

The results from the solid element model show the regions of the UC that have yielded. At 2% engineering strain (*Fig. 6.9*), it can be seen that the plastic zones are localized at the vertices of the UC. With further increase of the load to the UC, the plastic zones nonuniformly evolve towards the central regions of the struts. At the endpoint of the load case (3.75% engineering strain), shown in *Fig. 6.10*, all regions of the UC have yielded, with the highest plasticity still localized at the vertices.

The obtained engineering stress-strain curves from both modeling approaches are presented and compared in *Fig. 6.11*. The relevant effective shear stress component is shown, the remaining effective stress components are zero.

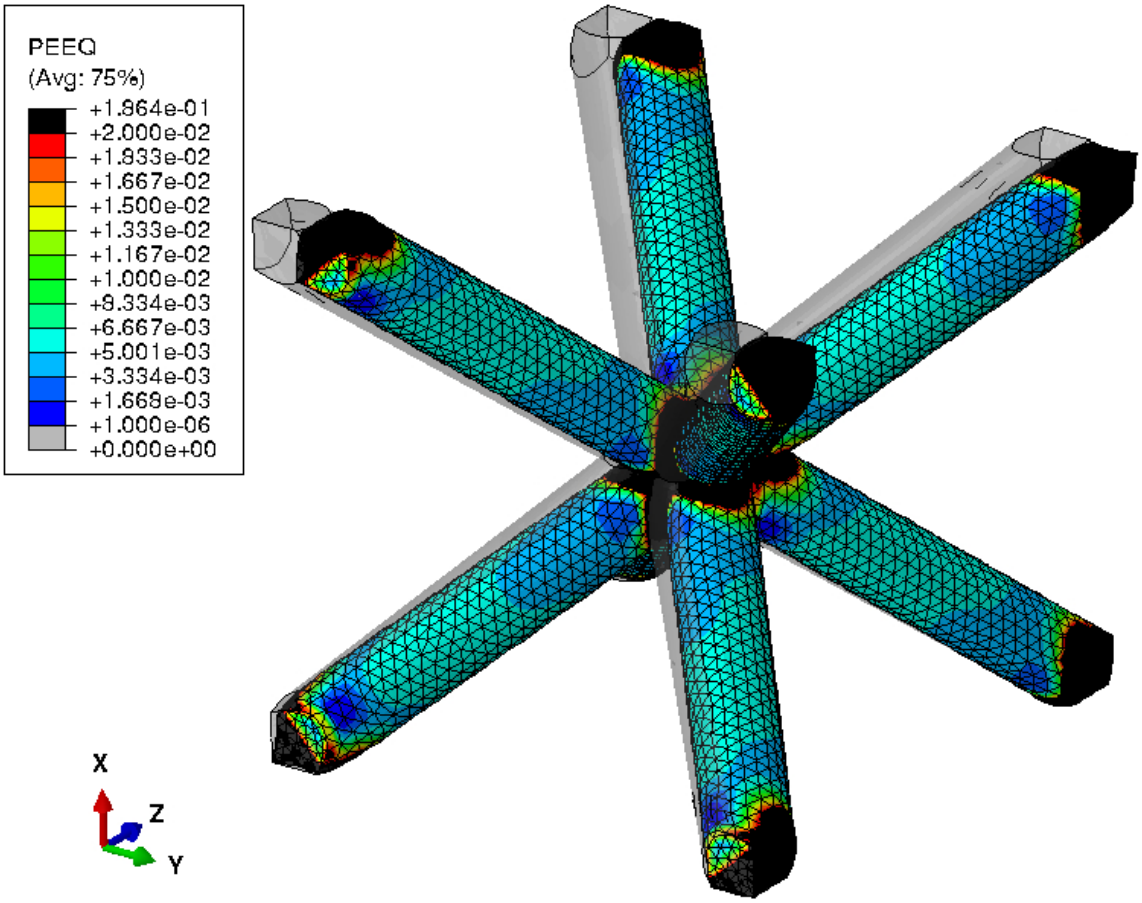

Fig. 6.10 The deformed and undeformed (shaded) shape of the solid element model, as well as the equivalent plastic strain (PEEQ) distribution at the endpoint (engineering strain of 3.75%) of the simple shear XY load case.

As already discussed, the struts are predominantly stretched or compressed, with some bending being present. Due to this bending deformation, plastic zones in the affected regions evolve, which causes a nonlinear relation between stress and strain in the elasto-plastic range. The curvature of this nonlinear region in the engineering stress-strain curve of the beam model is subtle since the corresponding bending deformation is very small. In comparison, the nonlinear region for the solid element model is considerably larger and extends up to around 2.5% engineering strain. This strong deviation in the deformation behavior between the models, which is also the cause for the contrast in the engineering stress-strain curves, is caused by the already discussed differences in the modeling approaches.

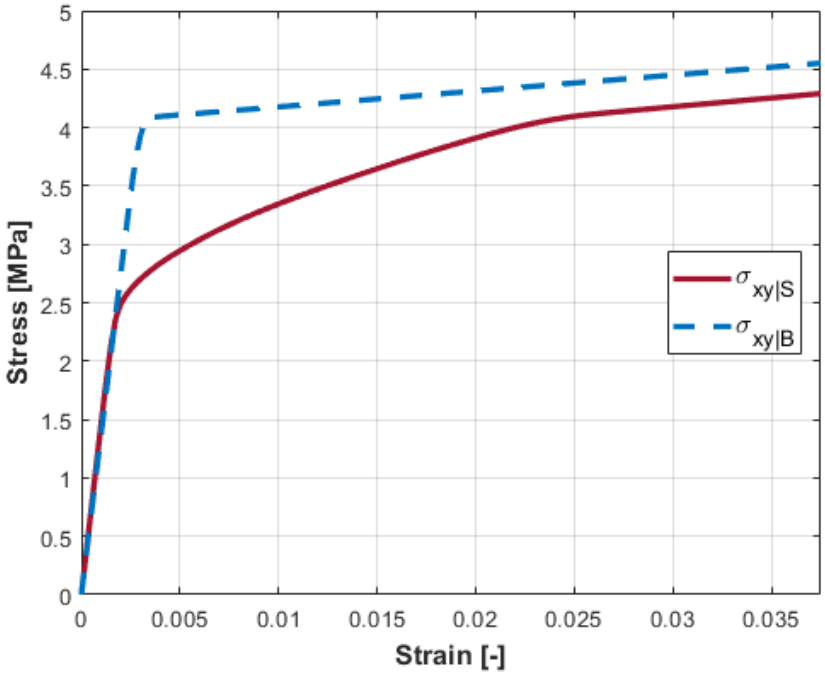

Fig. 6.11 The obtained engineering stress-strain curves for the simple shear XY load case for the beam model (index B) and solid element model (index S).

The slope values are shown in *Tab. 6.2*. The effective shear modulus $\tilde{M}$ values coincide with the ones from the linear elastic FEA. The effective tangent $\tilde{M}_{\mathrm{T}}$, and hardening $\tilde{M}_{\mathrm{H}}$ moduli from both modeling approaches are in a similar range. The $\tilde{M}_{\mathrm{T}}$ for the solid UC model is estimated in the region at around 3% engineering strain, whereas the one for the beam model is evaluated in the region around 2% engineering strain. From the results, it is concluded that the slopes of the engineering stress-strain curves are different for these modeling approaches, in both elastic and elastoplastic regions. Again, the differences in the results between the two models are caused by already discussed inaccuracies of the beam element modeling approach.

Tab. 6.2 The effective shear $\tilde{M}$, tangent $\tilde{M}_{\mathrm{T}}$, and hardening $\tilde{M}_{\mathrm{H}}$ moduli obtained from the engineering stress-strain curves for the simple shear XY load case.

	Beam UC	Solid UC
$\tilde{M}$ [MPa] lin. el. FEA	1374.73	1462.33
$\tilde{M}$ [MPa] from the slope	1374.16	1462.32
$\tilde{M}_{\mathrm{T}}$ [MPa] at 2% (3%) eng. strain for beam (solid) model	13.62	15.19
$\tilde{M}_{\mathrm{H}}$ [MPa] at 2% (3%) eng. strain for beam (solid) model	13.76	15.35

6.3.3 45° shear XY

The results that are obtained for the 45° shear XY load case are discussed in this section. The deformed and undeformed shapes of the UC at the endpoint (engineering strain of 3.75%) of the load case for the beam model (*Fig. 6.12*) and solid element model (*Fig. 6.13*) are shown in corresponding figures.

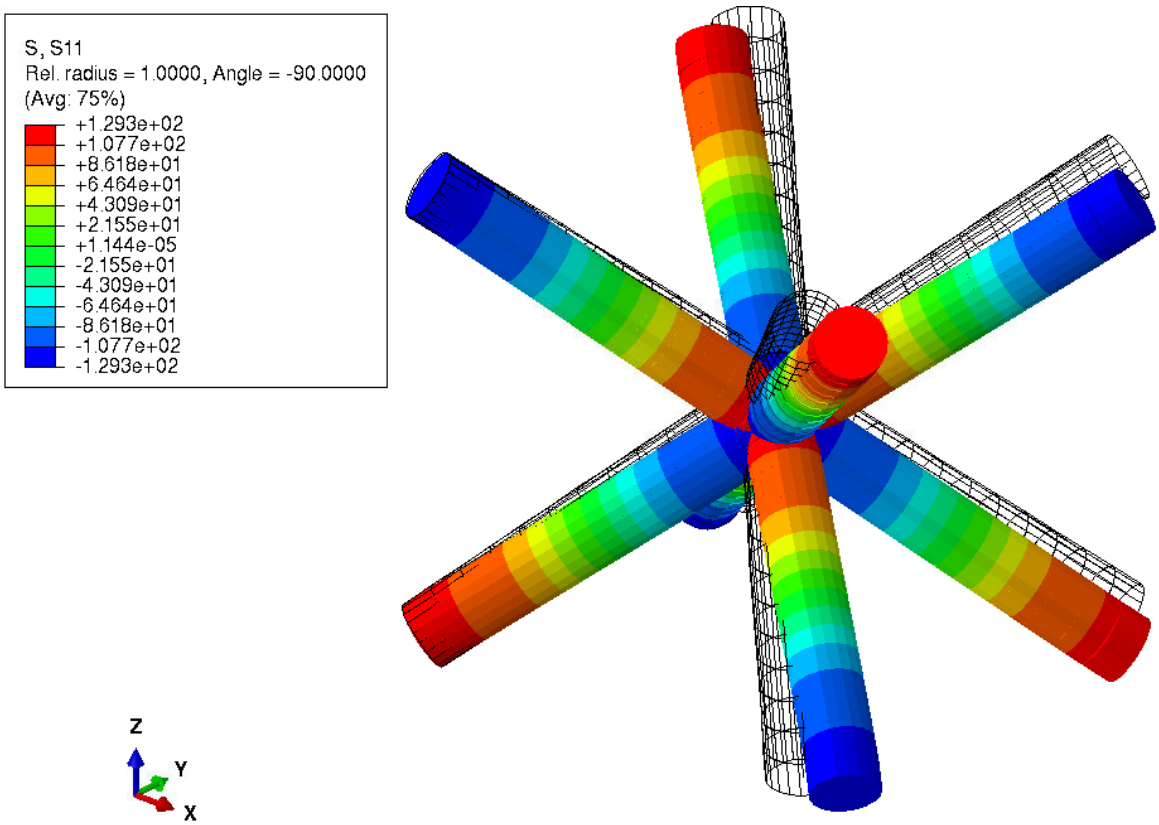

Fig. 6.12 The deformed and undeformed (wireframe) shape of the beam element model, as well as the axial stress (S11) distribution at the outermost fiber (*Fig. 3.3*) in the local orientation of beam elements at the endpoint (engineering strain of 3.75%) of the 45° shear XY load case.

From the deformed figure of the beam element UC (*Fig. 6.12*), as well as the axial stress (S11) distribution at the outermost fiber (*Fig. 3.3*) in the local orientation of beam elements, it is concluded that the bending of the struts is the predominant deformation behavior.

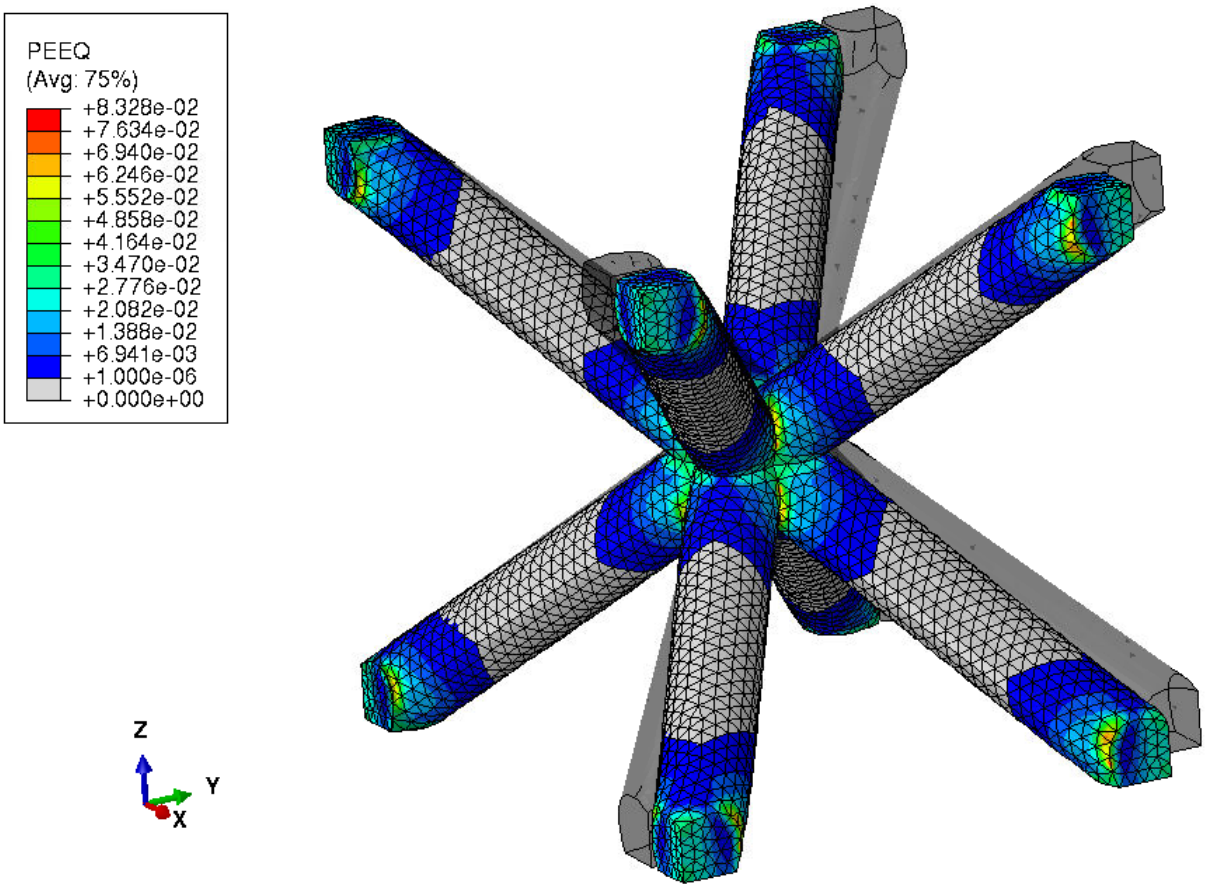

Fig. 6.13 The deformed and undeformed (shaded) shape of the solid element model, as well as the equivalent plastic strain (PEEQ) distribution at the endpoint (engineering strain of 3.75%) of the 45° shear XY load case.

The results from the solid element UC show that the plastic zones are localized at the vertices, and uniformly evolve towards the central regions of the struts with increasing strains. At the endpoint (engineering strain of 3.75%) of the load case, shown in *Fig. 6.13*, even though the plasticity has evolved, it remains mostly localized to the vicinity of the vertices.

The obtained engineering stress-strain curves from both modeling approaches are presented and compared in *Fig. 6.14*. The relevant effective normal stress components are shown, the remaining effective stress components are zero.

As previously discussed, the struts experience the highest bending deformation here, and thus deform the easiest out of all assessed single load cases. This is also reflected by the engineering stress-strain curves and their corresponding nonlinear elastoplastic regions. The explanations for the differences in the deformation behavior between the two models, as well as the differences in the overall engineering stress-strain curves, are the same as the ones provided for the bending deformation of the simple shear XY load case.

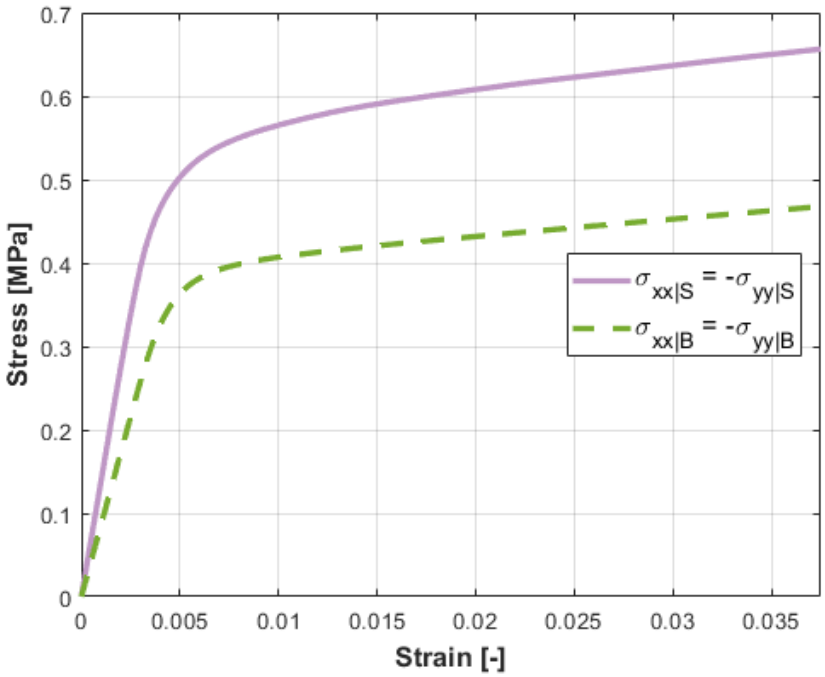

Fig. 6.14 The obtained engineering stress-strain curves for the 45° shear XY load case for the beam model (index B) and solid element model (index S).

The slope values are shown in *Tab. 6.3*. The effective shear moduli $\tilde{G}$ values coincide with the ones obtained from the linear elastic FEA. The effective tangent $\tilde{G}_{\mathrm{T}}$ moduli, estimated at around 2.5% engineering strain, and corresponding hardening $\tilde{G}_{\mathrm{H}}$ moduli values from models are in a similar range. From the results, it is concluded that the slopes of the engineering stress-strain curves are different for these modeling approaches, in both elastic and elastoplastic regions. Again, the differences between the results are caused by the inaccuracies of the beam element UC model.

Tab. 6.3 The effective shear $\tilde{G}$, tangent $\tilde{G}_{\mathrm{T}}$, and hardening $\tilde{G}_{\mathrm{H}}$ moduli obtained from the 45° shear XY load case.

	Beam UC	Solid UC
$\tilde{G}$ [MPa] lin. el. FEA	43.16	69.37
$\tilde{G}$ [MPa] from the slope	43.15	69.37
$\tilde{G}_{\mathrm{T}}$ [MPa] at 2.5% engineering strain	2.14	3.07
$\tilde{G}_{\mathrm{H}}$ [MPa] at 2.5% engineering strain	2.25	3.22

6.3.4 Uniaxial tension load case in the [100] direction

The results that are obtained for the uniaxial tension load case in the principal material direction [100] are discussed in this section. The deformed and undeformed shapes of the UC at the endpoint (engineering strain of 3.75%) of the load case for the beam model (*Fig. 6.15*) and solid element model (*Fig. 6.16*) are shown in corresponding figures.

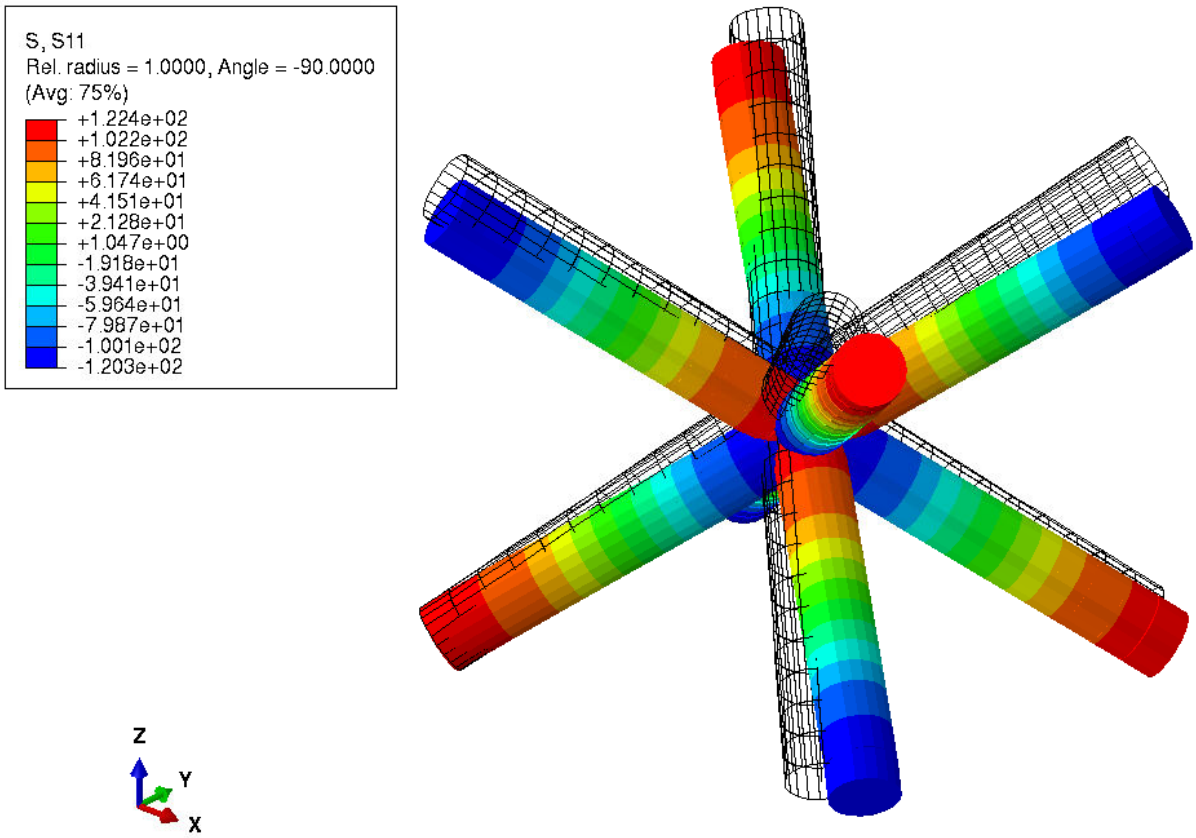

Fig. 6.15 The deformed and undeformed (wireframe) shape of the beam element model, as well as the axial stress (S11) distribution at the outermost fiber (*Fig. 3.3*) in the local orientation of beam elements at the endpoint (engineering strain of 3.75%) of the uniaxial tension [100] load case.

From the deformed figure of the beam element UC (*Fig. 6.15*), as well as the axial stress (S11) distribution at the outermost fiber (*Fig. 3.3*) in the local orientation of beam elements, it is concluded that the bending of the struts is the predominant deformation behavior.

The results from the solid element UC show that the plastic zones are localized at the vertices, and uniformly evolve towards the central regions of the struts with increasing strains. At the engineering strain of 3.75%, as shown in *Fig. 6.16*, even though plasticity has evolved, it remains mostly localized to the vicinity of the vertices.

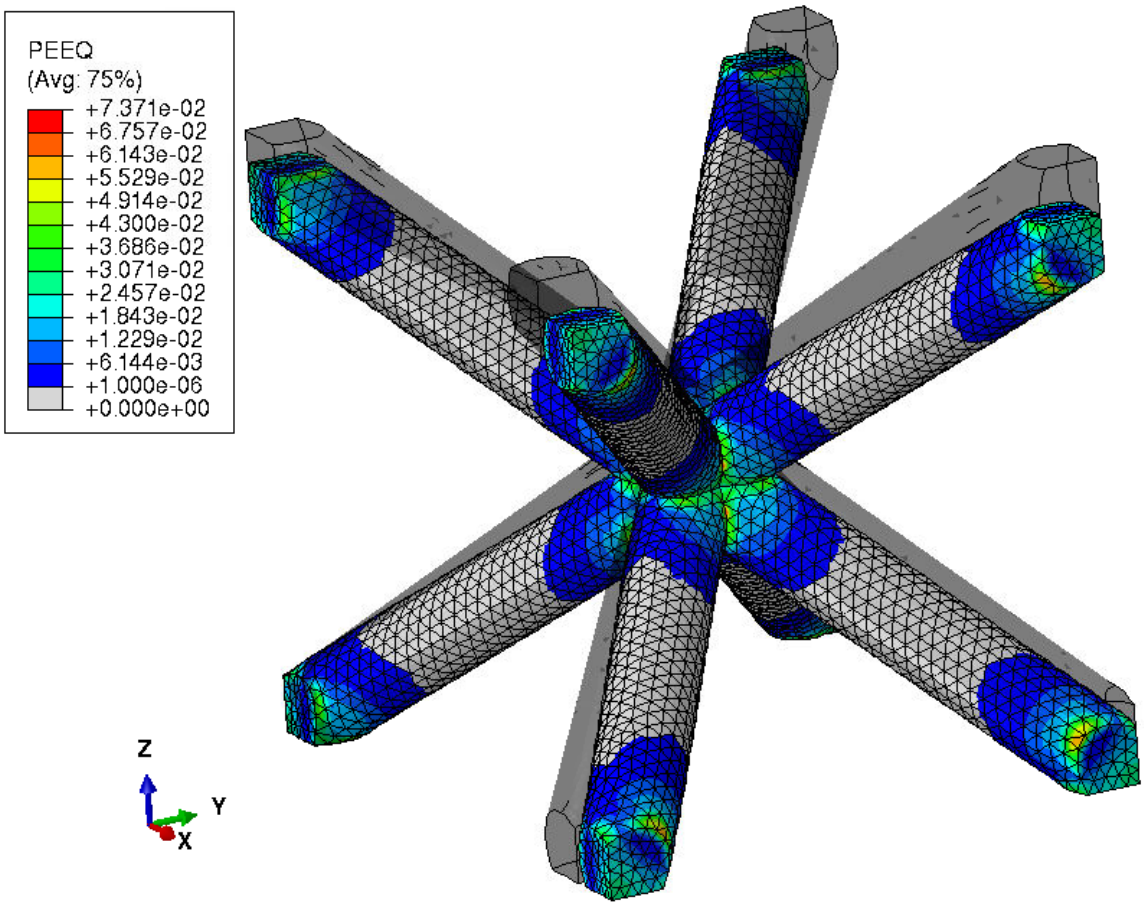

Fig. 6.16 The deformed and undeformed (shaded) shape of the solid element model, as well as the equivalent plastic strain (PEEQ) distribution at the endpoint (engineering strain of 3.75%) of the uniaxial tension [100] load case.

The obtained engineering stress-strain curves from both modeling approaches are presented and compared in *Fig. 6.17*. The relevant effective normal stress component is shown, the remaining effective stress components are zero.

The results from this load case show a lot of similarities to the 45° shear XY one since the bending of the struts is the predominant deformation mechanism in both. The differences between the two are caused by the amount of bending deformation, which is higher for the 45° shear XY load case. The explanations for the differences in the deformation behavior between the two modeling approaches and in the overall engineering stress-strain curves are the same as the ones provided for the bending deformation of the previous load cases.

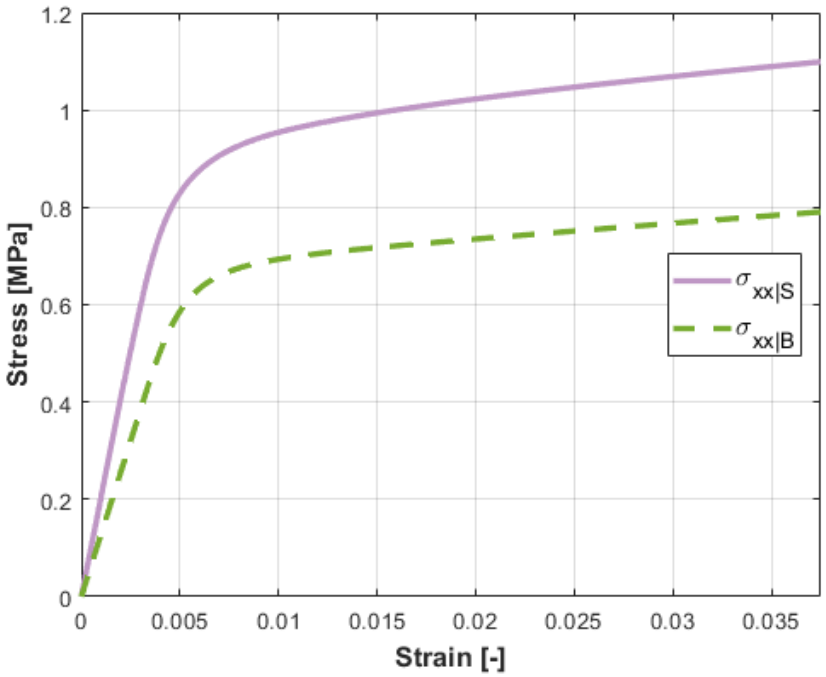

Fig. 6.17 The obtained engineering stress-strain curves for the uniaxial tension [100] load case for the beam model (index B) and solid element model (index S).

The slope values are shown in *Tab. 6.4*. The effective Young's moduli $\tilde{E}$ values coincide with the ones obtained from the linear elastic FEA. The effective tangent $\tilde{E}_{\mathrm{T}}$ moduli, estimated at around 2.5% engineering strain, and the corresponding hardening $\tilde{H}$ moduli values from both modeling approaches are also in a similar range. From the results, it is concluded that the slopes of the engineering stress-strain curves are different for these modeling approaches, in both elastic and elastoplastic regions. Again, the differences between the results are caused by the inaccuracies that come with the beam element UC model.

Tab. 6.4 The effective Young's $\tilde{E}$, tangent $\tilde{E}_{\mathrm{T}}$, and hardening $\tilde{H}$ moduli obtained from the engineering stress-strain curves for the uniaxial tension [100] load case.

	Beam UC	Solid UC
$\tilde{E}$ [MPa] lin. el. FEA	128.11	204.83
$\tilde{E}$ [MPa] from the slope	128.11	205.03
$\tilde{E}_{\mathrm{T}}$[MPa] at 2.5% engineering strain	3.33	4.99
$\tilde{H}$ [MPa] at 2.5% engineering strain	3.42	5.12

6.4 Two load cases applied in the single step

In this section, the results from the models where two different load cases are applied in a single step are discussed. This is achieved by superimposing the displacements that would be applied for the single load cases separately into a single step. The load cases that are assessed are combined simple shear XY and XZ, simple shear XY and hydrostatic tension, simple shear XY and 45° shear XY, as well as 45° shear XY and hydrostatic tension load cases. The corresponding BCs required to model them are shown in *Tab. 6.5*.

The comparison of the deformed and undeformed shapes for each of the modeling approaches under these load conditions is shown in the corresponding figures. The results are presented in the same way as for the single load cases. For the beam models, the axial stress (S11) distribution at the outermost fiber (*Fig. 3.3*) displayed in the local orientation of beams is shown. For the solid element models, the accumulated equivalent plastic strain (PEEQ) distribution is shown, according to which the plastic deformation behavior can be evaluated.

Tab. 6.5 Applied BCs to the UC for combined simple shear XY and XZ, simple shear XY and hydrostatic tension, simple shear XY and 45° shear XY, as well as 45° shear XY and hydrostatic tension load cases in a single step. The master node notation is based on *Fig. 2.3*. u is the desired displacement that is applied.

Load case	Master nodes	u_x	u_y	u_z
Simple shear XY and XZ	SWB	0	0	0
	SEB	0	u	u
	NWB	0	0	0
	SWT	0	0	0
Simple shear XY and hydrostatic tension	SWB	0	0	0
	SEB	u	u	0
	NWB	0	u	0
	SWT	0	0	u
Simple shear XY and 45° shear XY	SWB	0	0	0
	SEB	u	u	0
	NWB	0	$-u$	0
	SWT	0	0	0
45° shear XY and hydrostatic tension	SWB	0	0	0
	SEB	$2 \cdot u$	0	0
	NWB	0	0	0
	SWT	0	0	u

6.4.1 Simple shear XY and XZ load cases

The results that are obtained for the combined simple shear XY and XZ load cases in the single step are discussed in this section. The deformed and undeformed shapes of the UC at the endpoint (engineering strain of 3.75%) of the load case for the beam model (*Fig. 6.18*) and solid element model (*Fig. 6.19*) are shown in corresponding figures.

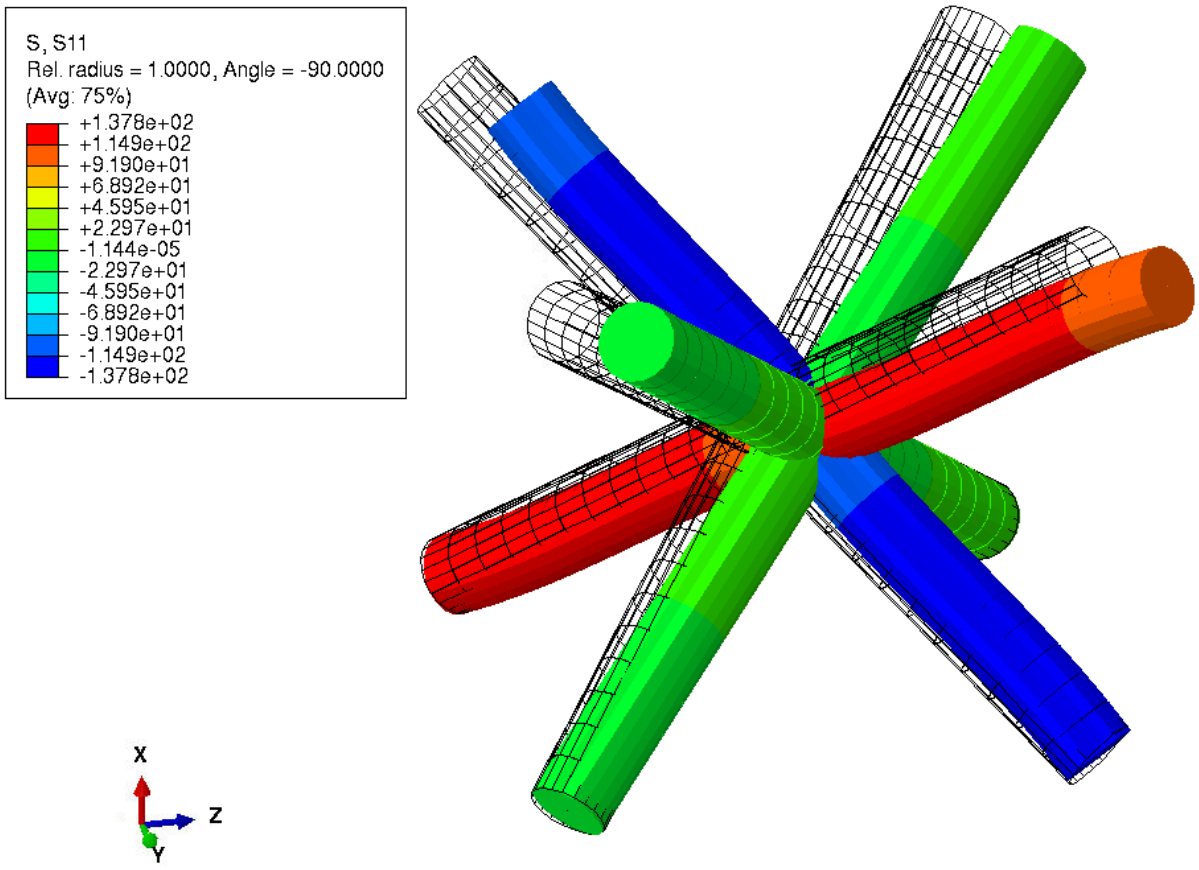

Fig. 6.18 The deformed and undeformed (wireframe) shape of the beam element model, as well as the axial stress (S11) distribution at the outermost fiber (*Fig. 3.3*) in the local orientation of beam elements at the endpoint (engineering strain of 3.75%) of the combined simple shear XY and XZ load cases in the single step.

From the deformed figure of the beam element UC (*Fig. 6.18*), as well as the axial stress (S11) distribution at the outermost fiber (*Fig. 3.3*) in the local orientation of beam elements, it is concluded that four of the struts (green colored ones in *Fig. 6.18*) are almost unloaded, while the remaining four are either compressed or stretched, with some amount of bending being present.

For the sake of clarity in the description of the deformation mechanism of struts, an assumption is made that the combined load case is restricted to the linear elastic regime and that it occurs in two different steps. For the single simple shear load case, the struts forming two of the space diagonals are stretched, while the remaining struts are compressed. As the load case transitions from the simple shear XY to XZ, one of the stretched legs (in the [111] direction) is additionally stretched, while the remaining stretched leg is relieved. The initially present tensile stress in the relieved leg is balanced out by an approximately equal compressive stress, as the transition unfolds. Simultaneously, an analogous mechanism occurs in the remaining (compressed) legs, where one of the legs is additionally compressed while the other one is relieved.

For the combined single-step load case, the difference is that the UC's face perpendicular to the x-axis moves directly in the direction of the face diagonal. In this way, even with the elastoplastic material modeling, the "relieved" struts experience almost no deformation and remain mostly unloaded from the beginning up to the endpoint of the load case.

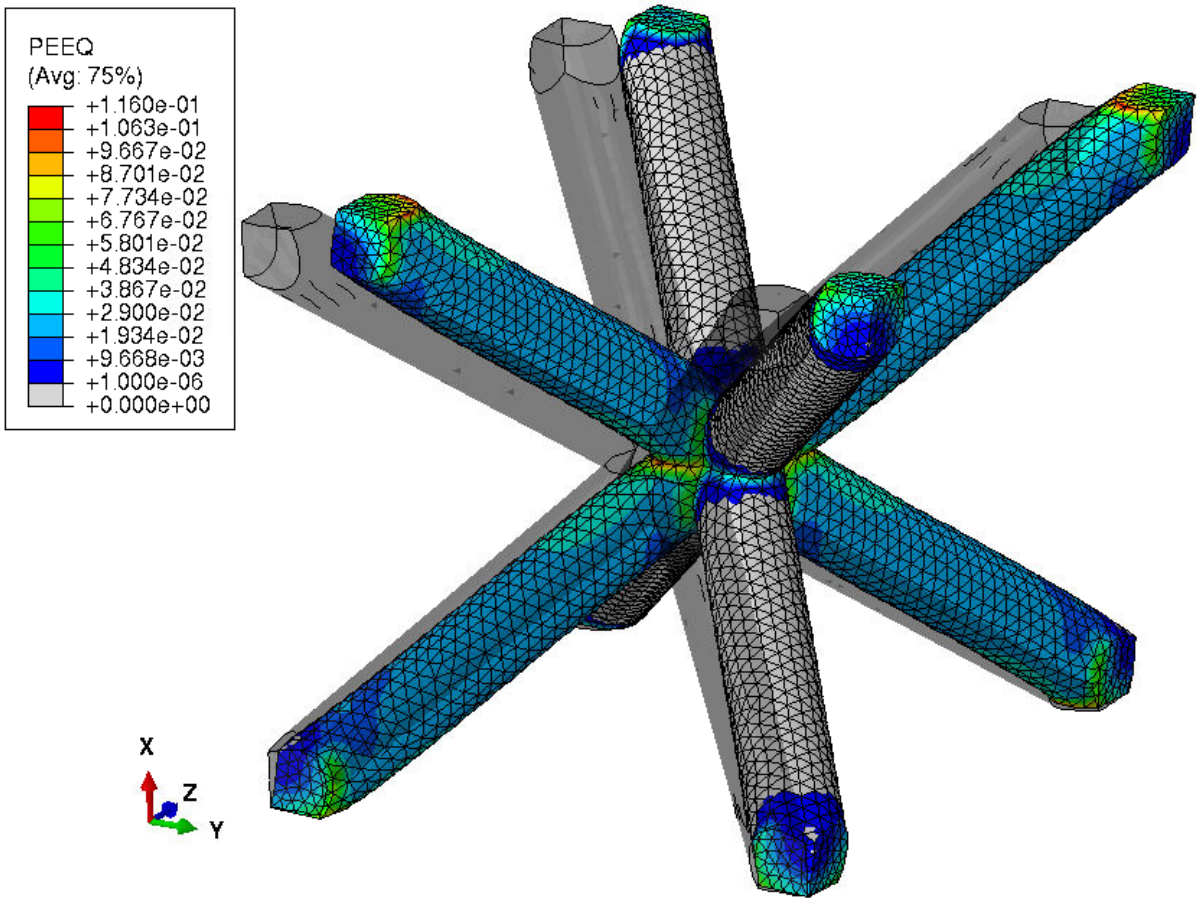

Fig. 6.19 The deformed and undeformed (shaded) shape of the solid element model, as well as the equivalent plastic strain (PEEQ) distribution at the endpoint (engineering strain of 3.75%) for the combined simple shear XY and XZ load cases in the single step.

The results from the solid element UC at the engineering strain of 3.75% (*Fig. 6.19*) show that the plastic zones are present in the compressed and stretched struts of the UC model, and their evolution from vertices towards the central regions of the struts follows a similar behavior as in the single simple shear XY load case (*Fig. 6.9*). The relieved struts have some plasticity present in the vicinity of the vertices but are overall unaffected by the plastic deformation since they remain predominantly unloaded throughout the load case.

The obtained engineering strain-time and engineering stress-time curves from both modeling approaches are shown and compared in *Fig. 6.20*. The values from the stress and strain tensors, which are rotated by 45° around the x-axis, are shown as well. With this transformation, the y-axis coincides with the face diagonal direction, and only one shear stress and strain component is present. Additionally, the engineering stress-strain plot of the transformed shear stress and strain components is shown in figure *Fig. 6.21*. The relevant transformed and untransformed effective shear stress and shear angle components are shown, the remaining ones are zero. The slope values for the effective shear $\tilde{M}'$, tangent $\tilde{M}'_{\mathrm{T}}$, and hardening $\tilde{M}'_{\mathrm{H}}$ moduli, obtained from this plot, are shown in *Tab. 6.6*.

From the results, it can be seen that the engineering stress-time curves from the beam and solid model are more in agreement, compared to the strong differences seen in the nonlinear elastoplastic from the single simple shear XY load case (*Fig. 6.11*). The significantly less pronounced nonlinear region of the solid model's engineering stress-time curve is presumably caused by two legs experiencing almost no deformation, and less bending in the remaining two.

The results obtained from the slopes of the transformed engineering stress-strain curves are also compared to the ones obtained from the single simple shear XY load case (*Tab. 6.2*). The values of the effective shear moduli $\tilde{M}'$ and $\tilde{M}$, for the transformed engineering stress-strain curve and the single simple shear XY load case respectively, coincide for both UC models. The effective tangent moduli, evaluated at around 3% engineering strain, and the corresponding effective hardening moduli values are in the same range compared to the results from the single simple shear XY load case.

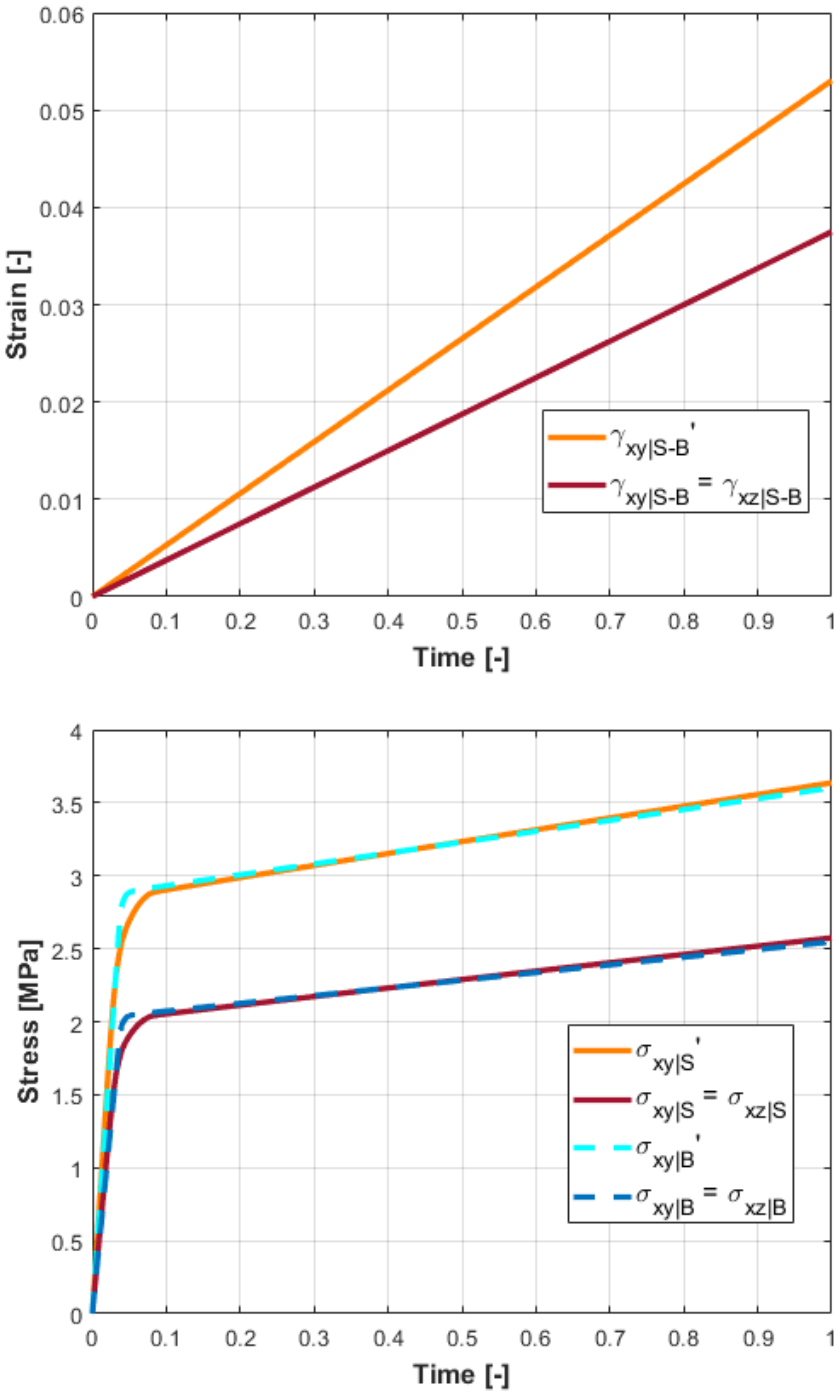

Fig. 6.20 The obtained engineering strain-time (top) and engineering stress-time (bottom) curves for the combined simple shear XY and XZ load cases in a single step for the beam model (index B) and solid element model (index S). The index $B - S$ in the engineering strain-time plot denotes that the applied strain components are equal for both solid and beam element models. The effective values with an apostrophe are the ones from the stress and strain tensors rotated by 45° around the x-axis.

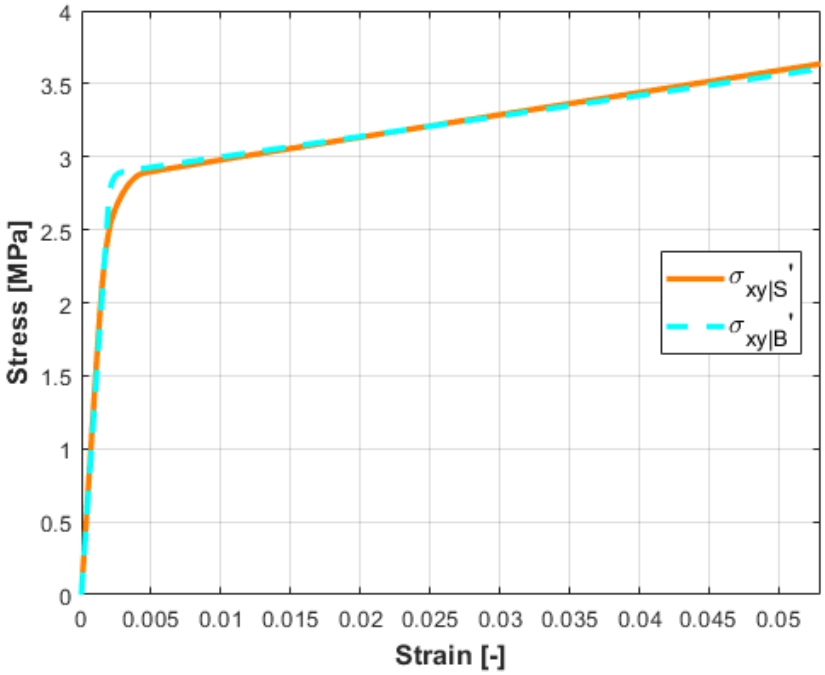

Fig. 6.21 The obtained engineering stress-strain curve for the combined simple shear XY and XZ load cases in a single step for the beam model (index B) and solid element model (index S), where the stress and strain tensors are rotated by 45° around the x-axis.

Tab. 6.6 The effective shear $\tilde{M}'$, tangent $\tilde{E}'_{\mathrm{T}}$, and hardening $\tilde{H}'$ moduli obtained from the slopes of the engineering stress-strain curve of the transformed stress and strain tensors for the combined simple shear XY and XZ load cases. These results are compared to the corresponding values obtained from the single simple shear XY load case (*Tab. 6.2*).

	Beam UC	Solid UC
$\tilde{M}$ [MPa] single simple shear XY	1374.16	1462.32
$\tilde{M}'$ [MPa]	1374.73	1462.29
$\tilde{M}_{\mathrm{T}}$ [MPa] single simple shear XY	13.62	15.19
$\tilde{M}'_{\mathrm{T}}$ [MPa] at 3% engineering strain	14.06	15.30
$\tilde{M}_{\mathrm{H}}$ [MPa] single simple shear XY	13.76	15.35
$\tilde{M}'_{\mathrm{H}}$ [MPa] at 3% engineering strain	14.21	15.48

6.4.2 Simple shear XY and hydrostatic load cases

The results that are obtained for the combined simple shear XY and hydrostatic tension load cases in the single step are discussed in this section. The deformed and undeformed shapes of the UC at the endpoint (engineering strain of 3.75%) of the load case for the beam model (*Fig. 6.22*) and solid element model (*Fig. 6.23*) are shown in corresponding figures.

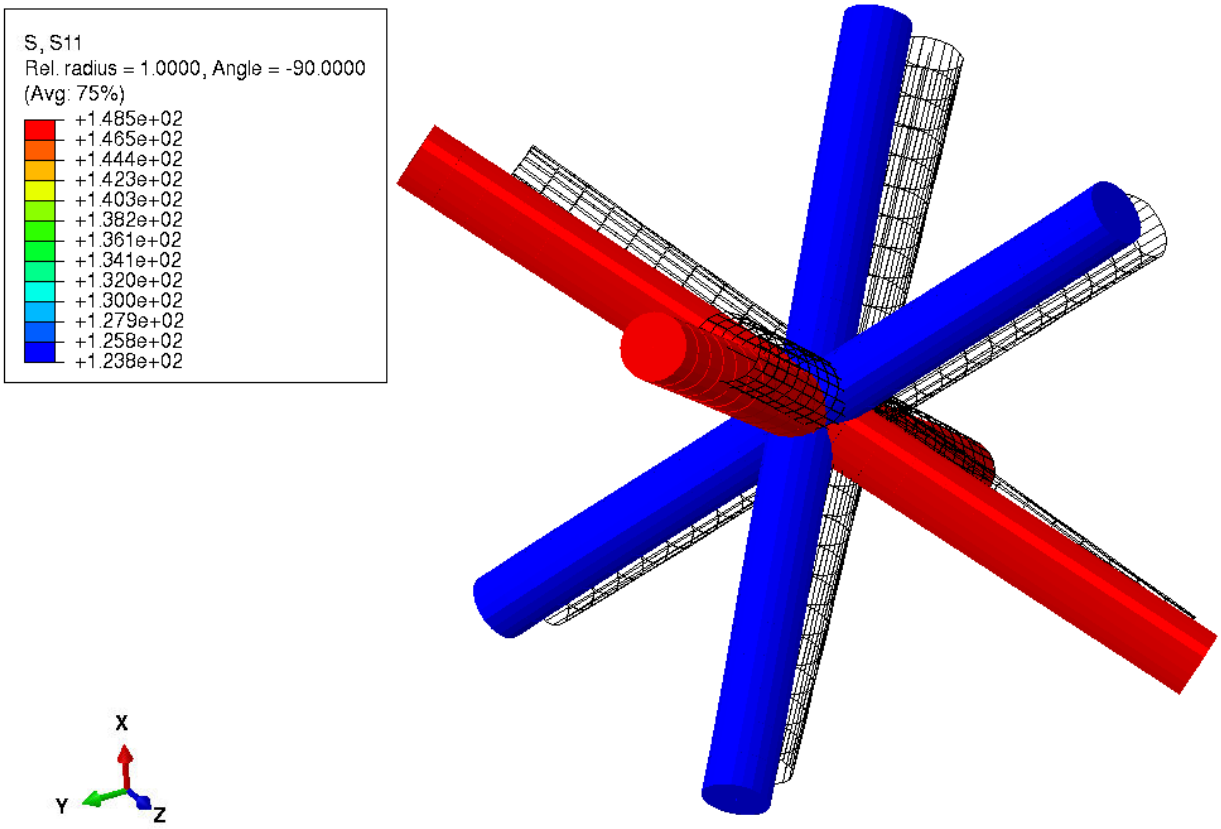

Fig. 6.22 The deformed and undeformed (wireframe) shape of the beam element model, as well as the axial stress (S11) distribution at the outermost fiber (*Fig. 3.3*) in the local orientation of beam elements at the endpoint (engineering strain of 3.75%) of the combined simple shear XY and hydrostatic tension load cases in the single step.

From the deformed figure of the beam element UC (*Fig. 6.22*), as well as the axial stress (S11) distribution at the outermost fiber (*Fig. 3.3*) in the local orientation of beam elements, it is concluded that all of the struts are under pure tension at the endpoint (engineering strain of 3.75%) of the load case. The red-colored struts experience higher stress compared to the blue-colored ones.

Both involved load cases are predominantly governed by stretching and compression (for the simple shear XY). Some amount of bending deformation of the struts, stemming from the simple shear XY, is minimized by the pure tension resulting from the hydrostatic load. In the beginning, superimposing the load cases leads to the deformation state, where the stretched legs from the simple shear XY are additionally stretched, and the compressed ones are also stretched. With the increase in load, the ”initially” compressed struts are further stretched, but so are the ”initially” stretched ones, which leads to the difference in the amount of stress experienced by struts at the end of the load case.

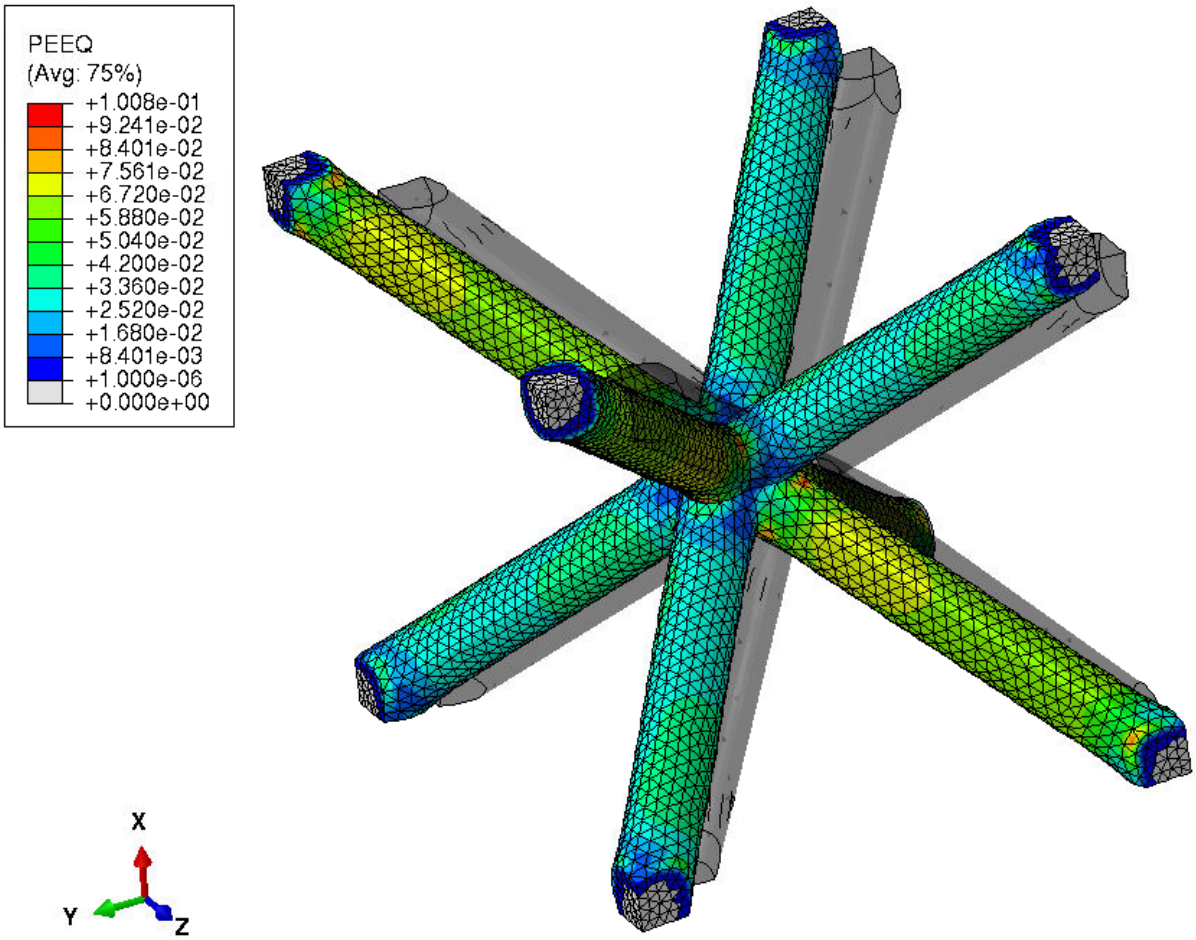

Fig. 6.23 The deformed and undeformed (shaded) shape of the solid element model, as well as the equivalent plastic strain (PEEQ) distribution at the endpoint (engineering strain of 3.75%) of the combined simple shear XY and hydrostatic tension load cases in the single step.

The results from the solid element model at the engineering strain of 3.75% (*Fig. 6.23*), show that the plastic zones are present in all regions of the UC, except on the tips of the struts. The four struts that overall experience higher stresses (light green in *Fig. 6.23*), are the first to yield and also have a higher amount of plasticity, compared to the remaining ones (turquoise in *Fig. 6.23*).

The obtained engineering strain-time and engineering stress-time curves from both modeling approaches are presented and compared in *Fig. 6.24*. The relevant effective shear and normal stress, shear angle, and normal strain components are shown, the remaining ones are zero.

When looking at the results from both models, the engineering stress-time curves show similar behavior. This is understandable since the combined load case is dominated by the stretching of the struts, while the bending deformation is minimized. As already discussed, from the beginning, two of the legs experience higher tensile stresses compared to the remaining two. As the shear stress component starts to drop from its peak point, the lower-stressed legs start catching up to the higher-stressed ones. This culminates at the point where the shear stress component drops almost to zero, and all legs experience roughly the same amount of tensile stress, i.e. only the hydrostatic load case is "active" at this point. Afterward, the differences between the legs, and the shear stress component gradually rise again.

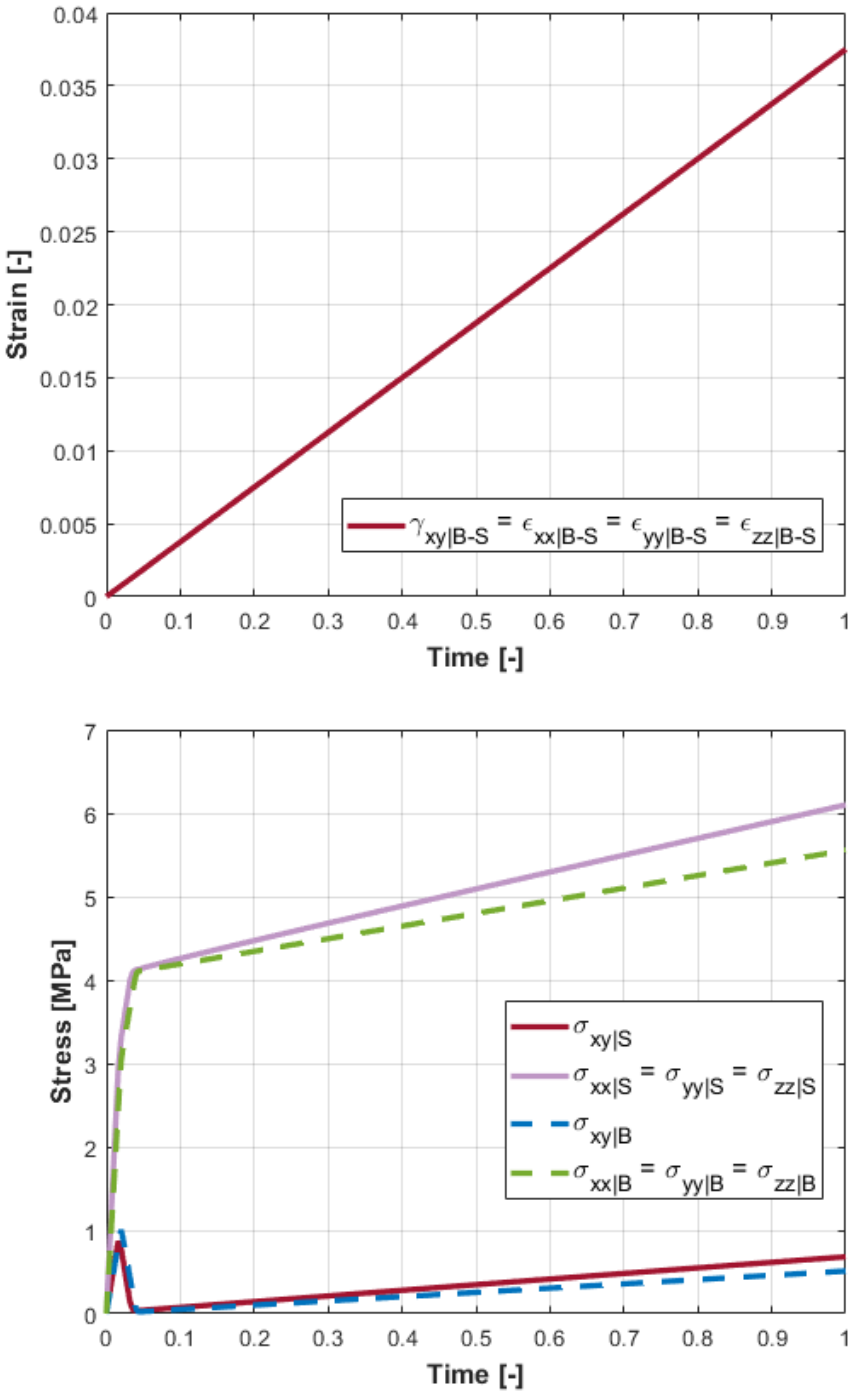

Fig. 6.24 The obtained engineering strain-time (top) and engineering stress-time (bottom) curves for the combined simple shear XY and hydrostatic tension load cases in a single step for the beam model (index B) and solid element model (index S). The index $B - S$ in the engineering strain-time plot denotes that the applied strain components are equal for both solid and beam element models.

6.4.3 Simple shear XY and 45° shear XY load cases

The results that are obtained for the combined simple shear XY and 45° shear XY load cases in the single step are discussed in this section. The deformed and undeformed shapes of the UC at the endpoint (engineering strain of 3.75%) of the load case for the beam model (*Fig. 6.25*), solid element model at 2% engineering strain (*Fig. 6.26*), and at 3.75% engineering strain (*Fig. 6.27*) are shown in corresponding figures.

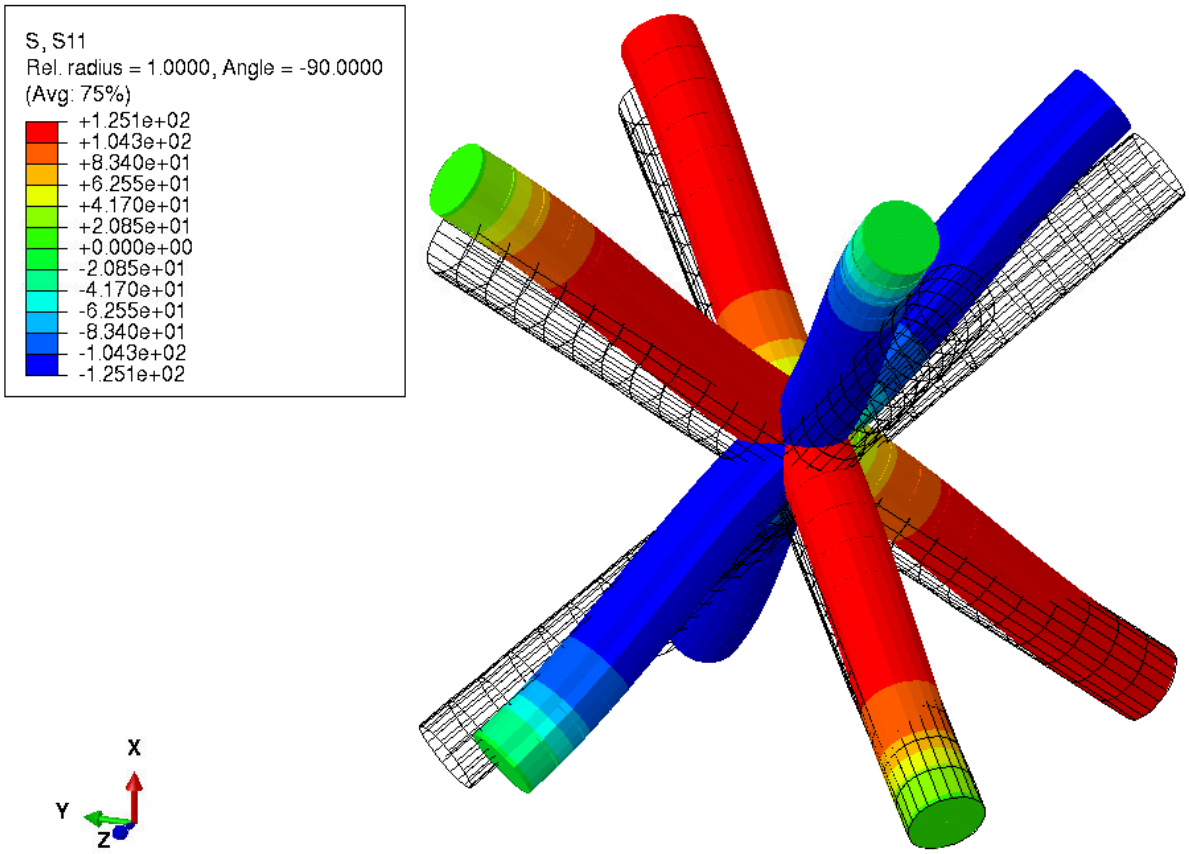

Fig. 6.25 The deformed and undeformed (wireframe) shape of the beam element model, as well as the axial stress (S11) distribution at the outermost fiber (*Fig. 3.3*) in the local orientation of beam elements at the endpoint (engineering strain of 3.75%) of the combined simple shear XY and 45° shear XY load cases in the single step.

The struts experience predominantly compression and stretching, with some amount of bending under the simple shear XY load, whereas for the 45° shear XY load case, they experience a significant amount of bending deformation. Superimposing these two load cases, results in a deformation state with compression and tension of struts, and an overall increase in present bending deformation. This behavior is confirmed by the results from the beam element UC at the engineering strain of 3.75% (*Fig. 6.25*).

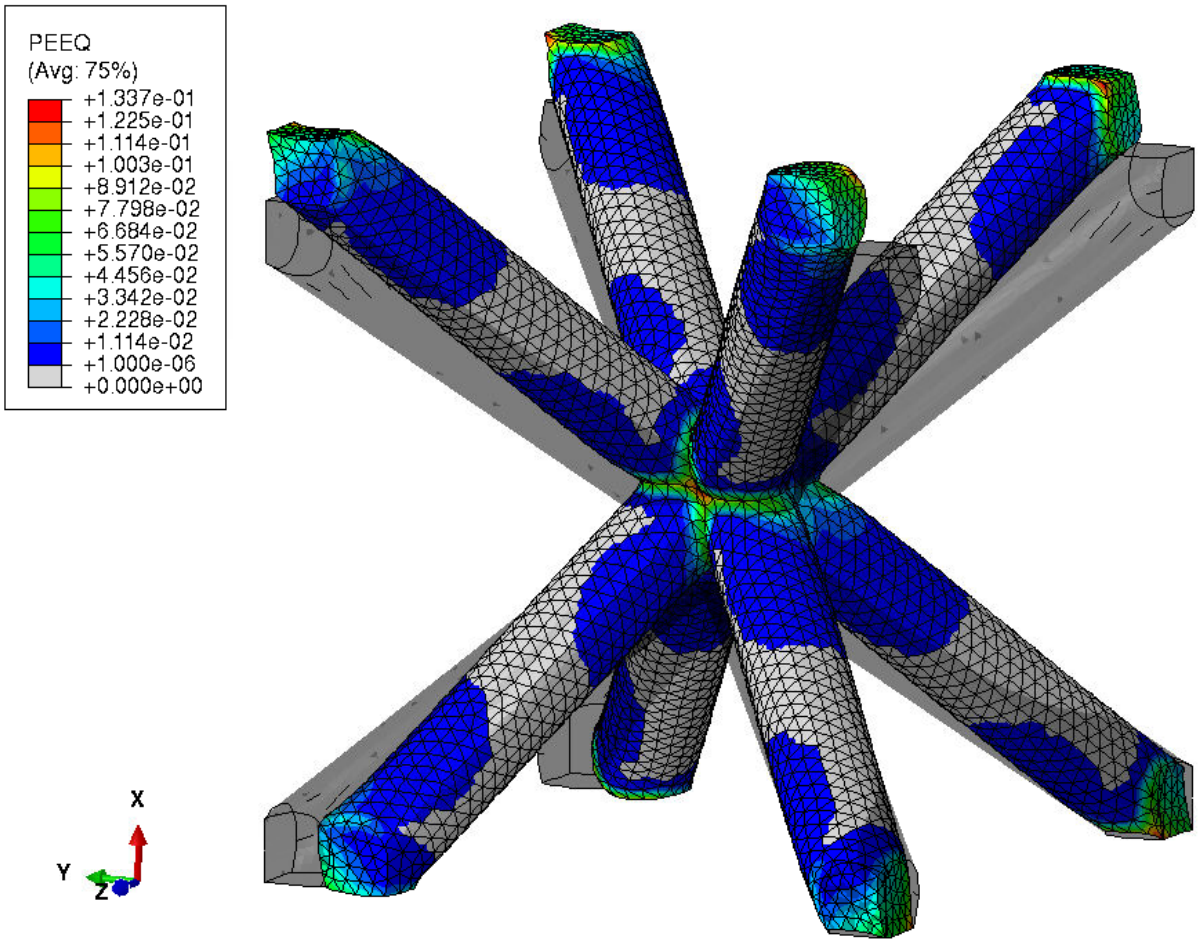

Fig. 6.26 The deformed and undeformed (shaded) shape of the solid element model, as well as the equivalent plastic strain (PEEQ) distribution at the 2% engineering strain of the combined simple shear XY and 45° shear XY load cases in the single step.

The nonuniform progress of plasticity evolution with increasing load starting from the vicinity of the vertices towards the central regions of the struts can be observed for the solid element UC at the 2% engineering strain (*Fig. 6.26*). This is comparable to the plastic deformation that occurs under the single simple shear XY load case at 2% engineering strain (*Fig. 6.9*), which is understandable, as this load case dominates the overall deformation behavior. When the endpoint (engineering strain of 3.75%) of the load case is reached, shown in *Fig. 6.27*, the plasticity is present in almost all regions of the solid element UC, except for some small surface zones of the struts. Presumably, this is caused by the increase in the bending deformation, compared to the single simple shear XY load case.

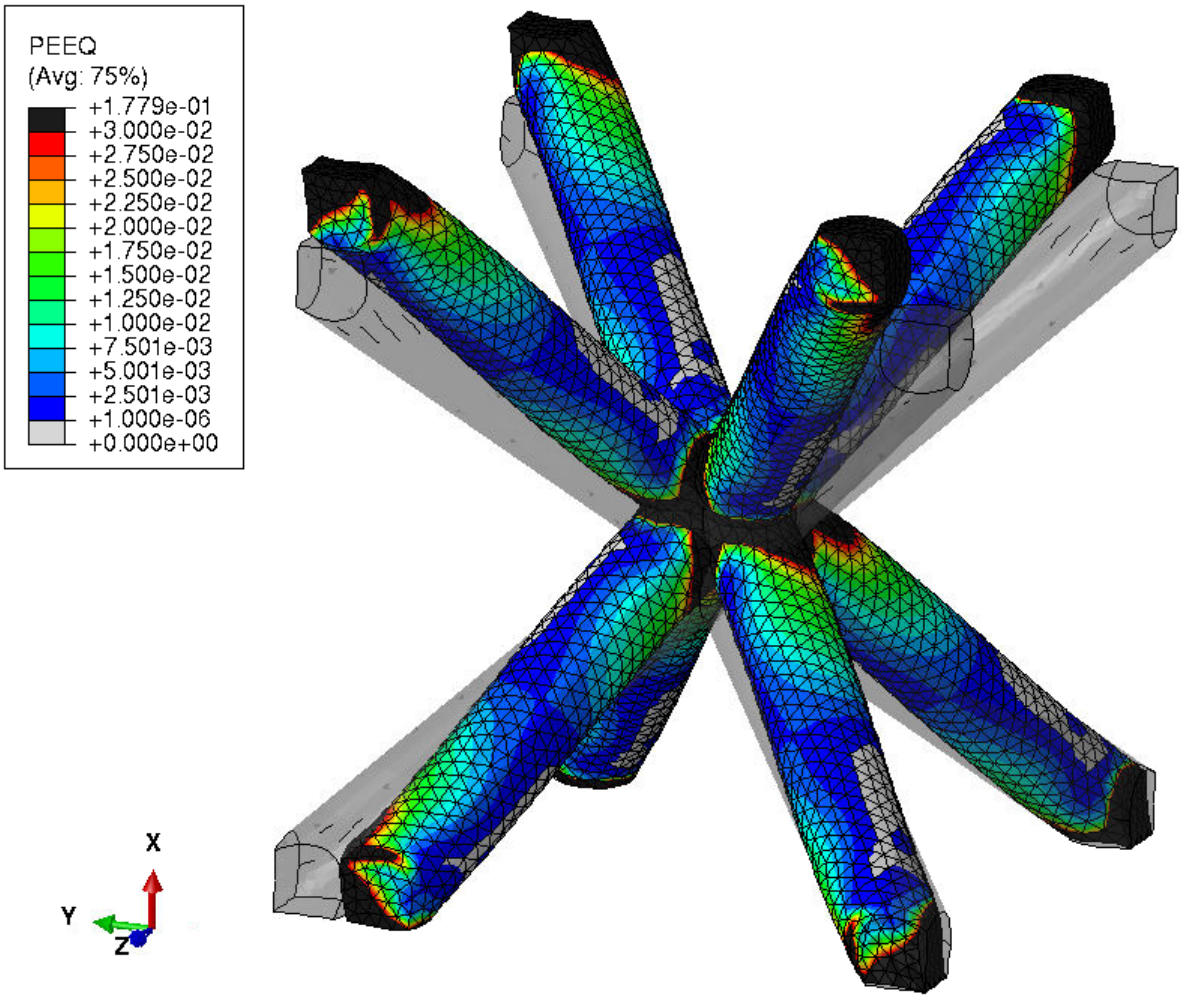

Fig. 6.27 The deformed and undeformed (shaded) shape of the solid element model, as well as the equivalent plastic strain (PEEQ) distribution at the endpoint (engineering strain of 3.75%) of the combined simple shear XY and 45° shear XY load cases in the single step.

The obtained engineering strain-time and engineering stress-time curves from both modeling approaches are presented and compared in *Fig. 6.28*. The relevant effective normal and shear stress, shear angle, and normal strain components are shown, the remaining ones are zero. The effective stress and strain components from the 45° shear XY load case are presented in their form before the transformation, i.e. as normal stresses and strains.

As already discussed, the struts experience increased bending deformation. This is observed from the engineering stress-time plot as well since the nonlinear elastoplastic zones of the shear stress components are broader compared to the results from the single simple shear XY load case (*Fig. 6.11*). For the beam element model, the stress components corresponding to the 45° shear XY drop to almost zero, after their peak at the time value of around 0.1, and remain in this range up until the end. This leads to the conclusion, that in this range only the simple shear XY load case is "active", i.e. it dominates the overall deformation behavior. For the solid element model, these stress components gradually decrease but do not drop to zero. In the same manner, it can be concluded that the simple shear XY also dominates the overall behavior, but that the contribution of the 45° shear XY is larger compared to the beam element model. The differences in the results between the modeling approaches are again caused by the previously discussed inaccuracies of the beam element model.

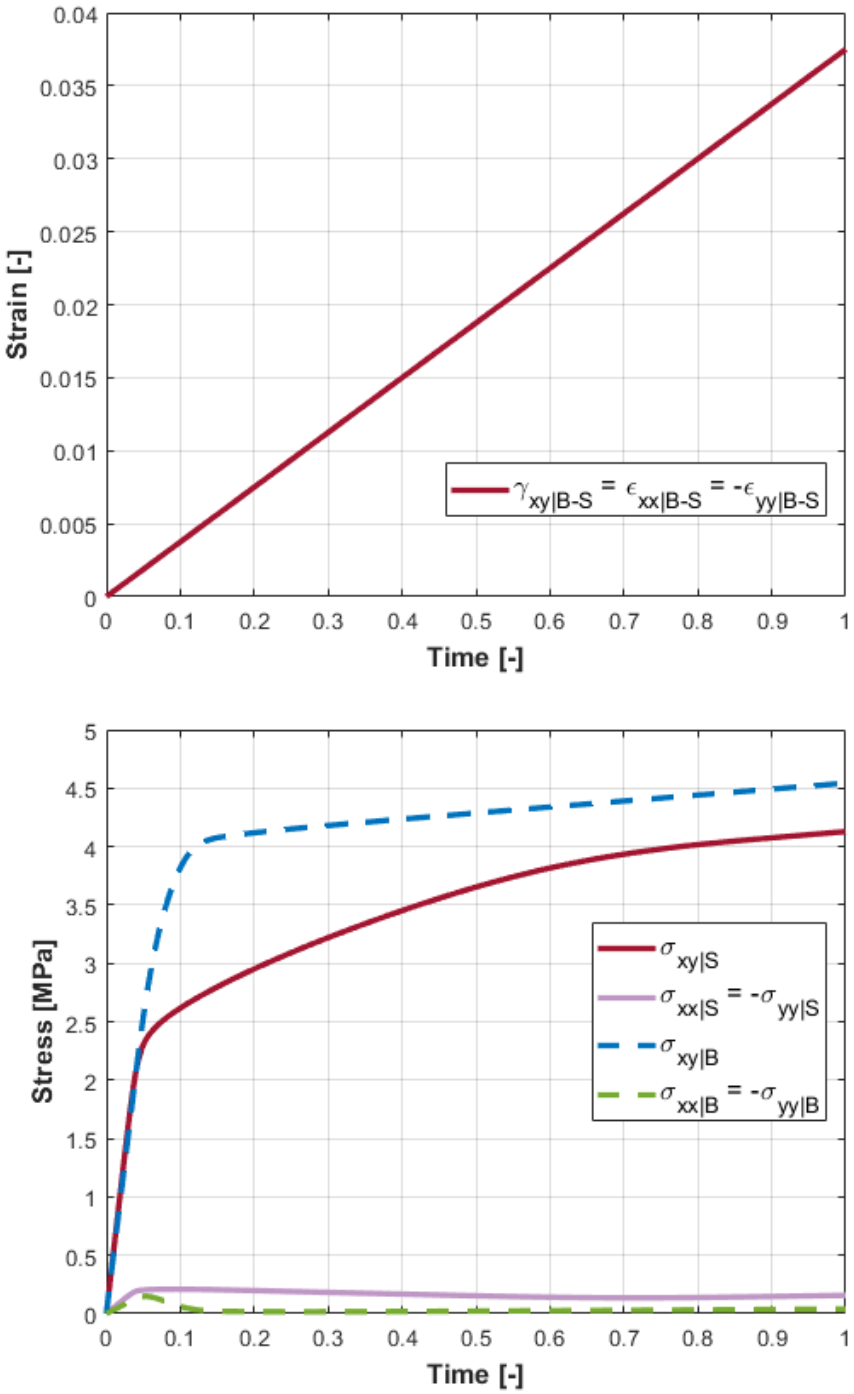

Fig. 6.28 The obtained engineering strain-time (top) and engineering stress-time (bottom) curves for the combined simple shear XY and 45° shear XY load cases in a single step for the beam model (index B) and solid element model (index S). The index $B - S$ in the engineering strain-time plot denotes that the applied strain components are equal for both solid and beam element models.

6.4.4 45° shear XY and hydrostatic load cases

The results that are obtained for the combined 45° shear XY and hydrostatic tension load cases in the single step are discussed in this section. The deformed and undeformed shapes of the UC at the endpoint (engineering strain of 3.75%) of the load case for the beam model (*Fig. 6.29*) and solid element model (*Fig. 6.30*) are shown in corresponding figures.

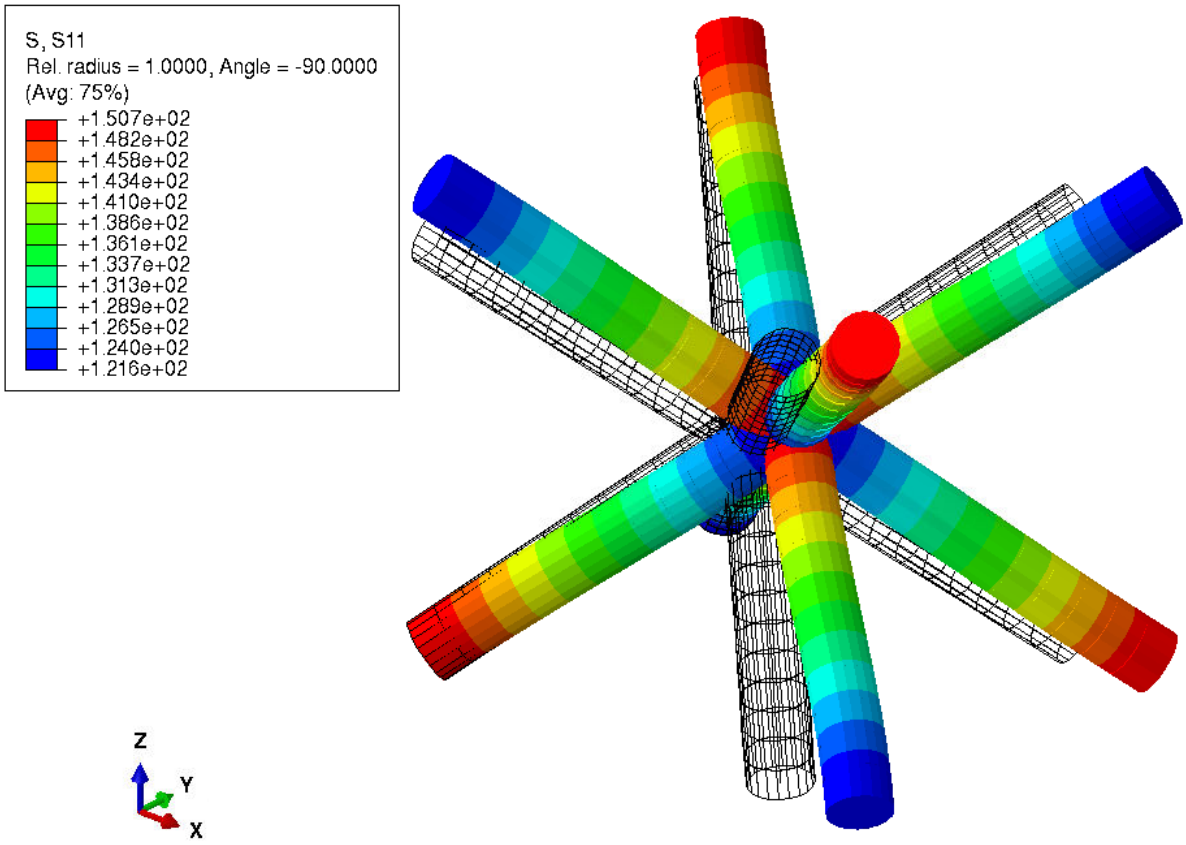

Fig. 6.29 The deformed and undeformed (wireframe) shape of the beam element model, as well as the axial stress (S11) distribution at the outermost fiber (*Fig. 3.3*) in the local orientation of beam elements at the endpoint (engineering strain of 3.75%) of the combined 45° shear XY and hydrostatic tension load cases in the single step.

The struts experience pure tension under the hydrostatic load and significant bending deformation under the 45° shear XY one. Superimposing these two load cases leads to the deformation state where the struts are predominantly stretched, with some amount of bending being present. Overall, the bending deformation is minimized by the stretching of the struts. This behavior is confirmed by the results from the beam element UC at the engineering strain of 3.75% (*Fig. 6.29*).

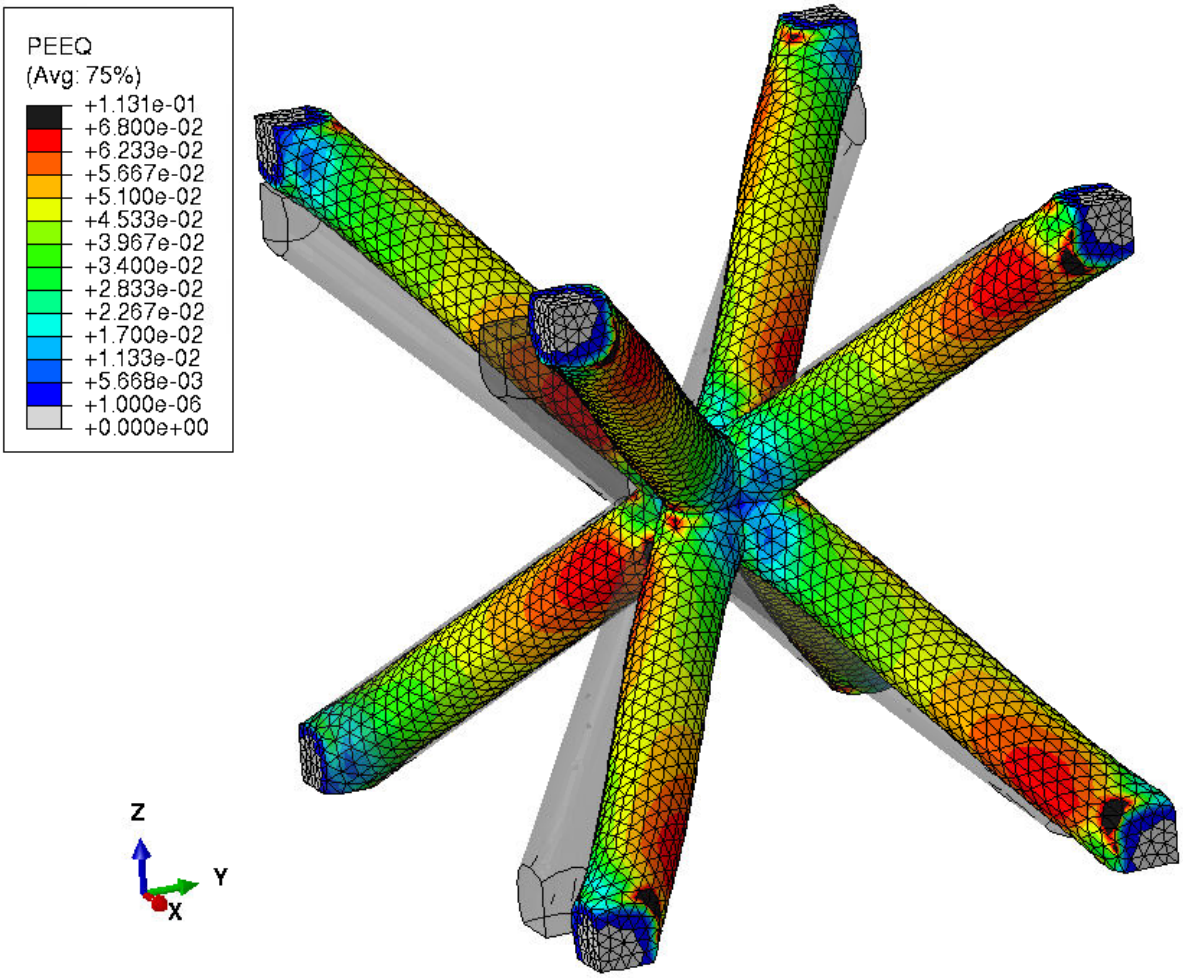

Fig. 6.30 The deformed and undeformed (shaded) shape of the solid element model, as well as the equivalent plastic strain (PEEQ) distribution at the endpoint (engineering strain of 3.75%) of the combined 45° shear XY and hydrostatic tension load cases in the single step.

At the engineering strain of 3.75%, the plasticity is present in almost all regions of the solid element UC, except on the tips of the struts (*Fig. 6.30*). The highest plasticity, excluding the local PEEQ concentrations at the vertices, is localized to the regions that experience the highest bending deformation (red colored in *Fig. 6.30*).

The obtained engineering strain-time and engineering stress-time curves from both modeling approaches are presented and compared in *Fig. 6.31*. The relevant effective normal stress and strain components are shown, the remaining ones are zero.

Due to the bending deformation, there is a small nonlinear transition in the elastoplastic region of the curve. The small differences in the engineering stress-time curves between the normal stress components are presumably caused by the modeling effects.

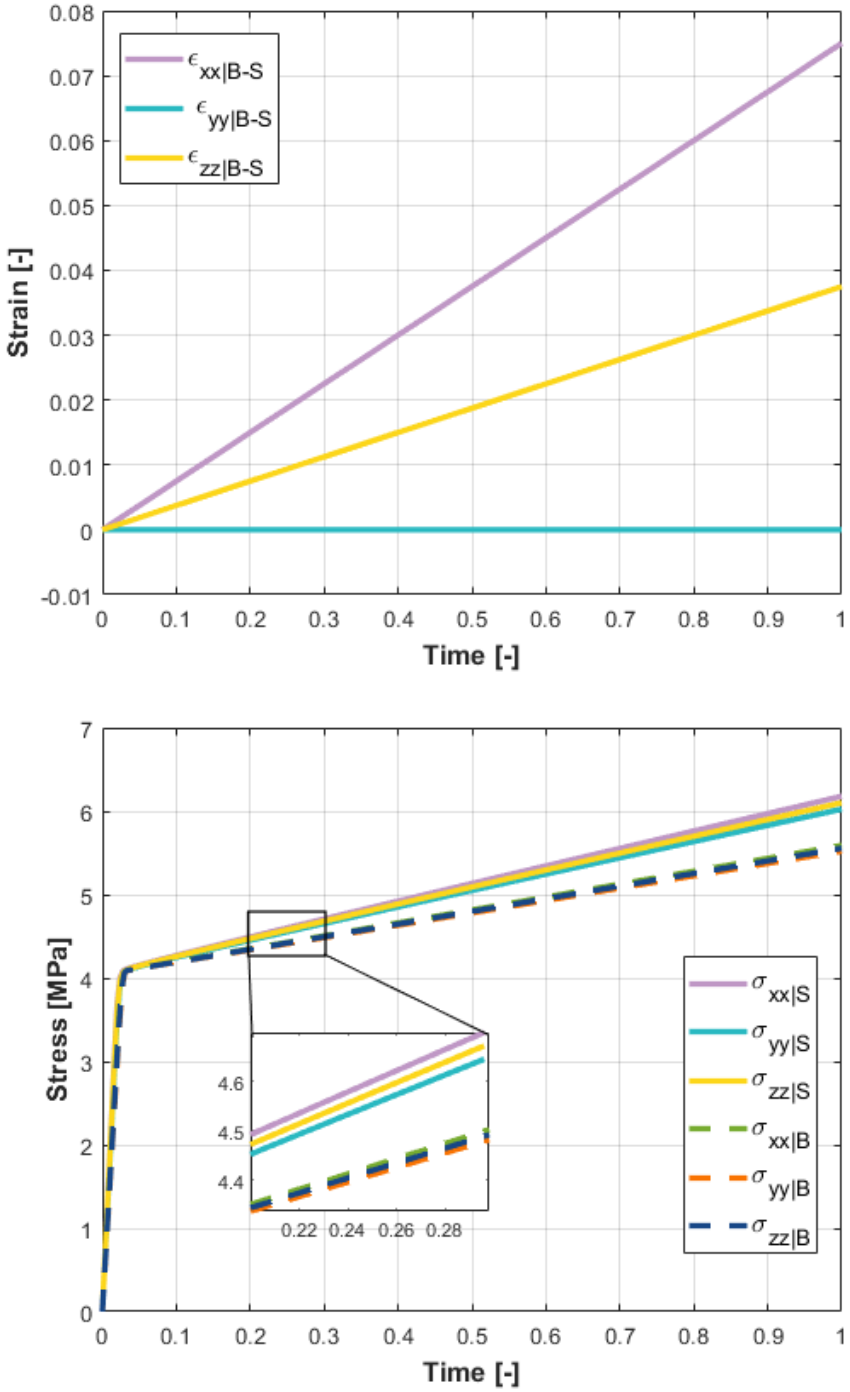

Fig. 6.31 The obtained engineering strain-time (top) and engineering stress-time (bottom) curves for the combined 45° shear and hydrostatic tension load cases in a single step for the beam model (index B) and solid element model (index S). The index $B-S$ in the engineering strain-time plot denotes that the applied strain components are equal for both solid and beam element models. For better clarity of the small differences in the slopes of the curves, a magnified view of the results for the time range between 0.2 and 0.3 is shown.

6.5 Two load cases applied in two steps

In this section, the results from the models where the two different load cases are applied in two different steps are discussed. This is achieved by applying displacements of the first load case in the first step, and then superimposing these with the displacements for the second load case in the second step. The combinations that are studied are combined simple shear XY and XZ, simple shear XY and hydrostatic tension, simple shear XY and 45° shear XY, as well as 45° shear XY and hydrostatic tension load cases. The BCs that are applied in the first step are the same ones used for the single load cases (*Tab. 4.1*), but the applied engineering strain is adjusted to 2% instead of 3.75%. For the second step, the BCs with superimposed displacements (*Tab. 6.5*) are implemented, but the applied strain is again adjusted to 2% instead of 3.75%.

The results are presented in the same way as in the previous sections. The comparison of the deformed and undeformed shapes for each of the modeling approaches under these load conditions is shown in the corresponding figures. For the beam models, the axial stress (S11) distribution at the outermost fiber (*Fig. 3.3*) displayed in the local orientation of beams is shown. For the solid element models, the accumulated equivalent plastic strain (PEEQ) distribution is shown, according to which the plastic deformation behavior can be evaluated. The results are shown for the endpoint of the second step of the load case since the endpoint of the first step corresponds to the results from the single load cases at the slightly lower applied engineering strains (i.e. 2% instead of 3.75%).

6.5.1 Simple shear XY and XZ load cases

The results that are obtained for the combined simple shear XY and XZ load cases in two different steps are discussed in this section. The deformed and undeformed shapes of the UC at the endpoint of the second step (engineering strain of 2%) for the beam model (*Fig. 6.32*) and solid element model (*Fig. 6.33*) are shown in corresponding figures.

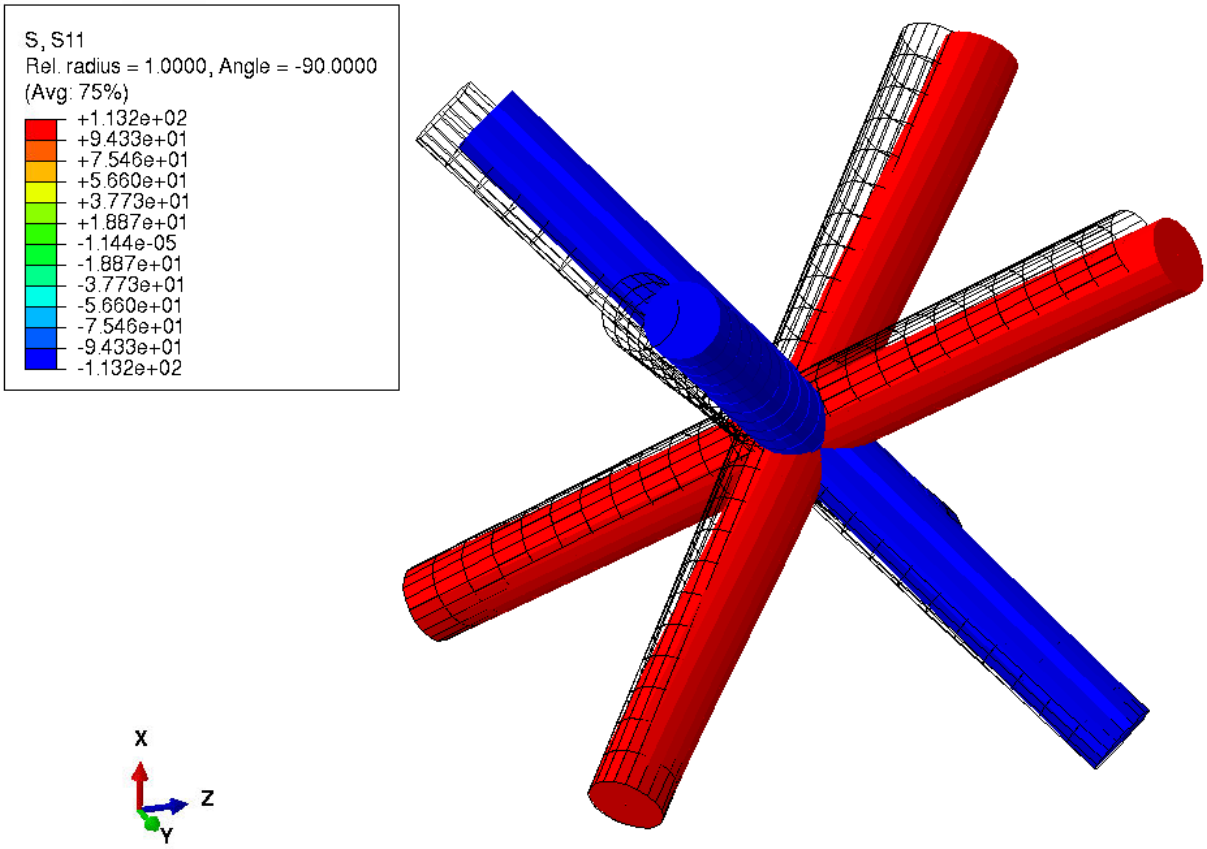

Fig. 6.32 The deformed and undeformed (wireframe) shape of the beam element model, as well as the axial stress (S11) distribution at the outermost fiber (*Fig. 3.3*) in the local orientation of beam elements at the endpoint of the second step (engineering strain of 2%) of the combined simple shear XY and XZ load cases in two different steps.

For the beam element model, the results at the end of the first step (engineering strain of 2%) are analogous to the results from the single simple shear XY load case (*Fig. 6.8*). From the deformed figure of the beam element UC, as well as the axial stress (S11) distribution at the outermost fiber (*Fig. 3.3*) in the local orientation of beam elements at the endpoint of the second step (*Fig. 6.32*), it is concluded that four of the struts are stretched and the remaining four are compressed. Additionally, there is some amount of bending deformation present as well.

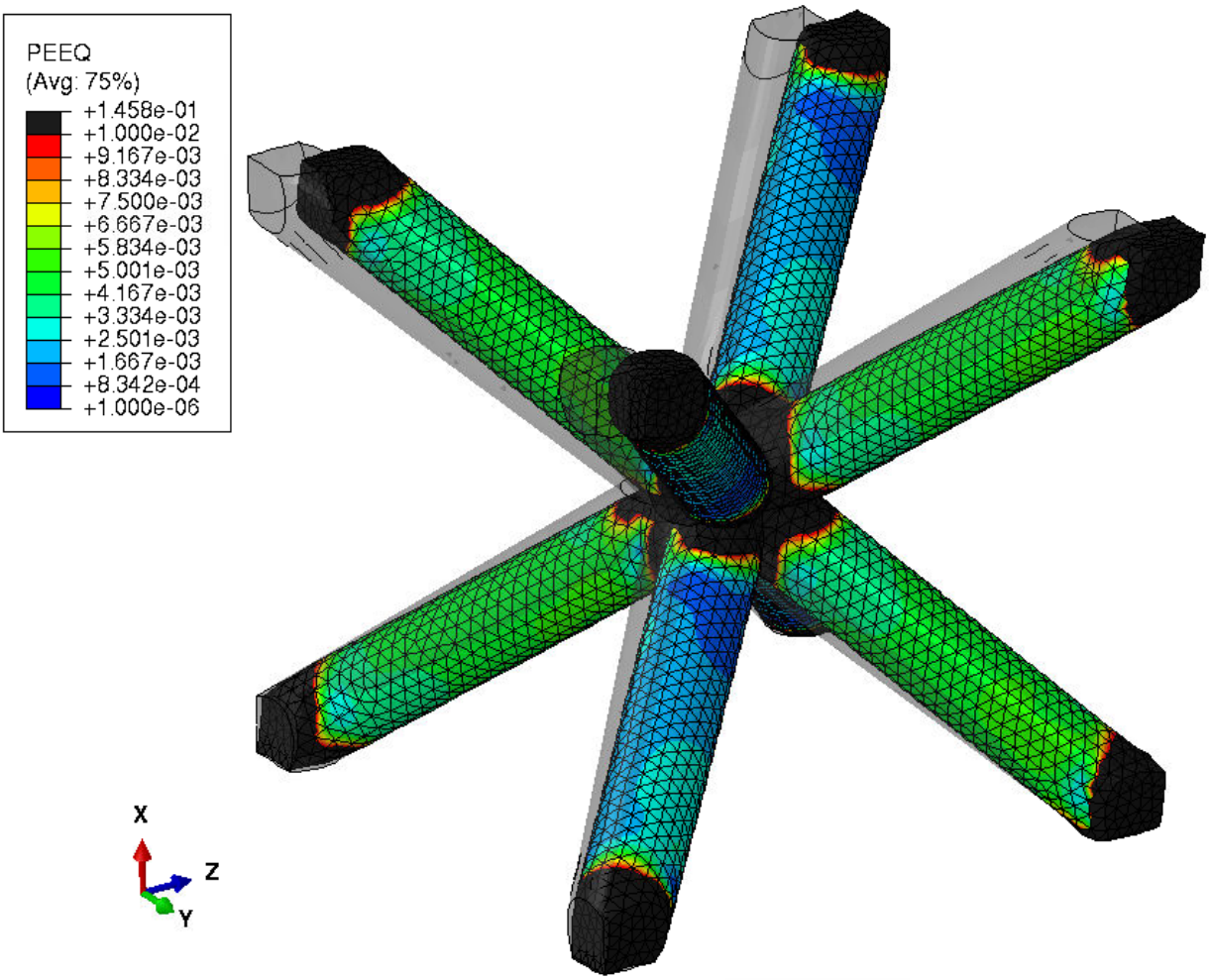

Fig. 6.33 The deformed and undeformed (shaded) shape of the solid element model, as well as the equivalent plastic strain (PEEQ) distribution at the endpoint of the second step (engineering strain of 2%) of the combined simple shear XY and XZ load cases in two different steps.

The explanation of the deformation behavior, as the transition between two simple shear loads occurs, is the same as for the combined single-step modeling variant. The main difference is that there are no relieved struts at the end of the second step, simply due to the global deformation behavior that occurs (i.e. the UC's face perpendicular to the x-axis does not directly move in the face diagonal direction as in the combined single-step case). For the two-step modeling variant, the struts that are supposed to be relieved, are deformed and experience some amount of isotropic hardening in both steps of the load case.

The results for the solid element UC model at the endpoint of the first step (engineering strain of 2%) are analogous to the single simple shear XY load case (*Fig. 6.10*). At the end of the second step (engineering strain of 2%), as shown in *Fig. 6.33*, plasticity is present in all regions of the UC, with the highest amount localized at the vertices (the same as with the single simple shear XY load case). Additionally, the struts that undergo unloading, have a lower plastic deformation compared to the remaining ones.

The obtained engineering strain-time and engineering stress-time curves from both modeling approaches are presented and compared in *Fig. 6.34*. The relevant effective shear stress and shear angle components are shown, the remaining ones are zero.

The first part of the engineering stress-time curve (time values between 0 and 1), corresponding to the first step, behaves in the same way as the single simple shear XY load case (*Fig. 6.11*). At the beginning of the second step, as the transition between the simple shear loads unfolds, there is the gradual relieving of the four struts, while the remaining four are additionally stretched or compressed. The deformation mechanisms of the latter struts remain the same up to the endpoint of the second step, only the amount of deformation increases with the load. The former struts are fully relieved at around $t = 1.15$, where the corresponding effective shear stress curves cross each other. From this point, the same mechanism that led to the unloading of these struts continues and now leads to their further deformation. The "relieved" struts that were initially stretched, now undergo compression, and vice versa. As this process continues, the effective shear stress component from the first load case slowly drops to zero. When looking at the second step, the effect of the isotropic hardening can be seen, since the nonlinear elastoplastic regions start at higher points compared to the first load case.

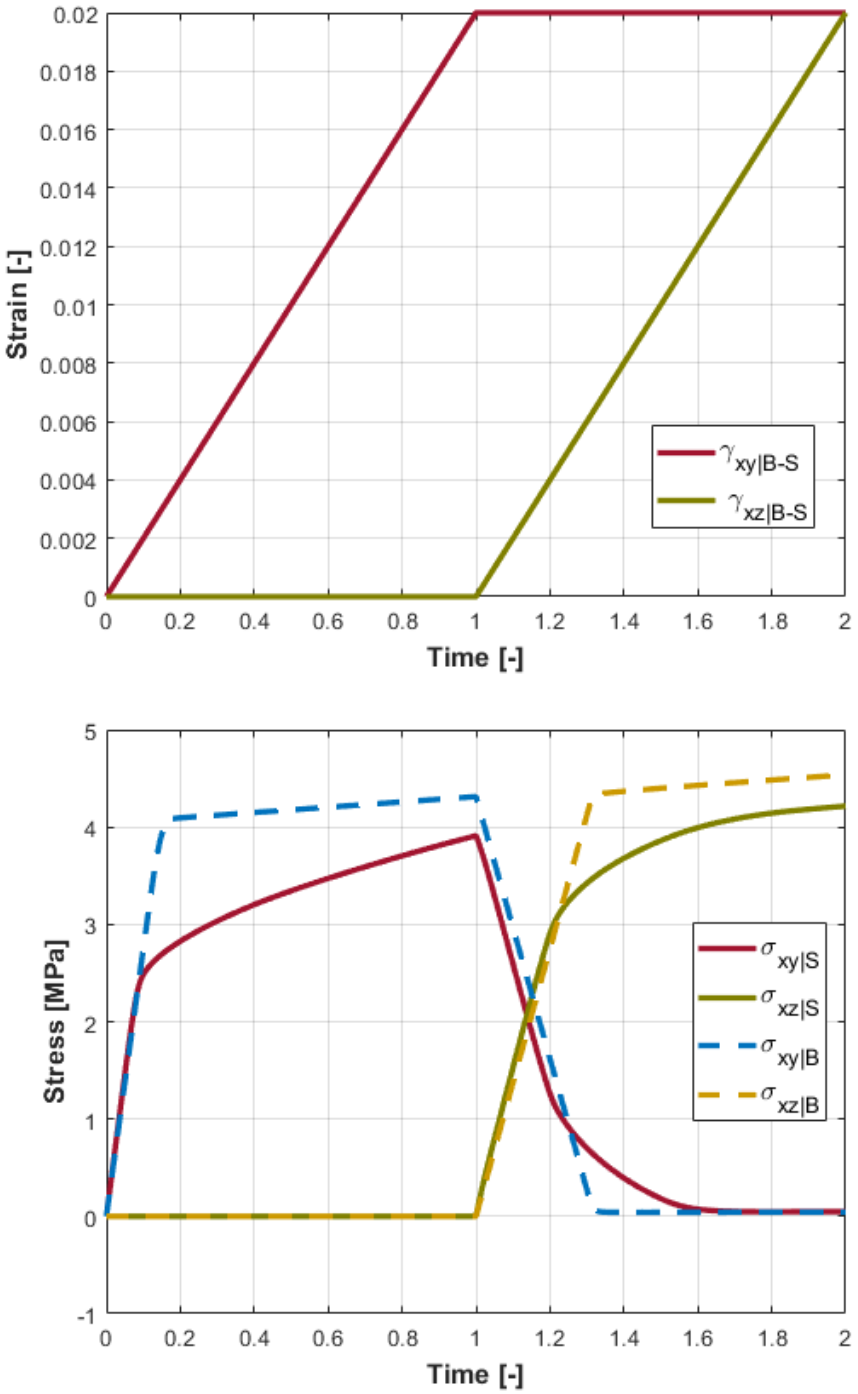

Fig. 6.34 The obtained engineering strain-time (top) and engineering stress-time (bottom) curves for the combined simple shear XY and XZ shear load cases in two different steps for the beam model (index B) and solid element model (index S). The index $B-S$ in the engineering strain-time plot denotes that the applied strain components are equal for both solid and beam element models.

6.5.2 Simple shear XY and hydrostatic load cases

The results that are obtained for the combined simple shear XY and hydrostatic tension load cases in two different steps are discussed in this section. The deformed and undeformed shapes of the UC at the endpoint of the second step (engineering strain of 2%) for the beam model (*Fig. 6.35*) and solid element model (*Fig. 6.36*) are shown in corresponding figures.

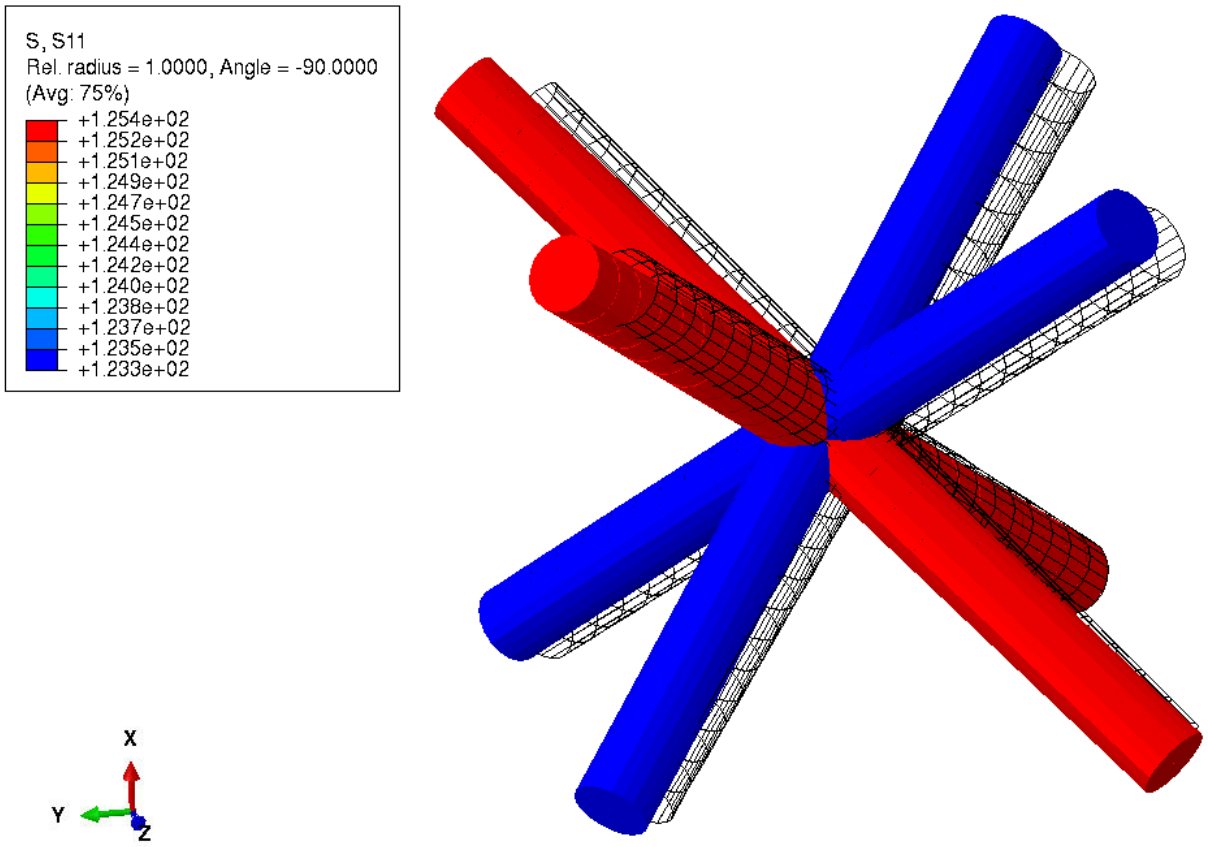

Fig. 6.35 The deformed and undeformed (wireframe) shape of the beam element model, as well as the axial stress (S11) distribution at the outermost fiber (*Fig. 3.3*) in the local orientation of beam elements at the endpoint of the second step (engineering strain of 2%) of the combined simple shear XY and hydrostatic tension load cases in two different steps.

For the beam element model, the behavior and results at the end of the first step (engineering strain of 2%) are analogous to the results from the single simple shear XY load case (*Fig. 6.8*). From the deformed figure of the beam element UC, as well as the axial stress (S11) distribution at the outermost fiber (*Fig. 3.3*) in the local orientation of beam elements at the endpoint of the second step (engineering strain of 2%), shown in *Fig. 6.35*, it is concluded that all of the struts are under pure tension.

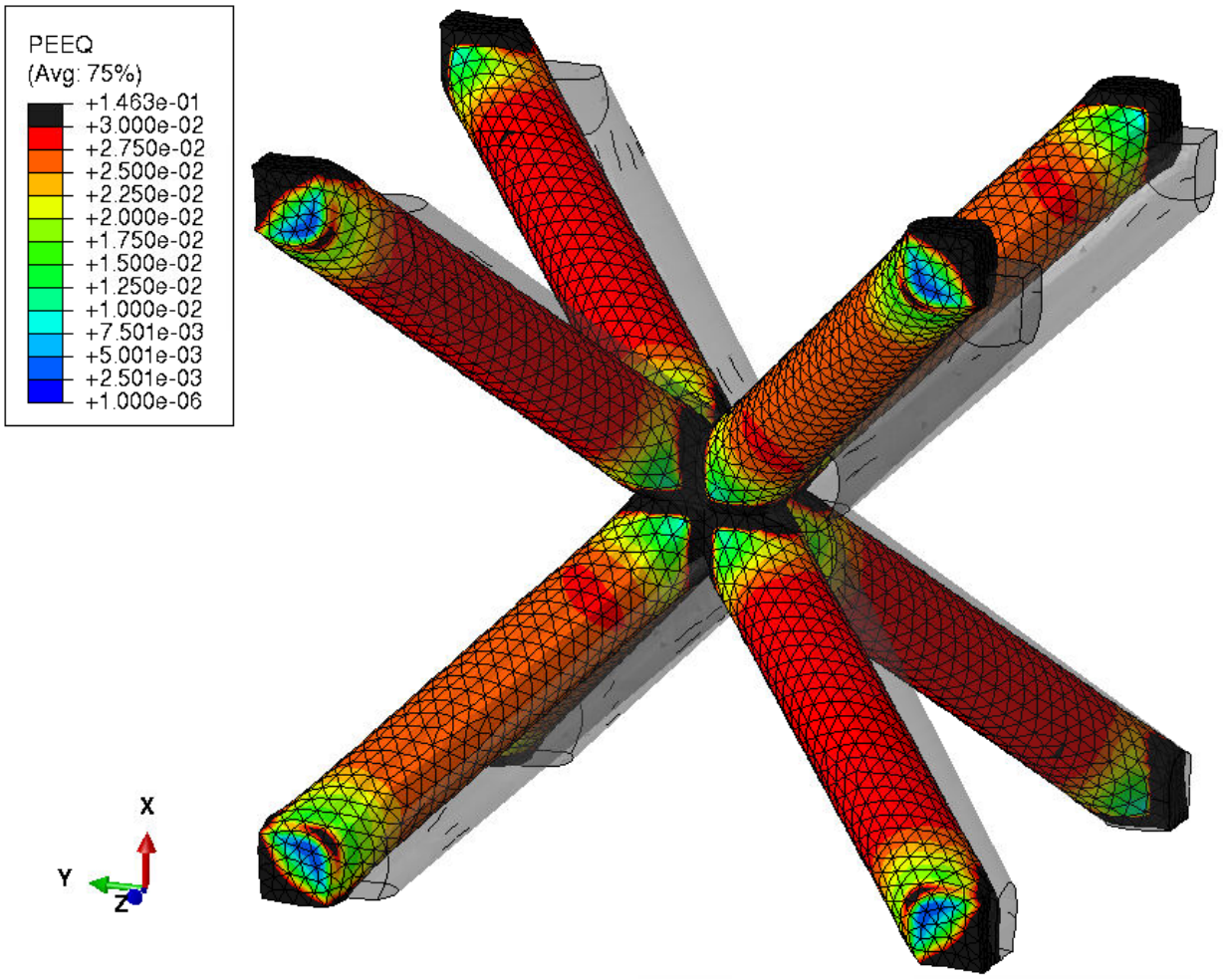

Fig. 6.36 The deformed and undeformed (shaded) shape of the solid element model, as well as the equivalent plastic strain (PEEQ) distribution at the endpoint of the second step (engineering strain of 2%) of the combined simple shear XY and hydrostatic tension load cases in two different steps.

The explanation of the deformation behavior, as the transition between two load cases occurs, is the same as for the combined single-step modeling variant. The main difference between the single-step and two-step approach lies in the tensile stresses and the amount of plasticity that initially stretched and compressed struts experience at the endpoint of the load case. In the two-step model, all struts undergo roughly the same amount of stress and plastic deformation, whereas the differences in these aspects between the initially stretched and compressed struts are more pronounced in the single-step approach. This behavior in the former approach occurs because hydrostatic tension predominantly influences the deformation in the second step. This allows the initially compressed struts to closely match the remaining (initially stretched) ones.

The results for the solid element UC model at the endpoint of the first step (engineering strain of 2%) are analogous to the single simple shear XY load case (*Fig. 6.10*). At the end of the second step (engineering strain of 2%), shown in *Fig. 6.36*, plasticity is present in all regions of the UC, with higher amounts of it concentrated in the central regions of the struts. Additionally, the initially compressed struts experience slightly lower plastic deformation compared to the rest.

The obtained engineering strain-time and engineering stress-time curves from both modeling approaches are presented and compared in *Fig. 6.37*. The relevant effective normal and shear stress, shear angle, and normal strain components are shown. The effective normal stresses in the x, y, and z-directions are equal, and the same is true for the effective normal strains. The remaining stress and strain components, that are not shown, are zero.

The first part of the engineering stress-time curve (time values between 0 and 1), corresponding to the first step, behaves in the same way as the single simple shear XY load case (*Fig. 6.11*). At the beginning of the second step, as the transition between the load cases unfolds, there is a gradual stretching of all struts. The initially compressed struts from the simple shear XY load case are relieved at the point where the corresponding effective normal and shear stress curves cross each other (at around $t = 1.05$). From this point, the same deformation mechanism continues, and these struts are further stretched, but never completely "catch up" to the remaining ones, that were under tension from the beginning. As this process continues, the effective shear stress component from the first load case slowly drops to zero. Additionally, it can be seen that the bending of the struts from the simple shear XY load case is completely minimized, since there is only a sharp transition to the elastoplastic region in the second step. The effect of the isotropic hardening can also be seen from the curves in this step since the elastoplastic regions start at higher points compared to the first load case.

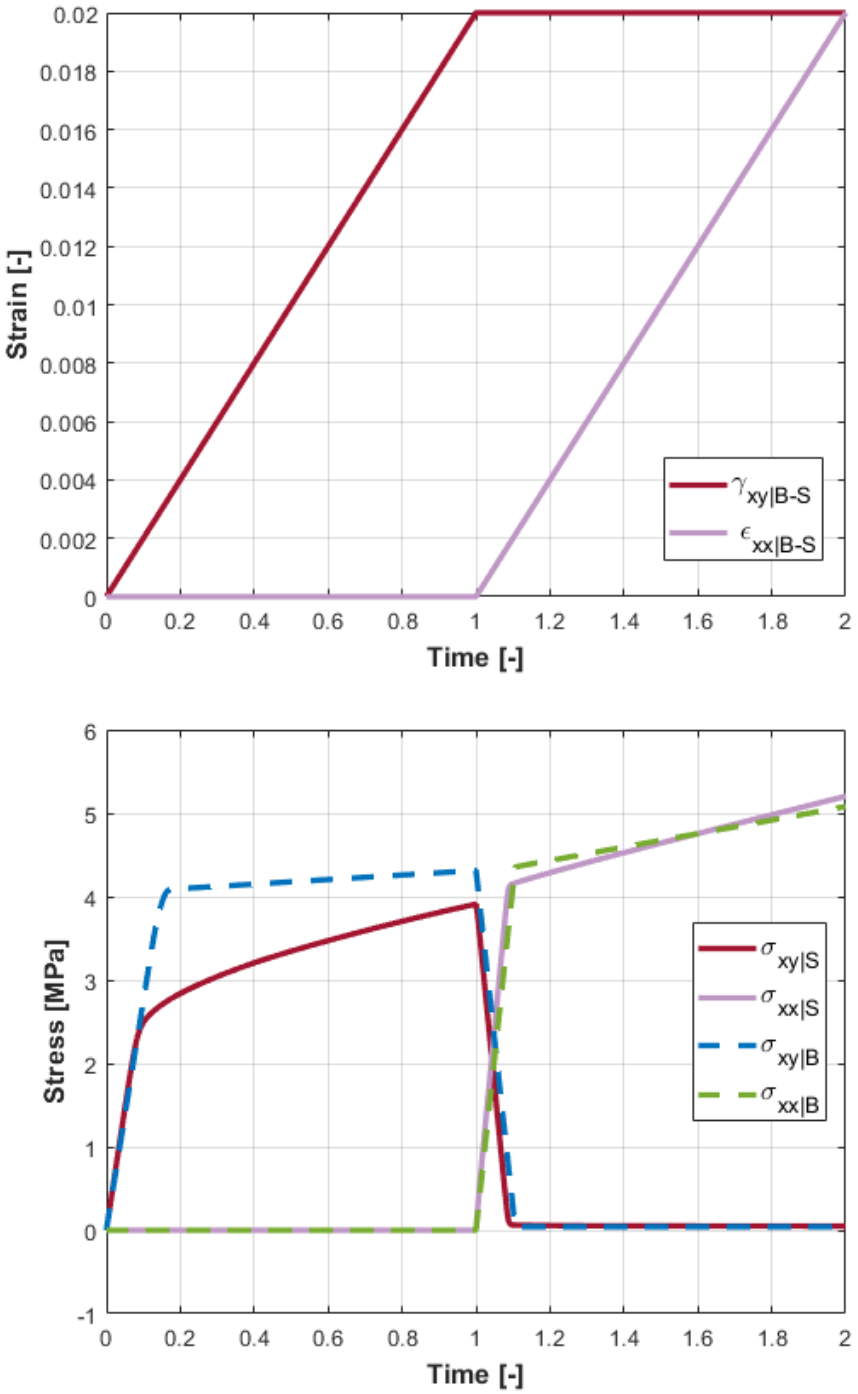

Fig. 6.37 The obtained engineering strain-time (top) and engineering stress-time (bottom) curves for the combined simple shear XY and hydrostatic tension load cases in two different steps for the beam model (index B) and solid element model (index S). The index $B-S$ in the engineering strain-time plot denotes that the applied strain components are equal for both solid and beam element models. The effective normal stresses in the x, y, and z-directions are equal, and the same is true for the effective normal strains.

6.5.3 Simple shear XY and 45° shear XY load cases

The results that are obtained for the combined simple shear XY and 45° shear XY load cases in two different steps are discussed in this section. The deformed and undeformed shapes of the UC at the endpoint of the second step (engineering strain of 2%) for the beam model (*Fig. 6.38*) and solid element model (*Fig. 6.39*) are shown in corresponding figures.

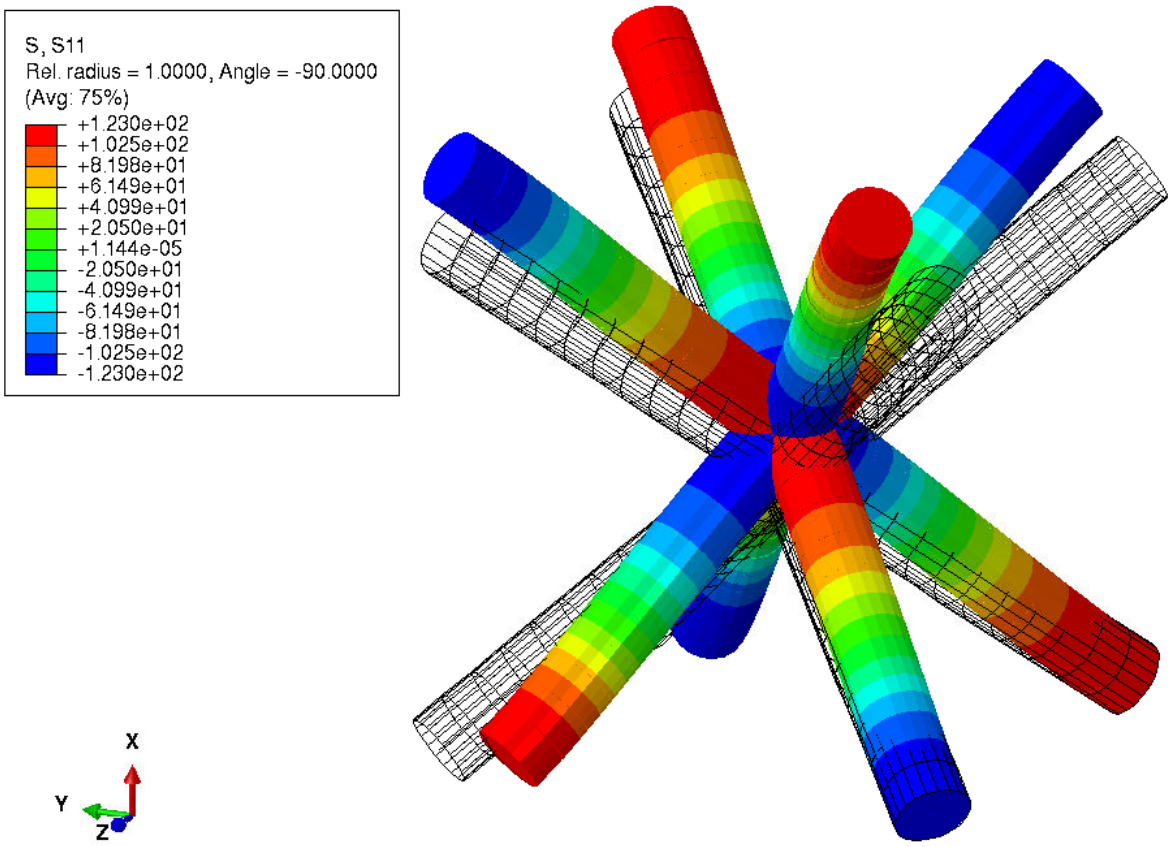

Fig. 6.38 The deformed and undeformed (wireframe) shape of the beam element model, as well as the axial stress (S11) distribution at the outermost fiber (*Fig. 3.3*) in the local orientation of beam elements at the endpoint of the second step (engineering strain of 2%) of the combined simple shear XY and 45° shear XY load cases in two different steps.

For the beam element mode, the results at the end of the first step (engineering strain of 2%) are analogous to the ones from the single simple shear XY load case (*Fig. 6.8*). From the deformed figure of the beam element UC, as well as the axial stress (S11) distribution at the outermost fiber (*Fig. 3.3*) in the local orientation of beam elements at the endpoint of the second step (engineering strain of 2%), shown in *Fig. 6.38*, it is concluded that all of the struts experience significant bending deformation.

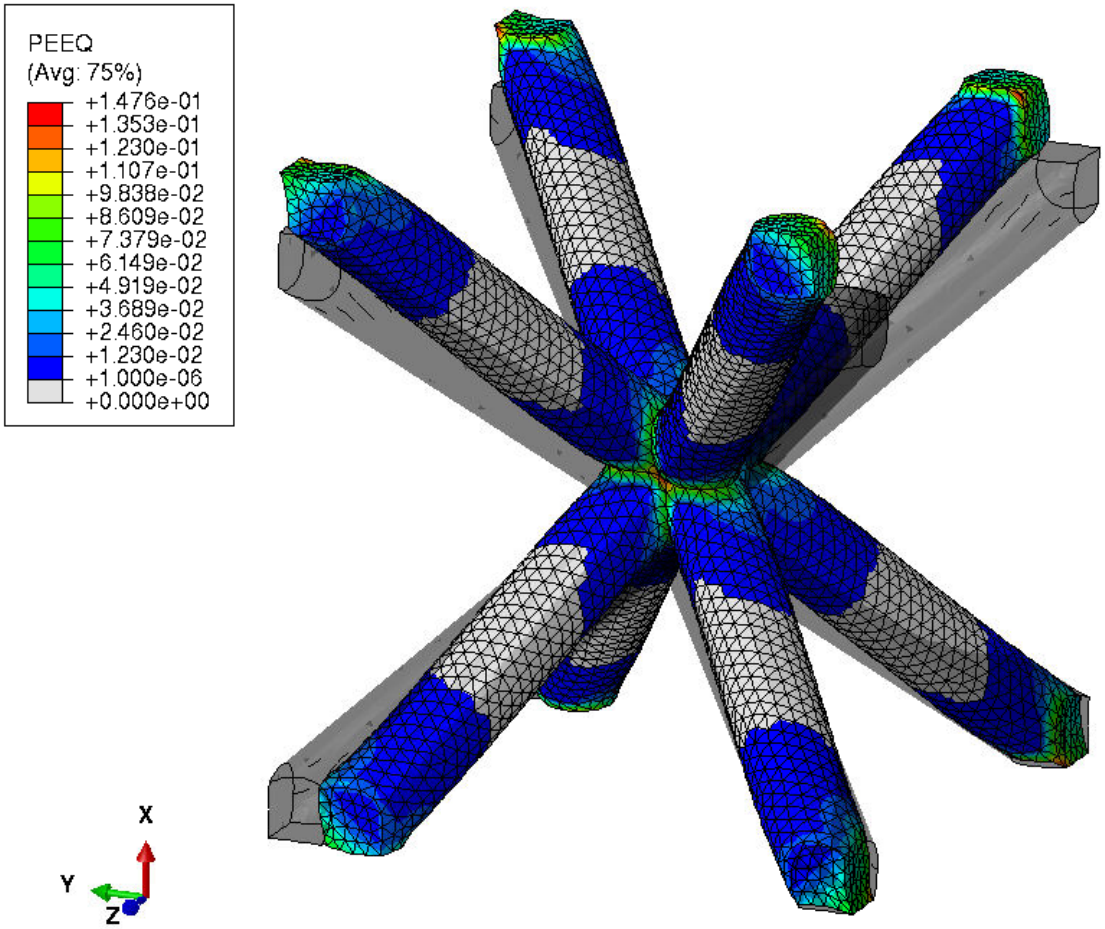

Fig. 6.39 The deformed and undeformed (shaded) shape of the solid element model, as well as the equivalent plastic strain (PEEQ) distribution at the endpoint of the second step (engineering strain of 2%) of the combined simple shear XY and 45° shear XY load cases in two different steps.

The explanation of the deformation behavior, as the transition between two loads occurs, is the same as for the combined single-step load case. Compared to this modeling variant, the results at the endpoint of the second step from the combined two-step approach show that overall bending deformation is higher and that the plasticity expands more uniformly from the vertices towards the central regions of the struts. As the influence of the 45° shear XY load case on the overall deformation behavior increases in the second step, so is this behavior more pronounced.

The results for the solid element UC model at the endpoint of the first step (engineering strain of 2%) are analogous to the single simple shear XY load case (*Fig. 6.9*). At the end of the second step (engineering strain of 2%), shown in *Fig. 6.39*, plasticity is present in the vicinity of the vertices and has evolved further towards the central regions of the struts in a more uniform manner.

The obtained engineering strain-time and engineering stress-time curves from both modeling approaches are presented and compared in *Fig. 6.40*. The relevant effective normal and shear stress, shear angle, and normal strain components are shown. The remaining stress and strain components, that are not shown, are zero. The effective stress and strain components from the 45° shear XY load case are shown in their form before transformation, i.e. as normal stresses and strains.

The first part of the engineering stress-time curve (time values between 0 and 1), corresponding to the first step, behaves in the same way as the single simple shear XY load case (*Fig. 6.11*). At the beginning of the second step, as the transition between the load cases unfolds, there is a gradual increase in the bending deformation of the struts, which leads to a decrease in the value of the corresponding effective shear stress component.

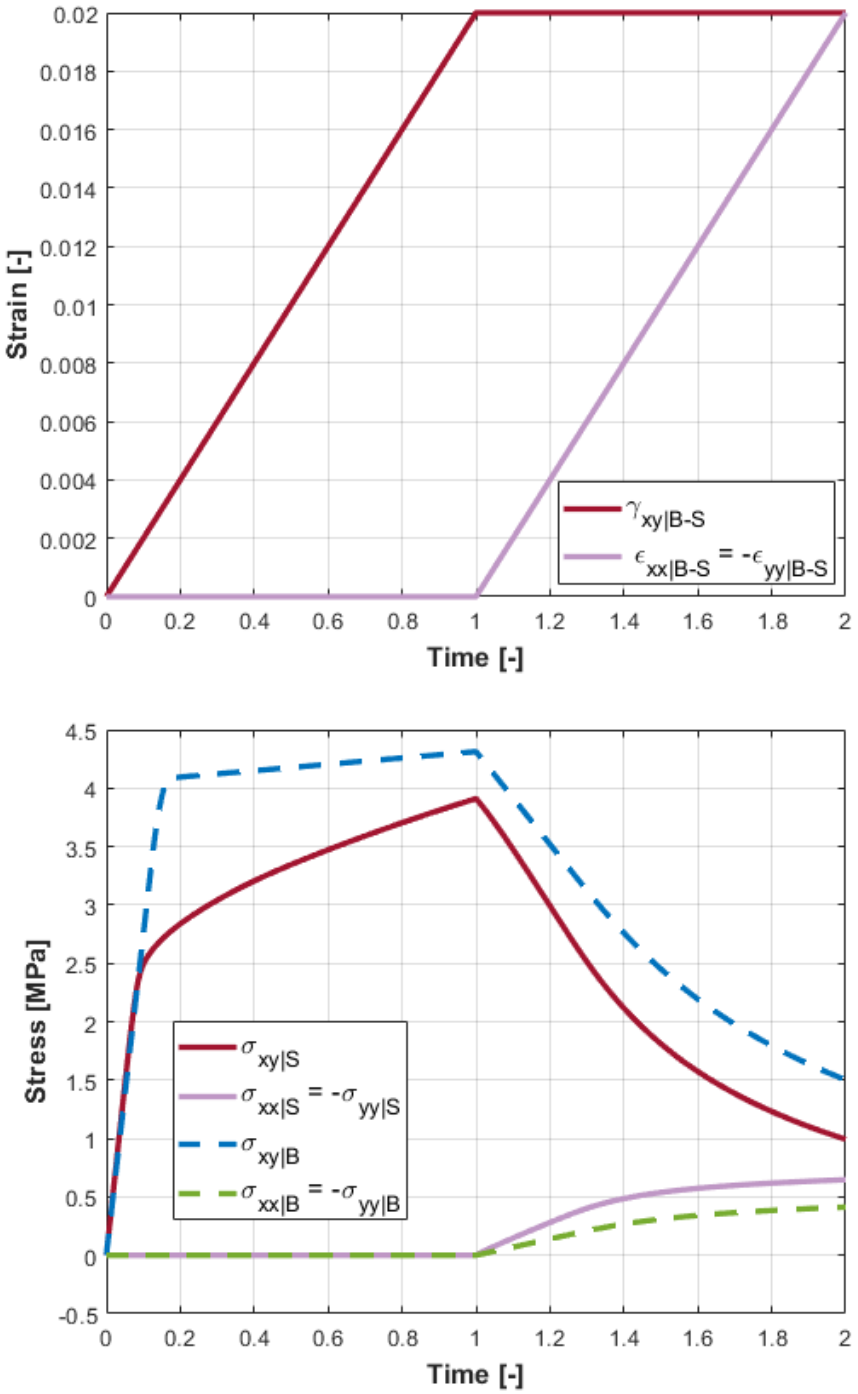

Fig. 6.40 The obtained engineering strain-time (top) and engineering stress-time (bottom) curves for the combined simple shear XY and 45° shear XY load cases in two different steps for the beam model (index B) and solid element model (index S). The index $B-S$ in the engineering strain-time plot denotes that the applied strain components are equal for both solid and beam element models.

6.5.4 45° shear XY and hydrostatic load cases

The results that are obtained for the combined 45° shear XY and hydrostatic tension load cases in two different steps are discussed in this section. The deformed and undeformed shapes of the UC at the endpoint of the second step (engineering strain of 2%) for the beam model (*Fig. 6.41*) and solid element model (*Fig. 6.42*) are shown in corresponding figures.

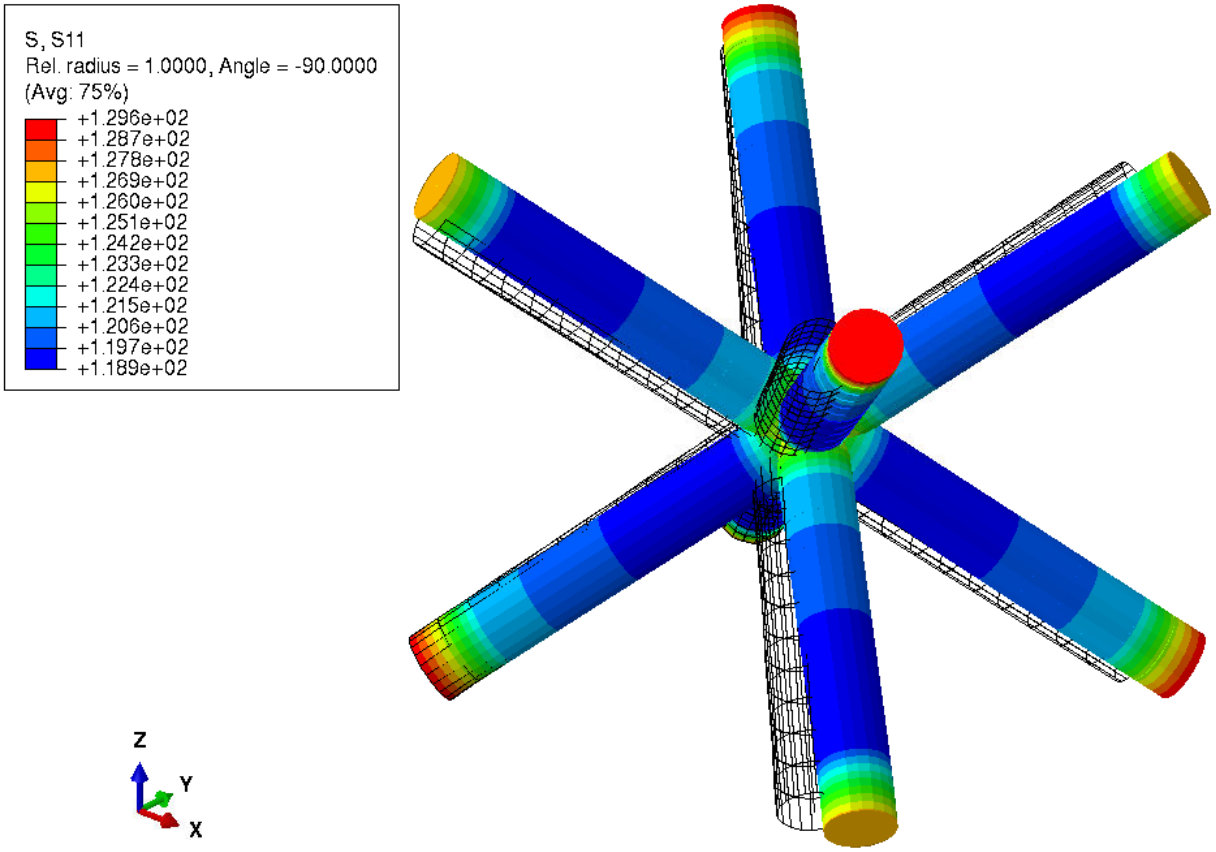

Fig. 6.41 The deformed and undeformed (wireframe) shape of the beam element model, as well as the axial stress (S11) distribution at the outermost fiber (*Fig. 3.3*) in the local orientation of beam elements at the endpoint of the second step (engineering strain of 2%) of the combined 45° shear XY and hydrostatic tension load cases in two different steps.

For the beam element mode, the behavior and results at the end of the first step are analogous to the results from the single 45° shear XY load case (*Fig. 6.12*). From the deformed figure of the beam element UC, as well as the axial stress (S11) distribution at the outermost fiber (*Fig. 3.3*) in the local orientation of beam elements at the endpoint of the second step, shown in *Fig. 6.41*, it is concluded that the struts are predominantly stretched with some amount of bending deformation being present.

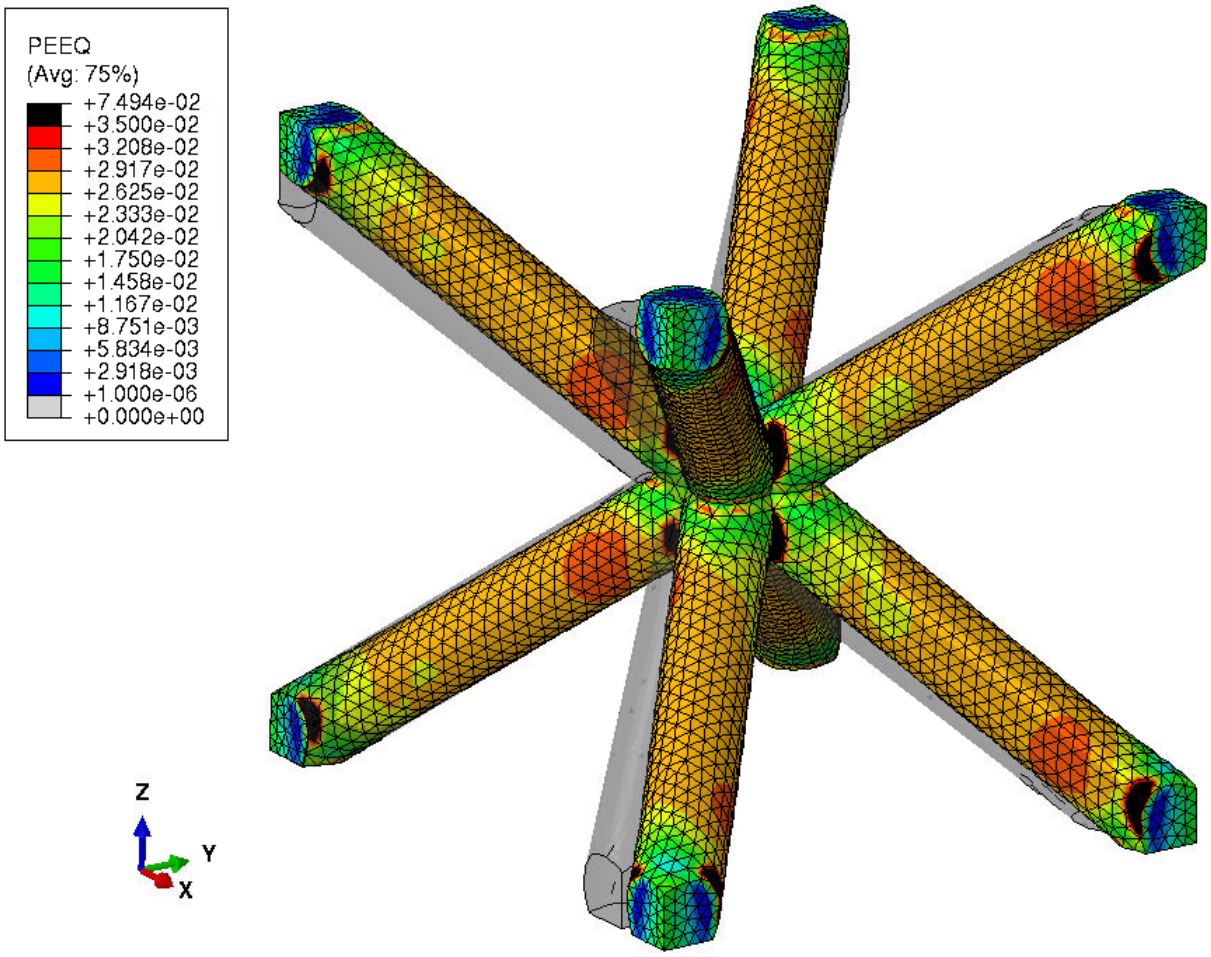

Fig. 6.42 The deformed and undeformed (shaded) shape of the solid element model, as well as the equivalent plastic strain (PEEQ) distribution at the endpoint of the second step (engineering strain of 2%) of the combined 45° shear XY and hydrostatic tension load cases in two different steps.

The explanation of the deformation behavior, as the transition between two loads occurs, is the same as for the combined single-step load case. The difference is, that the second step is dominated by the tension from the hydrostatic load case, which minimizes the bending deformation. This results in lower plasticity peaks in the regions that experience the highest bending, and overall more uniform plasticity distribution on the struts.

The results for the solid element UC model at the endpoint of the first step (engineering strain of 2%) are analogous to the single 45° shear XY load case (*Fig. 6.13*). At the end of the second step (engineering strain of 2%), plasticity is present in all regions of the UC. The highest plasticity, excluding the local PEEQ concentrations at the vertices, is localized to the regions that experience the highest bending (dark orange color in *Fig. 6.42*).

The obtained engineering strain-time and engineering stress-time curves from both modeling approaches are presented and compared in *Fig. 6.43*. The relevant effective normal stress and strain components are shown, the remaining ones are zero. The effective stress and strain components from the 45° shear XY load case are shown in their form before the transformation, i.e. as normal stresses and strains.

The first part of the engineering stress-time curve (time value between 0 and 1), corresponding to the first step, behaves in the same way as the single 45° shear XY load case (*Fig. 6.14*). At the beginning of the second step, as the transition between the load cases unfolds, there is a gradual decrease in the bending deformation of the struts. Because of this bending deformation, there is a small nonlinear transition in the elastoplastic region of the curve. The small differences in the engineering stress-time curves between the normal stress components are presumably caused by the modeling effects.

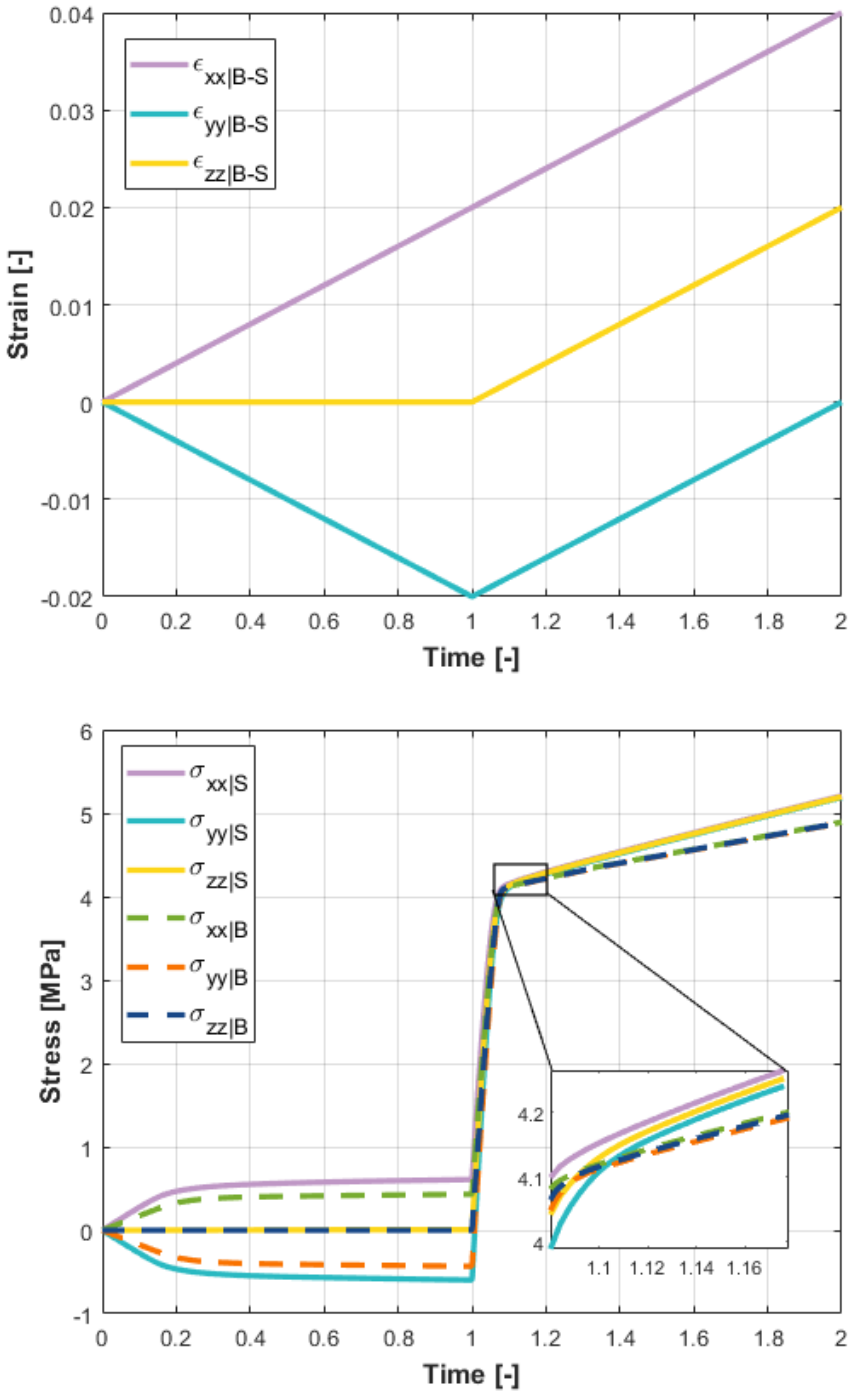

Fig. 6.43 The obtained engineering strain-time (top) and engineering stress-time (bottom) curves for the combined 45° shear XY and hydrostatic tension load cases in two different steps for the beam model (index B) and solid element model (index S). The index $B-S$ in the engineering strain-time plot denotes that the applied strain components are equal for both solid and beam element models. For better clarity of the small differences in the slopes of the curves, a magnified view of the results for the time range 1.06 - 1.2 is shown.

7. Conclusion

The elastic and elastoplastic behavior of the solid and beam element BCC lattice UC is determined. From the literature and definition of the elements, it is known that the approach with continuum elements is more accurate, but also computationally more expensive. The beam models neglect the material aggregation and overlapping volumes at the junctions of multiple struts in the model, which leads to lower stiffness, and thus is the main reason for inaccuracies. Although the approach with beam elements is coupled with some inaccuracies, it is computationally much more efficient and still provides satisfactory results, which is confirmed by the results. An increased number of beam section points is required to correctly capture nonlinear stress distribution for the load cases involving elastoplastic bending deformation of the struts. For the cases, where the bending deformation is small (simple shear) or non-existent (hydrostatic tension), the default number of section points can deliver correct results as well.

The effective bulk modulus $\tilde{K}$, shear modulus $\tilde{M}$, shear modulus $\tilde{G}$, and Young's modulus $\tilde{E}$ in the principal material direction [100] are computed for both modeling approaches. Due to the inaccuracies of the beam modeling approach, the obtained values for these moduli from the beam UC are slightly lower, i.e. the solid element UC is stiffer than the beam element one. Depending on the load case, in addition to compression and tension, the struts can experience bending as well. The highest bending deformation is present for the 45° shear load case, followed by the uniaxial tension in the [100] direction. The higher the bending of the struts, the lower the stiffness of the UC. This is reflected in the values of the corresponding effective moduli. Under the simple shear load case, two pairs of the struts are stretched while the other two are compressed. Additionally, some amount of bending deformation is present. Under the hydrostatic tension, the struts experience only pure tension, and the UC has a high stiffness. Due to the cubic material symmetry of the UC, the effective elasticity tensor for both modeling approaches is computed from $\tilde{K}$, $\tilde{M}$, and $\tilde{G}$. Lastly, the effective Young's moduli in the face diagonal direction [110], and space diagonal direction [111] are determined for the solid element model, due to the higher accuracy. According to the property of the cubic material symmetry, the modulus values obtained in the [100] and [111] directions represent extremes. In this case, the effective Young's moduli in these directions are minimum and maximum respectively, whereas the one from the [110] direction lies between them.

The initial yield stress values for the six load cases implemented for the elastic behavior of the UC are obtained for the solid element model. The values are in agreement with the overall conclusions regarding the predominant deformation mechanisms of the struts and the stiffness of the UC. All of the initial yield surface representations are oval-shaped. Model I (plane stress state without any shear stress component), as well as models IV and V (plane stress state with a constant shear stress component), are similar in shape. The surface representations of models II and III (in-plane principal stresses are varied, while the positive out-of-plane principal stress is constant) are more asymmetrical and shifted in the direction of the first quadrant, due to the presence of the positive out-of-plane principal stress. This also leads to the overall lower yield stress values in the regions where the compressive stresses begin to dominate the load cases, in comparison to the remaining representations. Due to the presence of the constant in-plane shear stress component for models IV and V, the overall yield stress values are reduced, "pulling" the surface inward, in comparison to the results from model I. These results only show a glimpse into the initial yield surface of the BCC lattice UC, and many more different stress states and surface representations are required to obtain the whole picture.

The elastoplastic behavior is assessed for various load cases, applied either individually or as a combination (single-step or two-step). The main results for the elastoplastic material behavior are shown in the form of engineering stress-strain curves and corresponding deformation behaviors, as well as the distribution of the accumulated equivalent plastic strain (PEEQ) for the solid element model. The effective bulk modulus $\tilde{K}$, Young's modulus $\tilde{E}$, and shear moduli $\tilde{G}$ and $\tilde{M}$ are obtained from the linear regions of corresponding engineering stress-strain curves and compared to the values obtained from the linear elastic UC models. The effective tangent moduli are also determined from the slopes of the engineering stress-strain curves in the linear elastoplastic regions, from which the corresponding effective hardening moduli are computed. The deformation behavior of the UC under all studied load cases is discussed in detail.

List of Figures

List of Tables

Bibliography

[1] *ABAQUS Version 6.6 Documentation*. Accessed on 2023-10-19. 2021. URL: https://classes.engineering.wustl.edu/2009/spring/mase5513/abaqus/docs/v6.6/index.html.

[2] M.F. Ashby. "The properties of foams and lattices". *Philosophical Transactions of the Royal Society A* 364 (2006), pp. 15–30.

[3] Helmut J. Böhm. *Continuum Micromechanics of Materials, lecture notes*. Vienna, Austria: ILSB, TU Wien, 1993, 2017.

[4] Ondrej Cervinek et al. "Computational Approaches of Quasi-Static Compression Loading of SS316L Lattice Structures Made by Selective Laser Melting". *Materials* 14 (2021), p. 2462.

[5] Ondrej Cervinek et al. "Non-linear dynamic finite element analysis of micro-strut lattice structures made by laser powder bed fusion". *Journal of Materials Research and Technology* 18 (2022), pp. 3684–3699.

[6] Rammerstorfer F.G. *Einführung in die Finite Elemente Methoden, lecture notes*. Vienna, Austria: ILSB, TU Wien, 2017.

[7] Rammerstorfer F.G. *Repetitorium Leichtbau*. Vienna, Austria: ILSB, TU Wien, 2017.

[8] ASTM F2792-12. *Standard Terminology for Additive Manufacturing Technologies*. West Conshohocken, PA, USA: ASTM International, 2012.

[9] Lorna J. Gibson and Michael F. Ashby. *Cellular Solids - Structure and Properties*. Cambridge, UK: Cambridge University Press, 1997.

[10] Mathias Luxner, Juergen Stampfl, and Heinz E. Pettermann. "Numerical simulations of 3D open cell structures - influence of structural irregularities on elasto-plasticity and deformation localization". *International Journal of Solids and Structures* 44 (2007), pp. 2990–3003.

[11] Mathias H. Luxner, Juergen Stampfl, and Heinz E. Pettermann. "Finite element modeling concepts and linear analyses of 3D regular open cell structures". *Journal of Materials Science* 40 (2005), pp. 5859–5866.

[12] J.F. Nye. *Physical Properties of Crystals*. Oxford, UK: Oxford University Press, 1985.

[13] Kwang-Min Park, Kyung-Sung Min, and Young-Sook Roh. “Design Optimization of Lattice Structures under Compression: Study of Unit Cell Types and Cell Arrangements”. *Materials* 15 (2021), p. 97.

[14] H.E. Pettermann and J. Hüsing. “Modeling and simulation of relaxation in viscoelastic open cell materials and structures”. *International Journal of Solids and Structures* 49 (2012), pp. 2848–2853.

[15] Heinz E. Pettermann. *Advanced Maetrial Models for Structural Analysis, lecture notes*. Vienna, Austria: ILSB, TU Wien, 2022.

[16] Heinz E. Pettermann and Subra Suresh. “A comprehensive unit cell model: a study of coupled effects in piezoelectric 1–3 composites”. *International Journal of Solids and Structures* 37 (2000), pp. 5447–5464.

[17] Leonardo Riva, Paola Serena Ginestra, and Elisabeta Ceretti. “Mechanical characterization and properties of laser-based powder bed fused lattice structures: a review”. *The International Journal of Advanced Manufacturing Technology* 113 (2021), pp. 649–671.

[18] Ali A. Roostaei and Hamid Jahed. *Cyclic Plasticity of Metals*. Elsevier Ltd., 2022.

[19] I.C. Skrna-Jakl. *Leichtbau mit faserverstärkten Werkstoffen, lecture notes*. Vienna, Austria: ILSB, TU Wien, 2011.

[20] J. Stampfl et al. “Regular, low density cellular structures - rapid prototyping, numerical simulation, mechanical testing”. *Biological and Bioinspired Materials and Devices (Mater. Res. Soc. Symp. Proc.), eds. J. Aizenberg, W.J. Landis, C. Orme, R. Wang (Hrg.)* 823 (2004).

[21] Erik Tempelman, Hugh Shercliff, and Bruno Ninaber van Eyben. *Manufacturing and Design*. Elsevier Ltd., 2014.

[22] Melanie Todt and Marius Schasching. *Festkörperkontinuumsmechanik, lecture notes*. Vienna, Austria: ILSB, TU Wien, 2021.